



Title	A Study on Precoating-induced Protective -Al ₂ O ₃ Scale Formation on Ni-Al Alloy in the High Temperature Oxidation
Author(s)	Shaaban Mostafa, Mohammed Ali
Citation	北海道大学. 博士(総合化学) 甲第11947号
Issue Date	2015-06-30
DOI	10.14943/doctoral.k11947
Doc URL	http://hdl.handle.net/2115/59698
Type	theses (doctoral)
File Information	Ali_Mohammed_Shaaban_Mostafa.pdf



[Instructions for use](#)

**A Study on Precoating-induced Protective α -Al₂O₃ Scale
Formation on Ni-Al Alloy in the High Temperature Oxidation**

Ali Shaaban

Graduate School of Chemical Sciences and Engineering
Hokkaido University

2015

PREFACE

Acknowledgements

Thanks, *God*...

Thank you, everyone who helped, guided, and supported me during these almost four years! I know I am very lucky to have had all of you around me. First of all, I would like to thank my boss, *Prof. Azumi* who accepted me in ‘**Electronic Materials Chemistry Laboratory**’. I am very much grateful for his understanding and support with enlightening words, which guided me to do things to the best of my abilities. I have learned a lot under your supervision! Deepest thanks to my advisor during the course of this work (*Prof. Hayashi*). Thanks for your interest and for many very good discussions on **Materials Oxidation**! His scientific advises and numerous discussions significantly contributed to the progress of my work. Without his support, this thesis would have not been accomplished, I have learned a lot from you!

Thanks *everyone* else in the Materials Chemistry and Materials Sciences & Engineering groups for being an excellent work family. I won’t name you all, but thanks especially to *Prof. Ukai, Prof. Ohnuki, Prof. Koizumi, Prof. Fushimi, Prof. Habazaki, Prof. Kikkawa* and *Prof. Murakoshi* for always being happy and helpful, and for giving some “stability” to the group!

Mr. Endo and *Mr. Okubo* thanks for their help in using FIB and TEM facilities with characterization of many samples. Electronic Materials Chemistry lab-mates such an excellent place to work. Thanks for being more than friends; I look forward to meeting all of you outside Japan some day!

My *friends* from “outside the Materials Chemistry building”, thanks for all your friendship and support and for everything we have done and will do together. You mean very much to me! Finally, *my wife* and *my son* thanks for all your love and for believing much more in me than I do myself. *Mamma* and *Pappa* thanks for all support and caring. I couldn’t have had a better family!

Content	Page No.
Preface Acknowledgements	2
List of Content	3
List of Tables	5
List of Figures	5
CHAPTER 1: OUTLINE	
CHAPTER 2: INTRODUCTION	
2.1 BACKGROUND	16
2.2 FUNDAMENTALS ON OXIDATION	17
2.2.1. Metal-Oxygen Reactions	17
2.2.2 Kinetics of Oxidation	20
2.3 HIGH TEMPERATURE OXIDATION OF ALLOYS	25
2.3.1. External and Internal Selective Oxidation	25
2.4. Alumina	27
2.4.1. Alumina polymorphs	28
2.4.2. Alumina Forming Alloys	31
2.4.3. Factors affect the meta-stable alumina to stable α -Al ₂ O ₃ phase transformation	33
2.5. Objective and Strategy	36
2.6. References	37
CHAPTER 3: EXPERIMENTAL SET UP	
3.1. Sample Preparation	40
3.1.1. Alloy Making	40
3.1.2. Homogenization	41
3.2. Pre-coating Methods	42
3.2.1. Precoating by Physical Vapor Deposition	43
3.2.3. Precoating by Electrodeposition	44
3.3. Oxidation Tests	48
3.4. Surface and Cross-sectional Observations	49
3.4.1. Field Emission Scanning Electron Microscopy (FE-SEM)	49
3.4.2. Multi-beam System (Focused Ion Beam milling and FE-SEM imaging) (FIB)	51
3.4.3. Transmission electron microscopy (TEM)	53

3.5. Oxidation products phases' identification X-ray Diffraction Spectroscopy (XRD)	54
CHAPTER 4: EFFECTS OF NANO METALLIC PRECOATINGS ON GROWTH of Al₂O₃ SCALE FORMED ON NiAl ALLOY	
4.1. Introduction	58
4.2. Experimental details	59
4.3. Results and Discussion	61
4.3.1 Oxidation kinetics and products in the pre-oxidation stage	61
4.3.2. Oxidation kinetics and products of pre-oxidized samples at 1000 °C	67
4.3.2.1. Oxide scale evaluation at the early stage of oxidation	69
4.3.2.2. Oxide scale evaluation at the late stage of oxidation	69
4.4. Conclusions	85
4.5. References	85
CHAPTER 5: PROMOTION OF α-Al₂O₃ FORMATION ON AN Ni-Al ALLOY USING A Ni-Fe₂O₃ NANO-COMPOSITE PRECOATING LAYER	
5.1. Introduction	89
5.2. Materials and methods	90
5.3. Results and discussion	92
5.3.1. Properties of electrodeposited Ni and Ni-Fe ₂ O ₃ composite precoating layers	92
5.3.2. High temperature oxidation of Ni-coated and Ni-Fe ₂ O ₃ composite-coated Ni50Al samples	103
5.4. Conclusions	115
5.5. References	115
CHAPTER 6: EFFECTS OF Ni-Fe CO-DEPOSITED LAYER ON DIRECT α-Al₂O₃ FORMATION	
6.1. Introduction	120
6.2. Materials and methods	122
6.3. Results and Discussion	123
6.3.1. Properties of co-electrodeposited Ni, Ni-Fe and Fe precoating layers	123
6.3.2. High temperature oxidation tests of PED Ni, Ni-Fe and Fe precoating layers	132
6.4. Conclusions	150
6.5. References	151
CHAPTER 7: OXIDATION MECHANISM	
CHAPTER 8: CONCLUSIONS	

LIST OF TABLES

1. **Table 4.1.** Parabolic rate constants of oxide scale growth, k_p values, at 1000 °C
2. **Table 5.1.** PED conditions and resultant properties of Ni and Ni-Fe₂O₃ composite precoating layers
3. **Table 5.2.** Details of the detected XRD phases
4. **Table 6.1.** Details of the detected XRD phases
5. **Table 6.2.** Summary of the possible reactions during oxidation at 1000 °C in air
6. **Table 7.1.** Summary of the possible oxide properties that formed by oxidation of Ni50Al with different precoating layers
7. **Table 7.2.** Summary of alumina properties that formed at steady state of oxidation of Ni50Al with different precoating layers

LIST OF FIGURES

1. **Figure 2.1:** Standard Gibbs free energy change of formation of some selected oxides as a function of temperature (Ellingham-Richardson diagram) [1]
2. **Figure 2.2:** Schematic model for the nucleation and growth of oxide on a metal surface, the oxide grows laterally until the surface is covered with a thin oxide film [2]
3. **Figure 2.3:** Classification of different oxidation kinetics (linear, parabolic, logarithmic and inverse logarithmic)
4. **Figure 2.4:** Transport processes through a dense, single-phase scale growing by lattice diffusion. Transport of reacting ions is rate determining (a). And Transport processes in growing scale in terms of lattice and electronic defects, e.g. of metal vacancies and interstitial ions, electrons and electron holes (b) [2]
5. **Figure 2.5:** Schematics of the selective oxidation of A-B binary alloy for which both oxides are stable in the ambient environment but BO is more stable than AO. The alloy of B % is low and easy to be oxidized to form internal oxide scale (a), on the other hand where B % is medium (b) B% is high enough and sufficient to form a continuous external scale beneath the initially transient AO (c) [11]
6. **Figure 2.6:** The compositional effect of B% on the oxidation of A-B alloy [12]

7. **Figure 2.7:** Temperature transformation of hydroxides or oxohydroxides to corundum via the formation of transitional alumina phases [13].
8. **Figure 2.8:** The α -alumina hexagonal unit cell (a) and the θ -alumina monoclinic unit cell (b), examples of tetra and octahedral Al positions are indicated
9. **Figure 2.9:** Arrhenius plot of the parabolic rate constants k_p of β -NiAl oxidation [46]
10. **Figure 3.1.1:** Argon arc melting system
11. **Figure 3.1.2:** Vacuum tube furnace
12. **Figure 3.2:** Physical Vapor Deposition system
13. **Figure 3.3:** Potentiostat (Ivium Technologies Co., model Iviumstat) (a) and an electrochemical deposition three-electrode cell (b)
14. **Figure 3.4.1:** Super furnace (a), furnace's temperature calibration for 1 cycle of $10^\circ\text{C}/\text{min}$. heating rate and 1 h holding time at 1000°C (b)
15. **Figure 3.4.2:** JEOL JSM-6500F Field Emission Scanning Electron Microscopy (FE-SEM)
16. **Figure 3.4.3:** JIB-4600F/HKD focused ion beam milling and FE-SEM imaging device (Multi-beam FIB)
17. **Figure 3.4.4:** Micro Pickup System Micro Support Co., Ltd. Axis Pro)
18. **Figure. 3.4.5:** Transmission Electron Microscope Model JEM-2010
19. **Figure. 3.4.6:** JEOL jdx-3500 X-ray diffractometer
20. **Figure 4.1:** Schematic illustration of the oxidation cycles.
21. **Figure 4.2:** Oxidation mass gain of Ni-50Al with/without Ni, Cr or Fe precoating after pre-oxidation for 4 h at 900°C in air.
22. **Figure 4.3.1:** Surface morphology and corresponding XRD pattern of NiAl sample pre-oxidized for 4 h at 900°C .
23. **Figure 4.3.2:** Surface morphology and corresponding XRD pattern of Ni-coated NiAl sample pre-oxidized for 4 h at 900°C .
24. **Figure 4.3.3:** Surface morphology and corresponding XRD pattern of Cr-coated NiAl sample pre-oxidized for 4 h at 900°C .
25. **Figure 4.3.4:** Surface morphology and corresponding XRD pattern of Fe-coated NiAl sample pre-oxidized for 4 h at 900°C .
26. **Figure 4.4:** Oxidation mass gain of NiAl with/without Ni, Cr or Fe precoating (a)

for different time intervals at 1000 °C in air and (b) rate constant, k_p , calculations.

27. **Figure 4.5.1:** Surface morphology and corresponding XRD pattern of pre-oxidized NiAl sample (4 h at 900 °C) that was oxidized at 1000 °C for 4 h
28. **Figure 4.5.2:** Surface morphology and corresponding XRD pattern of pre-oxidized Ni-coated NiAl sample (4 h at 900 °C) that was oxidized at 1000 °C for 4 h
29. **Figure 4.5.3:** Surface morphology and corresponding XRD pattern of pre-oxidized Cr-coated NiAl sample (4 h at 900 °C) that was oxidized at 1000 °C for 4 h
30. **Figure 4.5.4:** Surface morphology and corresponding XRD pattern of pre-oxidized Fe-coated NiAl sample (4 h at 900 °C) that was oxidized at 1000 °C for 4 h
31. **Figure 4.6.1:** TEM cross-sectional morphology and corresponding XRD pattern of pre-oxidized NiAl sample (4 h at 900 °C) that was oxidized at 1000 °C for 100 h
32. **Figure 4.6.2:** TEM cross-sectional morphology and corresponding XRD pattern of pre-oxidized Ni-coated NiAl sample (4 h at 900 °C) that was oxidized at 1000 °C for 100 h
33. **Figure 4.6.3:** TEM cross-sectional morphology and corresponding XRD pattern of pre-oxidized Cr-coated NiAl sample (4 h at 900 °C) that was oxidized at 1000 °C for 100 h
34. **Figure 4.6.4:** TEM cross-sectional morphology and corresponding XRD pattern of pre-oxidized Fe-coated NiAl sample (4 h at 900 °C) that was oxidized at 1000 °C for 100 h
35. **Figure 4.7:** Dependence of the parabolic rate constant, k_p , of oxide scale growth of different precoating samples on grain size, r_G , of the Al_2O_3 scale formed after 100 h of oxidation. Dashed curve represents the fitting of the calculated k_p values from eqn. (12).
36. **Figure 4.8:** Effect of Cr addition on the oxidation growth rate constant of Ni50Al at 1200 °C
37. **Figure 5.1:** Current waveform for galvanostatic current pulse electrodeposition (PED) and potential response measured for electrodeposition of Ni on an NiAl alloy at $i_{cd} = -5 \text{ mA cm}^{-2}$, $t_{on} = 2 \text{ s}$, $t_{off} = 4 \text{ s}$ and $T = 25 \text{ °C}$ (Sample #1)
38. **Figure 5.2:** Surface and cross-sectional SEM images of an Ni-coating layer electrodeposited on NiAl with pulse conditions of $i_{cd} = -5 \text{ mA cm}^{-2}$, $t_{on} = 2 \text{ s}$, $t_{off} = 4 \text{ s}$ and $T = 25 \text{ °C}$ (Sample #1)

39. **Figure 5.3.1:** Surface morphology and cross-sectional SEM images of Ni-Fe₂O₃ composite precoating layers electrodeposited on Ni50Al for 450 s with pulse conditions of $i_{cd} = -5 \text{ mA cm}^{-2}$, $t_{on} = 2 \text{ s}$, $t_{off} = 4 \text{ s}$, 25 °C (sample #2)
40. **Figure 5.3.2:** Surface morphology and cross-sectional SEM images of Ni-Fe₂O₃ composite precoating layers electrodeposited on Ni50Al for 450 s with pulse conditions of $i_{cd} = -10 \text{ mA cm}^{-2}$, $t_{on} = 2 \text{ s}$, $t_{off} = 4 \text{ s}$, 25 °C (sample #3)
41. **Figure 5.3.3:** Surface morphology and cross-sectional SEM images of Ni-Fe₂O₃ composite precoating layers electrodeposited on Ni50Al for 450 s with pulse conditions of $i_{cd} = -5 \text{ mA cm}^{-2}$, $t_{on} = 2 \text{ s}$, $t_{off} = 2 \text{ s}$, 25 °C (sample #4)
42. **Figure 5.4.1:** Surface morphology and cross-sectional SEM images of Ni-Fe₂O₃ composite precoating layers electrodeposited on Ni50Al for 450 s with pulse conditions of $i_{cd} = -5 \text{ mA cm}^{-2}$, $t_{on} = 2 \text{ s}$, $t_{off} = 4 \text{ s}$, 45 °C (Sample #5)
43. **Figure 5.4.2:** Surface morphology and cross-sectional SEM images of Ni-Fe₂O₃ composite precoating layers electrodeposited on Ni50Al for 450 s with pulse conditions of $i_{cd} = -10 \text{ mA cm}^{-2}$, $t_{on} = 2 \text{ s}$, $t_{off} = 4 \text{ s}$, 45 °C (Sample #6)
44. **Figure 5.4.3:** Surface morphology and cross-sectional SEM images of Ni-Fe₂O₃ composite precoating layers electrodeposited on Ni50Al for 450 s with pulse conditions of $i_{cd} = -20 \text{ mA cm}^{-2}$, $t_{on} = 2 \text{ s}$, $t_{off} = 4 \text{ s}$, 45 °C (Sample #7)
45. **Figure 5.5:** XRD patterns of oxidized samples at 1000 °C for different oxidation times, t_{ox} : bare Ni50Al (a), Ni50Al coated with Ni (Sample #1) (b), Ni-3.1%Fe₂O₃ (Sample #2) (c), Ni-5.2% Fe₂O₃ (Sample #6) (d) and Ni-7.4 Fe₂O₃ (Sample #7) (e)
46. **Figure 5.6** Surface SEM and cross-sectional TEM images of bare Ni50Al after oxidation tests for 1 h (a, c), and 100 h (b, d)
47. **Figure 5.7.1** Surface SEM and cross-sectional TEM images of oxide scales formed on Ni50Al coated with Ni (Sample #1) layer after oxidation tests for 1 h at 1000 °C in air.
48. **Figure 5.7.2** Surface SEM and cross-sectional TEM images of oxide scales formed on Ni50Al coated with Ni-3.1%Fe₂O₃ (Sample #2) layer after oxidation tests for 1 h at 1000 °C in air
49. **Figure 5.7.3** Surface SEM and cross-sectional TEM images of oxide scales formed on Ni50Al coated with 5.2%Fe₂O₃ (Sample #6) layer after oxidation tests for 1 h at 1000 °C in air

50. **Figure 5.7.4** Surface SEM and cross-sectional TEM images of oxide scales formed on Ni50Al coated with Ni-7.4%Fe₂O₃ (Sample #7) layer after oxidation tests for 1 h at 1000 °C in air
51. **Figure 6.1:** Current waveform for galvanostatic PED and potential response measured for electrodeposition from Ni-bath including (0, 1.4 or 27.8) g dm⁻³ FeSO₄•7H₂O or Fe-bath containing 27.8 g dm⁻³ FeSO₄•7H₂O on an Ni50Al samples at $i_{cd} = -10 \text{ mA cm}^{-2}$, $t_{on} = 2 \text{ s}$, $t_{off} = 4 \text{ s}$ and $T = 25 \text{ °C}$
52. **Figure 6.2.1:** Surface and cross-sectional morphologies FE-SEM images of Ni on an Ni50Al samples, which was deposited for 600 s with pulse conditions at $i_{cd} = -10 \text{ mA cm}^{-2}$, $t_{on} = 2 \text{ s}$, $t_{off} = 4 \text{ s}$ and $T = 25 \text{ °C}$
53. **Figure 6.2.2:** Surface and cross-sectional morphologies FE-SEM images of Ni17 wt. %Fe, on an Ni50Al samples, which was deposited for 600 s with pulse conditions at $i_{cd} = -10 \text{ mA cm}^{-2}$, $t_{on} = 2 \text{ s}$, $t_{off} = 4 \text{ s}$ and $T = 25 \text{ °C}$
54. **Figure 6.2.3:** Surface and cross-sectional morphologies FE-SEM images of Ni72 wt. %Fe on an Ni50Al samples, which was deposited for 600 s with pulse conditions at $i_{cd} = -10 \text{ mA cm}^{-2}$, $t_{on} = 2 \text{ s}$, $t_{off} = 4 \text{ s}$ and $T = 25 \text{ °C}$
55. **Figure 6.2.4:** Surface and cross-sectional morphologies FE-SEM images of Fe on an Ni50Al samples, which was deposited for 600 s with pulse conditions at $i_{cd} = -10 \text{ mA cm}^{-2}$, $t_{on} = 2 \text{ s}$, $t_{off} = 4 \text{ s}$ and $T = 25 \text{ °C}$
56. **Figure 6.3:** XRD patterns of Ni-, Ni17 wt. %Fe-, Ni72 wt. %Fe- and Fe- coated Ni50Al samples, which were deposited for 600 s with pulse conditions at $i_{cd} = -10 \text{ mA cm}^{-2}$, $t_{on} = 2 \text{ s}$, $t_{off} = 4 \text{ s}$ and $T = 25 \text{ °C}$
57. **Figure 6.4:** Change of oxidation mass gain of bare Ni50Al, Ni-, Ni17 wt. %Fe-, Ni72 wt. %Fe- and Fe- coated Ni50Al samples in the oxidation tests at 1000 °C in air up to 100 h (a) up to 1 h (b)
58. **Figure 6.5:** Surface morphology FE-SEM images of bare Ni50Al (a), Ni- (b), Ni17 wt. %Fe- (c), Ni72 wt. %Fe- (d) and Fe- (e) coated Ni50Al samples after oxidation for 9 h at 1000 °C in air
59. **Figure 6.6:** XRD patterns of bare Ni50Al, Ni-, Ni17 wt. %Fe-, Ni72 wt. %Fe- and Fe- coated Ni50Al samples after oxidation for 9 h at 1000 °C in air
60. **Figure 6.7:** XRD patterns of Ni17 wt. %Fe for 0.5-7 h (a) Ni72 wt. %Fe for 30 to 420 min. (b) at 1000 °C in air

61. **Figure 6.8.1:** Cross-sectional TEM images of oxide scales formed on bare Ni50Al sample after oxidation for 9 h at 1000 °C in air
62. **Figure 6.8.2:** Cross-sectional TEM images of oxide scales formed on Ni-coated Ni50Al sample after oxidation for 9 h at 1000 °C in air
63. **Figure 6.8.3:** Cross-sectional TEM images of oxide scales formed on Ni17 wt. %Fe-coated Ni50Al sample after oxidation for 9 h at 1000 °C in air
64. **Figure 6.8.4:** Cross-sectional TEM images of oxide scales formed on Ni72 wt. %Fe- coated Ni50Al sample after oxidation for 9 h at 1000 °C in air
65. **Figure. 6.8.5:** Cross-sectional TEM images of oxide scales formed on Fe- coated Ni50Al sample after oxidation for 9 h at 1000 °C in air
66. **Figure 7.1:** Oxidation of bare NiAl early stage (a) and late stage (b) at 1000 °C in air
67. **Figure 7.2:** Oxidation of Ni-coated NiAl (a) Fe-coated NiAl (b) early and late stages at 1000 °C in air
68. **Figure 7.3:** Oxidation of Ni coated NiAl (a) 3.1%Ni-Fe₂O₃ coated NiAl (b) Ni-5.2% or 7.4%Fe₂O₃ coated NiAl (c) at 1000 °C in air
69. **Figure 7.4:** Oxidation of Ni17%Fe coated (a), Ni72%Fe coated (b) and Fe coated (c) NiAl at 1000 °C in air
70. **Figure 7.5:** Parabolic shapes of Oxidation Kinetics of NiAl with/ without precoating at 1000 °C in air

CHAPTER 1: OUTLINE

This thesis is comprised out of eight chapters:

***Chapter 1* OUTLINE**

***Chapter 2* INTRODUCTION**

***Chapter 3* EXPERIMENTAL SETUP**

In this thesis, effects of nano precoatings, including pure metallic Ni, Fe and Cr physical vapor deposition (PVD) coatings and pulsed electrodeposited metallic Ni and Fe, NiFe alloy and Ni-Fe₂O₃ composite coatings on the alumina scale formation and growth rate were studied. The coated samples were subjected to high-temperature oxidation test in air at 1000 °C. The oxidized samples were characterized by using field emission scanning electron microscopy (FE-SEM), X-ray diffraction (XRD), transmission electron microscopy (TEM) accompanied energy dispersive X-ray (EDX) point analysis.

***Chapter 4* EFFECTS OF NANO METALLIC PRECOATINGS ON GROWTH of Al₂O₃ SCALE FORMED ON NiAl ALLOY**

In this chapter, the effects of physical vapor deposition (PVD) pure metal precoatings, including Ni, Fe and Cr precoatings, of 50 nm in thickness on long-term oxidation kinetics, oxidation products, surface morphology and oxide scale structure were studied. Ni-50Al alloy and Ni-coated, Fe-coated and Cr-coated samples were pre-oxidized at 900 °C in air for 4 h. These pre-oxidized samples were then oxidized isothermally at 1000 °C in air. The oxidation kinetics of all samples showed parabolic

behavior, but the oxidation kinetics could be categorized into three different groups. The bare Ni-50Al alloy sample oxidized rapidly during the initial stage of oxidation due to the formation and growth of meta-stable θ -Al₂O₃, but the oxidation rate decreased after α -Al₂O₃ had developed. Oxidation of the Ni-coated sample was very slow from the beginning of oxidation even though the θ -Al₂O₃ scale was predominated for a longer oxidation time. Oxide scales formed on Ni50Al alloys with different precoatings in the high temperature pre-oxidation at 900 °C in air and oxidation test at 1000 °C in air were characterized by using X-ray diffraction (XRD), transmission electron microscopy (TEM) accompanied energy dispersive X-ray (EDX) point analysis. No θ -Al₂O₃ was developed on Cr and Fe-coated samples, but the oxidation rates of these samples were much faster than those of bare and Ni-coated samples. Cross-sectional images revealed that the grain size of α -Al₂O₃, which formed on Cr and Fe-coated samples, was much smaller than those of bare and Ni-coated samples. The difference in the grain size of α -Al₂O₃ was considered to be the reason for different growth rates of α -Al₂O₃ scales. Different metal precoatings affected the transformation behavior of meta-stable alumina to the α -Al₂O₃. These metal precoatings also affected the microstructure of α -Al₂O₃ and they showed a strong effect on the growth rate of α -Al₂O₃ in the steady-state oxidation stage.

Chapter 5 PROMOTION OF α -Al₂O₃ FORMATION ON Ni-Al ALLOY USING A Ni-Fe₂O₃ NANO-COMPOSITE PRECOATING LAYER

In this chapter, thin precoating layers of Ni and Ni-Fe₂O₃ composites were successfully formed on an Ni50Al alloy using the pulse electrodeposition method (PED) from a Watts bath in order to promote α -Al₂O₃ formation for improving high temperature

oxidation resistance of the Ni50Al alloy. The conditions for the PED and the effects of these precoating layers on Al₂O₃ scale formation on the Ni50Al alloy were investigated. The coated samples showed thicker oxide scales than bare Ni50Al samples in oxidation tests at 1000 °C in air. At the initial stage of oxidation (1 h), a single layer scale composed of blade-like crystals of meta-stable θ -Al₂O₃ was formed. The oxide scales formed on the PED coated samples had a multilayered structure consisting of an inner layer of either a mixture of θ -Al₂O₃ and α -Al₂O₃ or of single-phase α -Al₂O₃, intermediate NiAl₂O₄ layer and an outer NiO layer. The Ni-coating layer was found to delay the phase transformation of θ -Al₂O₃ to α -Al₂O₃ to 100 h of oxidation. Addition of 3.1%Fe₂O₃ to the Ni-coating layer accelerated the transformation of θ -Al₂O₃ to α -Al₂O₃ after 9 h of oxidation. Further addition of Fe₂O₃ nano-powder (5.2%~7.4%) to the Ni-coating layer successfully suppressed the θ -Al₂O₃ formation even at 1 h of oxidation. The Al₂O₃ phase structure and thickness of the oxide scales were found to be considerably affected by these precoating layers via two main factors: (i) formation of NiAl₂O₄ and (ii) the effect of Fe₂O₃ to accelerate the transformation of meta-stable Al₂O₃ to stable α -Al₂O₃ or to suppress the formation of meta-stable Al₂O₃.

***Chapter 6* EFFECTS OF Ni-Fe CO-DEPOSITED LAYER ON DIRECT α -Al₂O₃ FORMATION**

In this chapter, Ni, Fe metal or Ni-Fe alloy deposits were developed on Ni50Al alloy via pulsed electrodeposition (PED) technique. The effects of these metals or alloys precoating layers on the initial stage of oxidation behavior and oxidation products were studied at 1000°C in air atmosphere. The surface morphologies of the deposited layers and/or oxide scale were examined by using field emission scanning electron microscope

(FE-SEM) and transmission electron microscopy (TEM). The deposition and oxidation products were identified by using energy dispersive X-ray (EDX) and X-ray diffractometer (XRD). The surface morphology of the PED precoating layer depended on the Ni and Fe amount in deposits consequently; it affected the final oxidation products. The bare Ni50Al alloy oxidized rapidly during the initial stage of oxidation due to the formation of meta-stable θ -Al₂O₃. θ -Al₂O₃ was detected also for Ni-coated and Ni17%Fe-coated samples. θ -Al₂O₃ phases were not detected for Fe-coated and Ni72%Fe-coated samples at all oxidation times, but the oxidation mass gain on Fe-coated and Ni72%Fe-coated samples were higher than that on Ni50Al, Ni-coated and Ni17%Fe-coated samples. TEM cross-sectional images revealed that the grain size of α -Al₂O₃, which formed on Fe-coated and Ni72%Fe-coated samples, were smaller than those of bare Ni50Al and Ni-coated and Ni-17%Fe-coated samples. XRD and EDX point analysis confirmed the formation of different multilayered structure oxide scales on different oxidized samples. NiO/NiAl₂O₄/Al₂O₃ on Ni-coated, complex spinel Ni(Fe)Al₂O₄/Al₂O₃ on Ni17%Fe-coated, Fe₂O₃/ (Fe, Al)₂O₃/ α -Al₂O₃ on Ni72%Fe-coated and Fe₂O₃/ α -Al₂O₃ on Fe-coated samples. Introducing Fe or Ni72%Fe precoating layer prior to the oxidation of Ni50Al alloy resulted in suppression of θ -Al₂O₃ formation and influenced the microstructure of α -Al₂O₃, which reflected on oxide scale growth rate.

***Chapter 7* OXIDATION MECHANISM**

Effects of different PVD nano metal precoatings on the grain size of the α -Al₂O₃ were investigated and the effect of different grain sizes of the α -Al₂O₃ for different coated samples on the oxidation mass gain with/without residual θ -Al₂O₃ above this α -Al₂O₃ was clarified. An equation could be stated to correlate the grain size of the α -Al₂O₃ for

different coated samples and their oxidation growth rate constant. Then effects of introducing different amount of Fe_2O_3 nano powder to Ni as a PED Ni- Fe_2O_3 hybrid precoating layer on the phase structure and thickness of the oxide scales were investigated and the main factors, which may affect the oxide scale formation, were clarified. Afterword, effects of different Fe/Ni ratios in PED alloy deposits on the Al_2O_3 scale formation were studied and the main factors, which may affect the oxide scale formation, were clarified.

The $\alpha\text{-Al}_2\text{O}_3$, which formed on different coated samples, will be classified based on their oxide growth rate constants kp value, transformation time and the parabolic shape of their oxidation growth kinetics.

Different oxide phases, which may form during the oxidation process of different coated samples, will be categorized based on their metal cation-oxygen framework (oxygen sub-lattice).

***Chapter 8* CONCLUSIONS**

Chapter 2 INTRODUCTION

2.1 BACKGROUND

Two thirds of worldwide electricity is generated by thermal power plants, but it is also contributing in releasing carbon dioxide, which has greenhouse effect. The reduction of these emissions is of great importance and attracts interests of many scientists in last decades. Developing the constructing materials of high temperature applications like thermal power plants could help in the enhancement of the operation efficiency and elongate the maintenance periods. Which in turn, reflects economically on reducing the operation costs and also environmentally on reducing hazardous emissions. To apply high temperature resistive materials or alloys to practical use, special service requirements are needed depending on applications. Extension of operating temperature, pressure and mechanical loading of high temperature resistive materials are essentials to achieve an efficient high temperature application. Somehow to do so, neither environmental nor economical restrictions allow that.

Dense protective chromia, silica or alumina scales may form at such high temperatures on Fe- or Ni- based superalloys and they meet high temperatures applications requirements. However use of chromia formers is limited at temperature lower than 1000°C because of its evaporation property. Alumina formers is an excellent alternative candidate to take over the higher temperatures limitation because alumina doesn't evaporate up to its melting point at 2051°C. Although alumina scale is applicable to a wide range of temperature, it has a drawback. The problem of the usage of alumina scale is the initial formation of many undesired meta-stable phases (at lower temperatures or shorter oxidation duration). These meta-stable phases take long time until complete

transformation to stable alumina phase. The transformation from meta-stable phases to the stable phase leads to shrinkage in the oxide scale due to compressive stresses and results in spallation and breaking down of the scale. Therefore, rapid formation of stable alumina phase at the initial stage of oxidation is needed. This could be achieved by either suppression of meta-stable phase formation or acceleration of transformation from meta-stable to stable alumina.

2.2 FUNDAMENTALS ON OXIDATION

2.2.1 Metal-Oxygen Reactions

When metal (M) exposed to air a chemical reaction with oxygen will proceed and could be expressed as,



The possibility of occurrence of this chemical reaction is governed by the Gibbs free energy change during the reaction. The change in Gibbs free energy ΔG determines the reaction direction. When the reaction is in equilibrium the value of ΔG is zero, when $\Delta G < 0$ the reaction occurs in direction of the products and when $\Delta G > 0$ the reaction will occur in direction of the reactants. In high temperature oxidation process the temperature and total pressure are constant as a result the driving force for the reaction is the Gibbs free energy change ΔG .

The Gibbs free energy change; ΔG , is given by,

$$\Delta G = \Delta G_0 + RT \ln K \quad (2)$$

Where, ΔG_0 is the standard Gibbs free energy change for the reaction, R is the gas constant, T is the kinetic temperature in Kelvin and K is the equilibrium constant.

In equilibrium (i.e. $\Delta G = 0$), the equation (2) becomes,

$$\Delta G_0 = - RT \ln K \quad (3)$$

The equilibrium constant K is the ratio of the activities of the products to reactants (law of mass action) and can be written as,

$$K = a_{M_x O_y} / a_M^x (p_{O_2})^{y/2} \quad (4)$$

Where, $a_{M_x O_y}$, a_M^x are the activities of metal oxide and metal, p_{O_2} is the oxygen partial pressure. Taking into account that the activities of pure, condensed phases are one and replacing of equation (4) in (3) becomes,

$$\Delta G_0 = - RT \ln (p_{O_2})^{y/2} \quad (5)$$

From equation (5), the partial pressure of the metal oxide formation could be determined. This value is the threshold value for the metal oxide formation *i.e.*, if the oxygen pressure exceeds this value at the temperature in equation, an oxide will form. The relation between standard Gibbs free energy change and temperature is used to estimate the equilibrium oxygen potentials via the Ellingham-Richardson diagram, as shown in **Fig. 2.1**.

The scale on the right side of the diagram (**Fig. 2.1**) labeled ' p_{O_2} ' is used to determine the equilibrium oxygen partial pressure with both the metal and metal oxide at a given temperature. By drawing a straight line from the origin point '+' (upper left corner of the diagram) through the free energy line at the temperature of interest and

reading the oxygen pressure from its intersection with the scale at the right side ' P_{O_2} ', the equilibrium oxygen partial pressure could be determined.

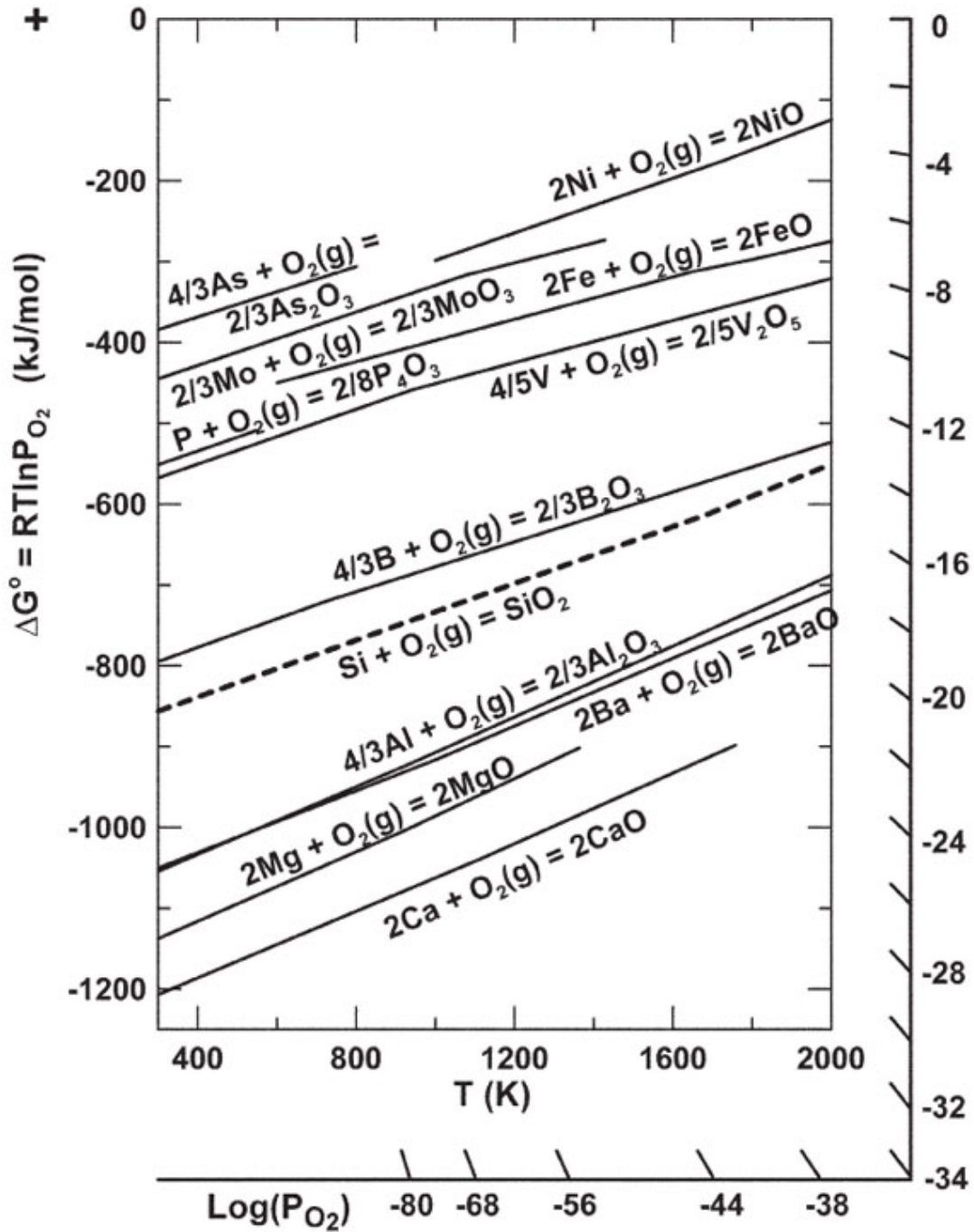


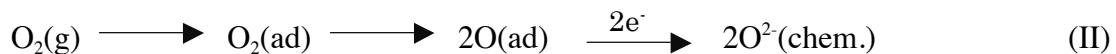
Figure 2.1: Standard Gibbs free energy change of formation of some metal oxides as a function of temperature (Ellingham-Richardson diagram) [1]

2.2.2 Kinetics of Oxidation

The stability of oxides and the possible oxide phases, which may form during the oxidation process, could be determined by thermodynamical calculations by calculating the equilibrium oxygen partial pressure and the formation Gibbs free energy. However, in the rapid heating cycles, the oxide growth is controlled by kinetics. The initial stages of metal-oxygen reaction involve the following steps:

- (i) Adsorption (attachment) of oxygen and surface reaction
- (ii) Oxide nucleation (heterogeneous or homogenous)
- (iii) Lateral growth (coverage)

Initially, oxygen adsorption takes place before its partial pressure of oxide formation is reached the threshold value. Then, the adsorbed oxygen molecules divided to form adsorbed oxygen, which attracts electrons from the lattice to become initially chemisorbed and finally incorporated into the lattice. This process can be represented as follows [1]



The surface is covered by adsorbed oxygen by increasing the oxygen partial pressure. When a metal surface saturated with oxygen and further oxygen is supplied, oxide nuclei are formed on the surface. The oxide nuclei grow laterally to form a continuous oxide film on the surface. A model for such a growth process is shown in **Fig. 2.2.**

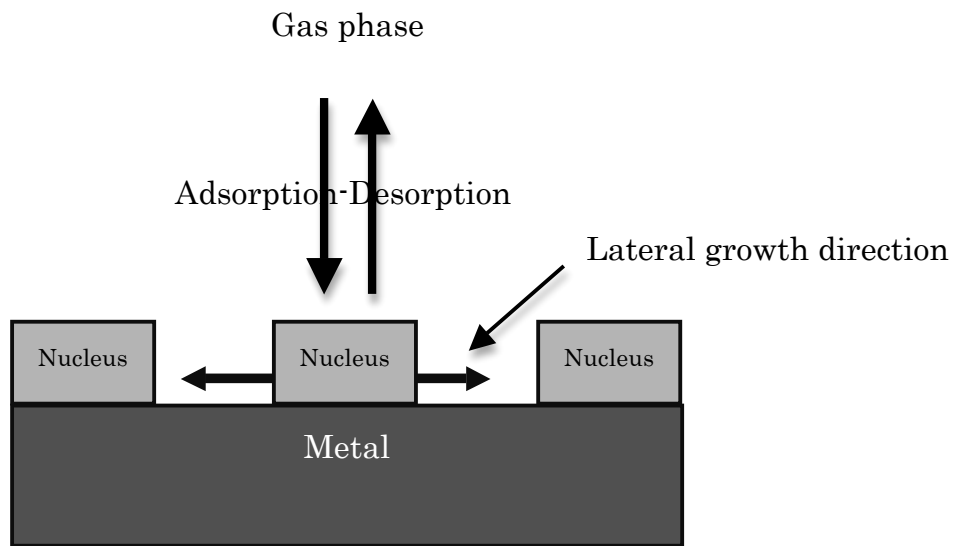


Figure 2.2: Schematic model for the nucleation and growth of oxide on a metal surface, the oxide grows laterally until the surface is covered with a thin oxide film [2]

When the oxide nuclei are grown laterally together, the surface oxides separate the metal from the gas phase. Because of the formation of a continuous film on the metal surface, the reaction can proceed only via the solid-state diffusion of the reactants through the film. As mentioned above, for very thin oxide scales, the electric fields across the film is the driving force for the reactants transport while, for thick oxide scales, it the chemical potential gradient across the scale is the driving force for thermal diffusivity of cations and anions. The oxidation process mechanism is rather complex and depends on a variety of factors such as pre-treatment or surface preparation and oxidation temperature, atmosphere, oxygen partial pressure, and oxidation time. For simplicity, the oxidation kinetics could be classified in different three categories shown in **Fig. 2.3**.

In linear rate law, the oxidation of metals proceeds at a constant rate and may be described by,

$$X = k t \quad (6)$$

Where X represent the thickness of the oxide film, t denotes the time and k represents the linear rate constant. In this case, the following phase boundary reactions are rate determining:

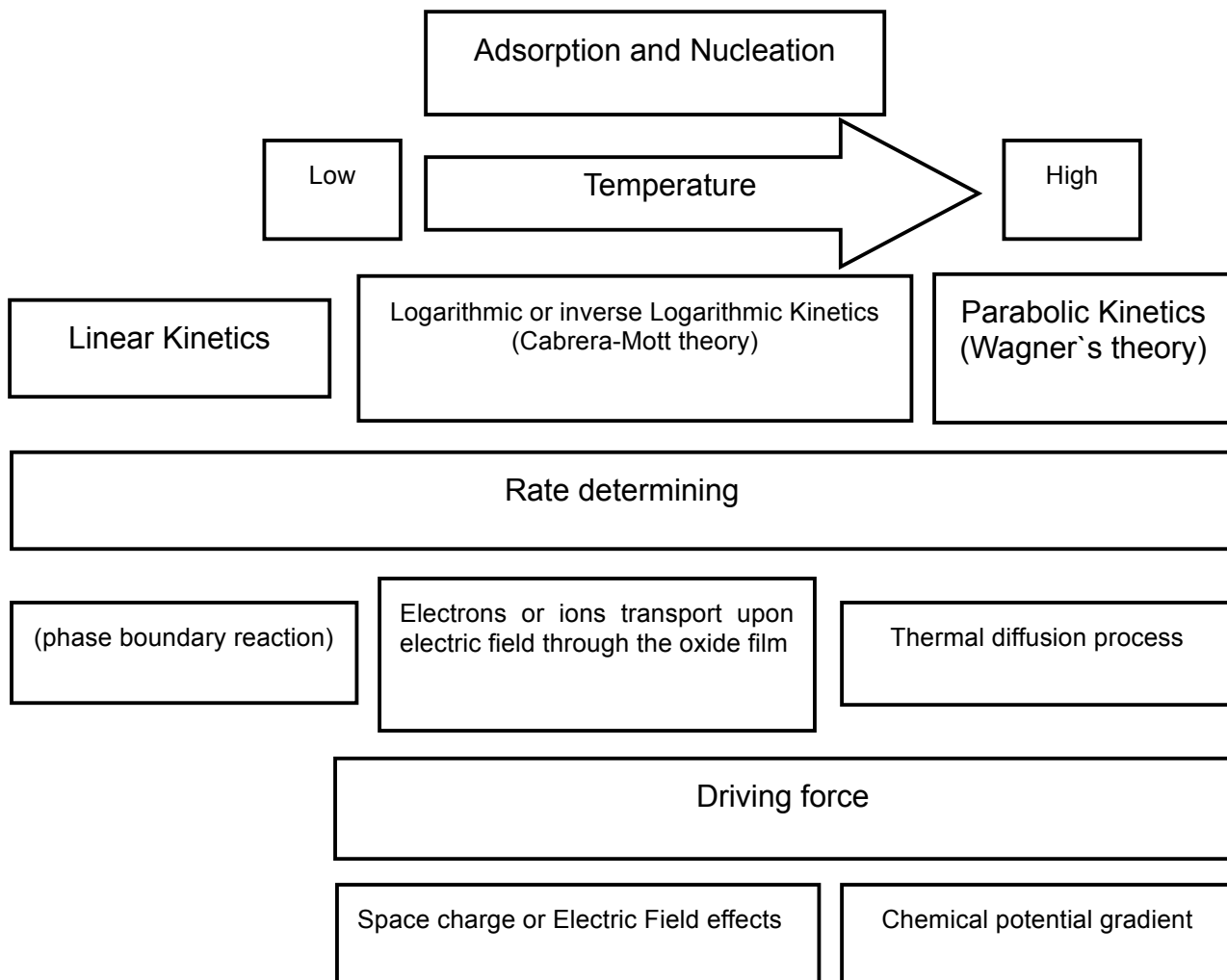


Figure 2.3: Classification of different oxidation kinetics (linear, parabolic, logarithmic and inverse logarithmic)

By further oxidation time, oxide nuclei form on a metal surface, as shown in **Fig. 2.2**. Subsequently, an oxide film is formed on the surface and the kinetics of oxidation is controlled by diffusion in the layer, with a parabolic behavior. The parabolic equation is given by,

$$X^2 = 2k_p t \quad (7)$$

Where, k_p denotes the parabolic rate constant.

At lower temperatures and in the case of very thin oxide films of thickness ($X < 10\text{nm}$), Cabrera-Mott theory (inv. log/log rate law) governs the oxidation process where the electric field across the film or space charges in the film caused by the oxygen chemisorption on the oxide surface is considered to be the driving force for the oxide formation [3]. Oxygen molecules desorb and adsorb on the surface and thereby give rise to traps with energy below the Fermi level of the metal. This gives a potential drop V across the film and thereby a field ($F = V/X$) is established in the oxide. Mott in ref. [4] originally assumed that electron tunneling through the film is rate determining and these results in a direct logarithmic rate equation:

$$X = k \log t + A \quad (8)$$

One of the basic assumption of the Cabrera-Mott theory is that the activation energy W necessary for the cation to move is reduced by the strong field to $W - qaF/2$ where, q is the charge on the cation and a is the jump distance, this assumption sounds like the Schottky-effect in semiconductors. But in Schottky-effect, the energy of electrons is considered that is different from the present case. If the transport of cations through the film is rate determining, this assumption results in the inverse logarithmic rate equation.

$$l/X = B - k \log t \quad (9)$$

The fundamental theoretical work on parabolic oxide scale growth for high temperature oxidation of metals and alloys was done by Carl Wagner [5]. Wagner assumed that a porous-free dense oxide scale that is well adhered to a metal surface is formed. The solubility of oxygen in the metal is limited. There are no space charge effects across the oxide and at the metal/oxide or oxide/gas interfaces. Thermodynamic equilibrium is established locally through the scale and at interfaces or boundaries.

And the most important assumption of Wagner`s theory is that lattice diffusion of cations and/or anions associated with the transport of electrons through the dense scale are rate determining in the overall oxidation reaction as mentioned above in **Fig. 2.3**. The schematics of the ionic migration process are shown in **Fig. 2.4**.

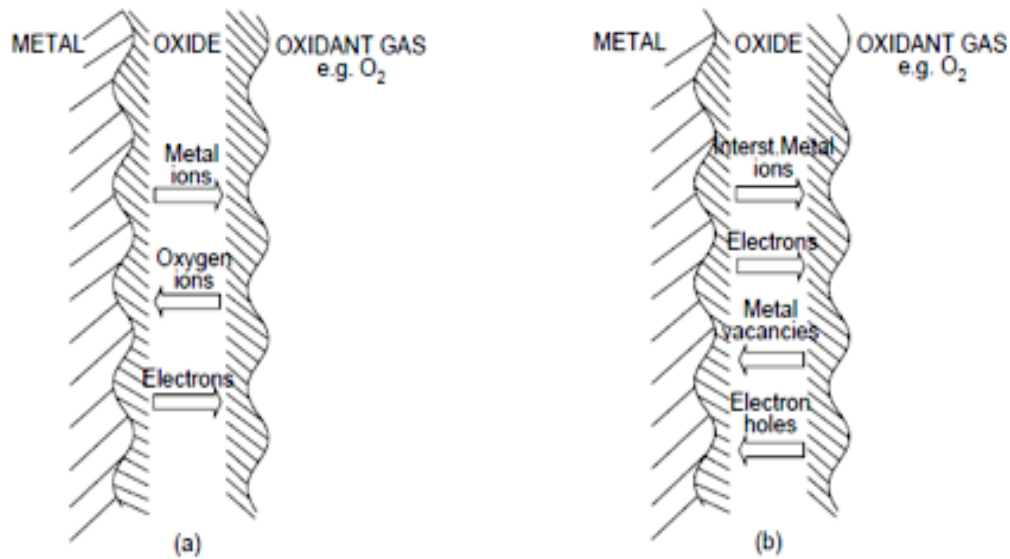


Figure 2.4: Transport processes through a dense, single-phase scale growing by lattice diffusion. Transport of reacting ions is rate determining (a). And Transport processes in growing scale in terms of lattice and electronic defects, e.g. of metal vacancies and interstitial ions, electrons and electron holes (b) [2]

Both of outward diffusion of cations and/or the inward diffusion of oxygen ions are contributing for the oxide scale growth. Which of these two diffusion processes is rate determining or domination the oxidation kinetics, this depends on the mobility of migrating ions in the system. The most important outcome of Wagner's analysis is the possibility to obtain complete information about the mechanism of the process (using the dependence of anion and cation conductivities on oxygen partial pressure and the dependence of diffusivities on oxygen partial pressure [1]).

2.3 HIGH TEMPERATURE OXIDATION OF ALLOYS

2.3.1. External and Internal Selective Oxidation

Selective oxidation is defined to the preferential oxidation of the less noble elements in an alloy. According to Wagner's theory, the selective oxidation can be categorized into two types, external oxidation and internal oxidation [6-10]. In highly Al % alloys, the oxide scale is formed on the alloy surface and it is called an external selective oxidation process. In this case, this oxide scale prevents the oxidation of the parent metal, i.e. oxidation resistive oxide scale. On the other hand, the internal oxide scale or precipitations of one or more of alloying elements are formed beneath the alloy surface when the oxygen diffuses into an alloy and it is called an internal selective oxidation process. Schematic models of external and internal oxidation in the case of a binary alloy A-B oxidation, where B is a dilute solute that forms a very stable oxide are shown in **Fig. 2.5**. Pettit [12] assessed the oxidation behavior of Ni–Al alloys over the temperature range 900–1300 °C and categorized the oxide scales into three groups, as shown in **Fig. 2.6**. Group I represents the internal oxidation of Al, with external formation

of NiO doped with Al. Group II represents the alloys that contain enough Al and able to form an external α -Al₂O₃ layer, but this depletes the surface to the point at which, if the scale breaks down in some manner, NiO and NiAl₂O₄ may be formed. A protective Al₂O₃ layer may reform in time, but a multilayered scale develops as these processes repeat. With higher Al content, an exclusive Al₂O₃-scale layer is established and maintained that represents Group III. **Figure 2.6** shows that an increase in the oxidation temperature helps to promote external Al₂O₃ formation (i.e., the necessity of Al content for the transition from Group I to Group II decreases with increasing temperature) and of course it depends on the oxygen partial pressure during oxidation.

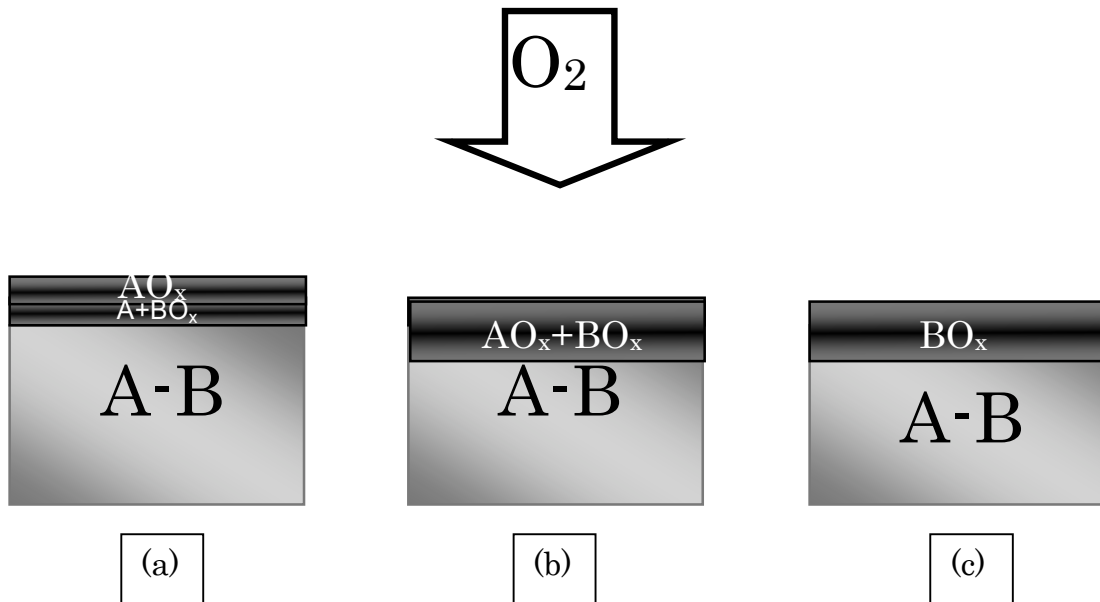


Figure 2.5: Schematics of the selective oxidation of A-B binary alloy for which both oxides are stable in ambient but BO_x is more stable than AO_x. The alloy of B% is low and easy to be oxidized to form internal oxide scale (a), on the other hand where B% is medium (b) B% is high enough and sufficient to form a continuous external scale beneath the initially transient AO_x (c) [11]

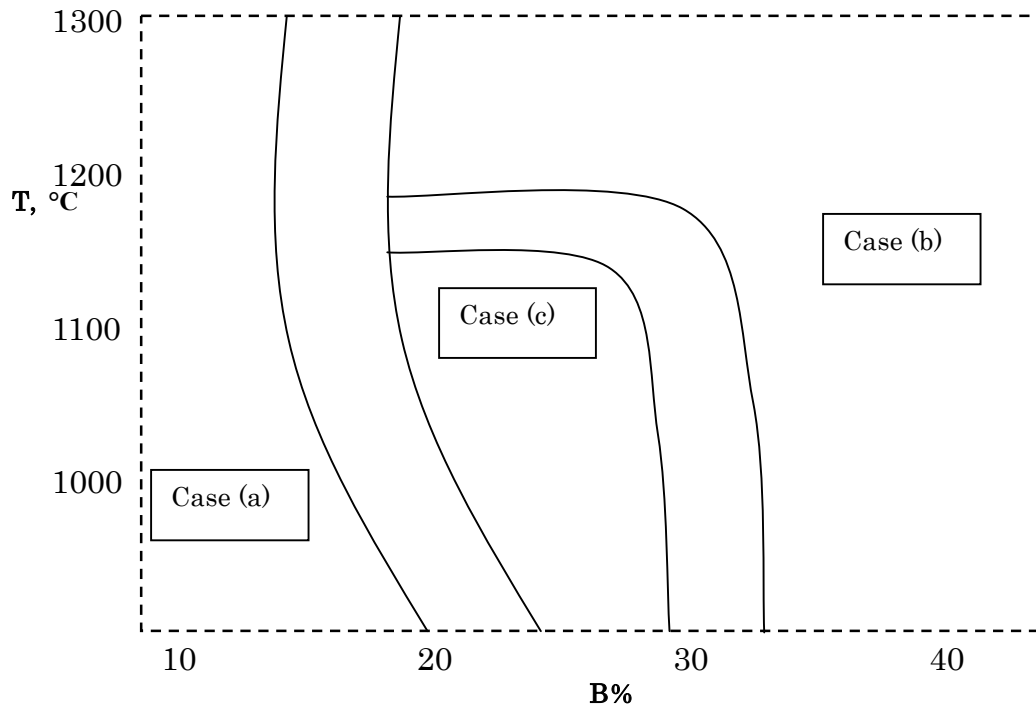


Figure 2.6: The compositional effect of B% on the oxidation of A-B alloy [12]

2.4. Alumina

Alumina has many appealing properties, which makes the material interesting for applications in many different areas. For example, it is hard, stable, insulating, transparent, etc. This section describes briefly the complexity of alumina crystalline phases and reviews the properties of the two phases that are encountered in this work. **Fig. 2.7** shows the paths of transition Al_2O_3 during the heat treatment processes [13]. Beside stable $\alpha\text{-Al}_2\text{O}_3$, there are other forms of meta-stable Al_2O_3 structures, such as η , χ , κ , γ , δ and $\theta\text{-Al}_2\text{O}_3$.

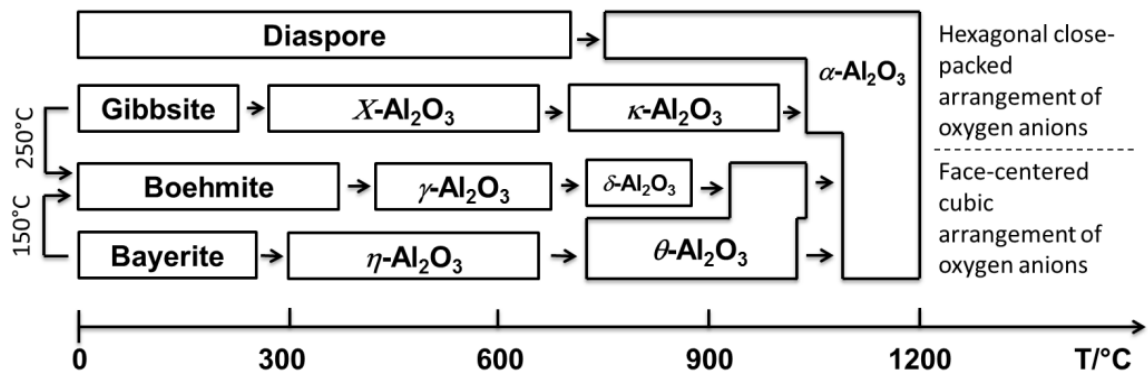


Figure 2.7: Temperature transformation of hydroxides or oxohydroxides to corundum via the formation of transitional alumina phases [13]

2.4.1 Alumina polymorphs

Alumina exists in many crystalline phases or polymorphs such as meta-stable η , χ , κ , γ , δ and θ - Al_2O_3 , and stable α - Al_2O_3 . Only α structure is thermodynamically stable at all temperatures up to Al_2O_3 melting point at 2051°C , but the other meta-stable phases appear initially (lower temperatures or shorter time) by oxidation of alumina forming alloys. All alumina polymorphs can be formed within typical synthesis temperatures, *i.e.*, from room temperature up to about 1000°C as shown above in **Fig. 2.7**. Somehow the controllability of alumina growth is rather complicated than it is expected because of the formation of more than one alumina phase at the same time. But the polymorphism also opens many opportunities for applications in various areas of technical science, since the properties of one alumina phase in some respects differ from the properties of another.

Properties of corundum α -alumina

α form of aluminum oxide is also known as *corundum* (the name comes from the naturally occurring mineral corundum, which consists of pure α -Al₂O₃). It is transparent and uncolored and is known in its single crystal form as *sapphire*. It is used not only in materials science, but occurs also as gemstones. The gem known, as ruby is α -alumina doped with small amounts of chromium, while the gemstone sapphire is actually α -alumina doped with iron and titanium.

The corundum structure is also formed by a number of other metals, such as Cr₂O₃, Ti₂O₃, and Fe₂O₃ [14]. The structure belongs to space group $R3c$ and is rhombohedral with two formula units (10 atoms) in the primitive unit cell. However, a more often-used unit cell is the hexagonal representation containing six formula units. The c axis of the hexagonal cell is along the (111) direction of the rhombohedral lattice. The corundum structure can be described as a hexagonal close-packed (hcp) oxygen sub lattice, in which the aluminum atoms, or ions, occupy two thirds of the octahedral interstices, i.e., they have six oxygen nearest-neighbors. There is thus only single coordination (octahedral) for aluminum and one for oxygen (with four surrounding aluminum ions) as shown in **Fig 2.8a**. Thus the thermodynamic stability of α -alumina makes it the most suited phase for use in many high-temperature applications.

Properties of θ -alumina

θ phase of alumina is meta-stable and transforms into the α phase at about 1050°C. It is less dense than the θ phase with a density of about 3600 kg/m³ compared to 4000 kg/m³ for α -alumina [15]. The structures of all alumina phases are built up around (slightly distorted) close-packed oxygen lattices and while the α phase has an hcp

framework, the θ structure is based on an fcc oxygen lattice [16]. Within this oxygen framework, half the aluminum ions occupy octahedral interstitial sites and half occupy tetrahedral (with four oxygen neighbors) sites, as shown in **Fig. 2.8b**. This is also in contrast to the α phase. The oxygen ions have three different possible surroundings, each of which is occupied by one third of the oxygen ions. Two of these oxygen sites there have three aluminum nearest-neighbors and the third has four. The structure is monoclinic, belonging to space group $C2/m$, and the unit cell contains four formula units (20 atoms). θ -alumina is a structural isomorph of $\beta\text{-Ga}_2\text{O}_3$ and, interestingly, gallium oxide can also form the corundum structure.

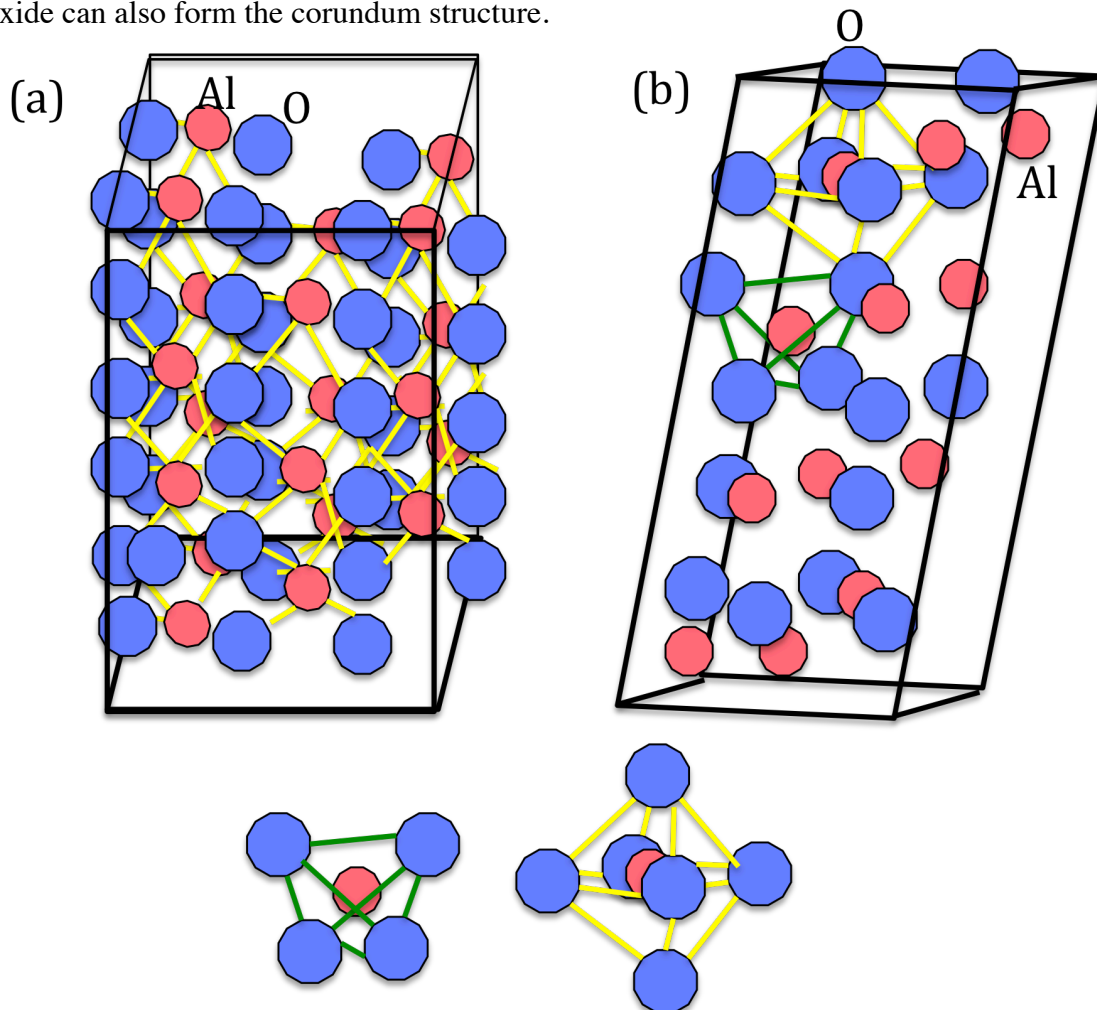


Figure 2.8: The α -alumina hexagonal unit cell (a) and the θ -alumina monoclinic unit cell (b), examples of tetrahedral and octahedral Al positions are indicated.

2.4.2 Alumina Forming Alloys

Many research works have been done on the development of the protective α - Al_2O_3 scales. The Alumina forming alloys were studied with or without reactive elements additions. NiAl, CoAl and FeAl have been used widely as a diffusion coating for gas turbines [17-20]. Also, FeCrAl alloys have an oxidation resistance due to the formation of alumina scales that suitable for the alloy protection up to 1300°C. This kind of alloys has been used for fabrication of components working at high temperatures: heating elements, fire grid and honeycomb catalytic converters for automotive exhausts. Mainly, the oxidation temperature is the most effective factor on the oxidation process of the alumina formers; higher temperature means stable alumina phase formation. Also, Aluminum content is significantly affecting the development of the continuous alumina scale.

Different morphologies of alumina scales, grown on FeCrAl alloys, are described in the literature. The oxide layer is usually α - Al_2O_3 , but a sub-layer of γ - Al_2O_3 was also detected, after an oxidation carried out below 900°C and the scale growth rate was higher at 1000°C [21]. Oxidation in air at 1100-1200°C of FeCrAl brought the formation of a structured alumina film, characterized by equi-axed grains on the outer surface and a columnar structure inside the layer [21, 22], as well as to a planar multi-layer oxide coating [23]. A higher concentration of alloying elements up to 1at.% is believed to cause the formation of pegs, made of Sc_2O_3 or Y_2O_3 and protruding into the alloy [24]. An almost flat scale/gas interface was usually observed, even though protrusion of alumina whiskers or filaments occurred by oxidation at 1200°C of FeCrAl without rare earth alloying elements or oxidation at 900°C of doped-FeCrAl [21, 24].

Because of its high melting point and excellent oxidation resistance, NiAl is a material of great interest in high-temperature applications. This intermetallic phase with ordered B2-structure has a wide homogeneity range which varies over 20 at.% at 1000°C [25]. As yet NiAl is used mainly as a base material for oxidation resistant coatings on high temperature alloys. Renewed interest has arisen because of improvements in mechanical properties [26] and now it is intended to use NiAl in structural applications. Therefore, after earlier investigations, [27-29] its oxidation behavior has been reinvestigated in recent years [30, 31]. Because of its high aluminum activity, NiAl forms only the oxide Al_2O_3 upon high temperature oxidation. Moreover, the adherence of the Al_2O_3 scale can be improved significantly by the addition of platinum. The addition of Pt to an Al_2O_3 -scale forming alloy has been known to improve scale adhesion since the 1970s [32, 33]. However, despite numerous studies of Pt-modified aluminides [34], the exact mechanism by which Pt improves the coating performance is still not well understood. It has been proposed that Pt may interact with indigenous sulfur, reduce the growth rate of interfacial voids [35, 36], or limit the outward diffusion of minor alloying elements (e.g., Ti, Ta, Re, etc.) from the superalloy substrate [37], all of which would serve to improve scale adhesion.

2.4.3 Factors affect the meta-stable alumina to stable α - Al_2O_3 phase transformation

There has been much research into the development of protective α - Al_2O_3 scales [38-39] on Al-containing alloys. A critical factor is the Al content in the alloy or coating, which must be sufficiently high to develop and maintain an alumina layer and prevent subsequent breakaway oxidation. A further critical factor is the oxidation temperature, which must be high enough to promote the formation of α - Al_2O_3 in preference to the faster growing transition alumina phases that form during a certain transient stage of oxidation at temperatures below about 1100 °C (e.g., during heating). At lower temperatures and/or in the early stages of oxidation, the meta-stable oxides γ - Al_2O_3 , δ - Al_2O_3 and θ - Al_2O_3 grow. The meta-stable, transitional Al_2O_3 structures often grow as blades or whiskers [40], and their growth can affect considerably the overall amount of oxidation and the subsequent growth of the stable α - Al_2O_3 phase. These phases contain a high concentration of cation vacancies. For example, eventual transformation from meta-stable θ - Al_2O_3 to α - Al_2O_3 produces an 8–13% volume reduction, which results in apparent tensile stresses in the scale [41, 42] and scale cracking [43].

The change of oxidation rate constants; k_p , by about two orders of magnitude was observed by several authors [30, 44, 45]. The described sequence of phase formations and transformations, involving the meta-stable relatively fast growing γ - Al_2O_3 and δ - Al_2O_3 in fact is undesirable, but it can be widely suppressed by alloying additions in NiAl, such as Cr and rare earth elements. The data for pure NiAl are compiled in the Arrhenius-diagram **Fig. 2.9**, which shows the Arrhenius lines for the formation of the three mentioned Al_2O_3 phases. Because of its slow growing rate and thermodynamically stability, α - Al_2O_3 is preferred to form from the beginning or to be developed by

acceleration the transformation from meta-stable alumina phases.

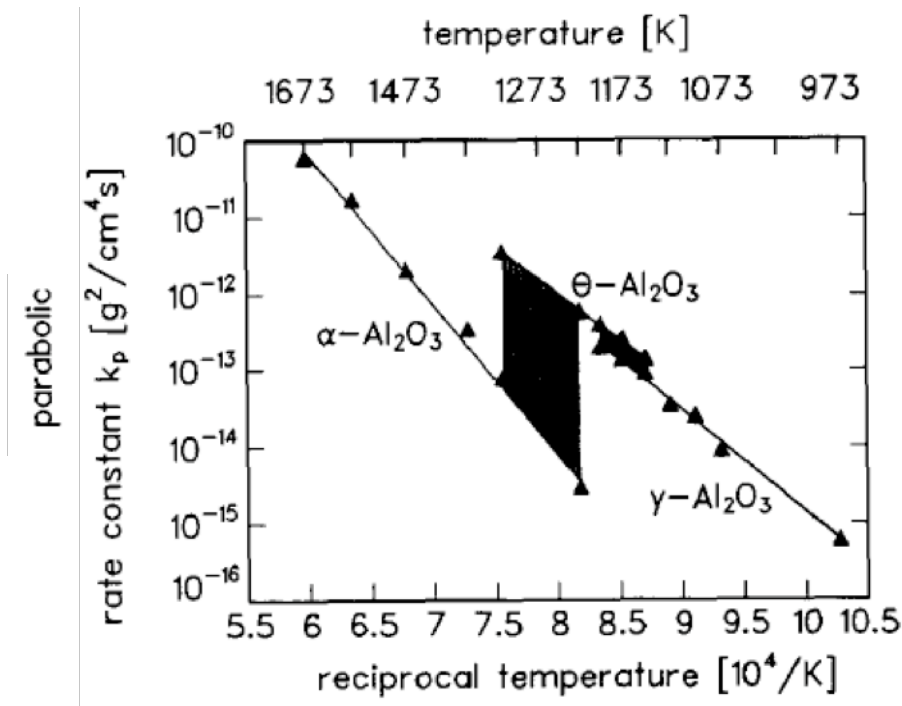


Figure 2.9: Arrhenius plot of the parabolic rate constants k_p of β -NiAl oxidation [46]

Reactive elements (REs) such as Y, Zr, La, and Hf are often used in high temperature alloys in order to improve their oxidation resistance, by improving scale adhesion and slowing the rate of oxide-scale growth during exposure to higher temperatures. However, doping of REs often causes delay in the meta-stable to α - Al_2O_3 phase transformation, and this delay results in a greater growth rate of Al_2O_3 scales, particularly during the initial stage of oxidation [47]. Addition of certain amounts of various metals is known to affect the Al_2O_3 scale properties. Doping the alloy with less than 0.1% of REs was reported [48, 49]. Addition of Cr or Fe is known to accelerate the transformation to α - Al_2O_3 . This beneficial effect on the phase transformation is thought to be due to the isomorphism of the metal oxides and α - Al_2O_3 , which are formed at the

initial stage of oxidation [50].

It is also believed that Fe accelerates the transformation of meta-stable Al_2O_3 to stable $\alpha\text{-Al}_2\text{O}_3$ due to an isomorphism effect of Fe_2O_3 to $\alpha\text{-Al}_2\text{O}_3$, suggesting that Fe_2O_3 can act as a “template” for the $\alpha\text{-Al}_2\text{O}_3$ scale formation [51-55]. Kitajima *et al.* reported that a very thin Fe-precoating ($\sim 50\text{nm}$) could suppress meta-stable Al_2O_3 formation on Fe-50Al and Ni-50Al alloys by oxidation in air at the relatively low temperature of 900 °C. They emphasized the beneficial effects of pre-deposition of Ti, Cr, and Fe on an Fe-50Al and Ni-50Al alloys to form Ti_2O_3 , Cr_2O_3 , and Fe_2O_3 prior to the Al_2O_3 scale growth [56, 57].

Hayashi *et al.* proposed another mechanism whereby $\alpha\text{-Al}_2\text{O}_3$ precipitates from the Al-saturated Fe_2O_3 , which was formed during initial stage of oxidation by oxidation of Fe-precoating layer. Effects of metal precoatings, different Al contents and/or different oxidizing atmosphere conditions on the transformation behavior of Al_2O_3 scale during high temperature oxidation by in-situ HT X-ray diffraction by means of synchrotron radiation were studied extensively in Ref. [58, 59]. In their study, in-situ measurements were made of structural changes in the oxide scales formed on FeAl with and without Fe precoating during heating and subsequent isothermal high temperature oxidation by synchrotron radiation with a two-dimensional X-ray detector. The results of this study suggest that the $\alpha\text{-Al}_2\text{O}_3$ was formed not only by precipitation from the Al-saturated Fe_2O_3 , but also by oxidation of Al in the substrate [58]. In another study, effects of introducing very thin (100 nm) Fe precoating on the phase transformation of Al_2O_3 scale on binary Fe–Al alloys with various Al content in different oxygen partial pressures were investigated by in situ HT X-ray diffraction by means of synchrotron radiation [59]. Hayashi *et al.* found that not only Fe-precoating can effectively suppress meta-stable

Al_2O_3 formation, but also the oxygen partial pressure (PO_2) can play a role. Under the low PO_2 atmosphere, meta-stable to stable $\alpha\text{-Al}_2\text{O}_3$ scale phase transformation on Fe–Al alloys with or without Fe-precating was significantly delayed. Higher Al content in Fe-52Al was found to delay the transformation of meta-stable Al_2O_3 to stable $\alpha\text{-Al}_2\text{O}_3$ at 1100 °C. It was also speculated that FeAl_2O_4 spinel scale formation on the Fe coated alloy in $\text{H}_2\text{-H}_2\text{O}$ stabilize meta-stable $\theta\text{-Al}_2\text{O}_3$ phase.

2.5. Objective and Strategy

Based on the literature presented here, the purpose of this study was an attempt to develop a stable $\alpha\text{-Al}_2\text{O}_3$ phase exclusively without any of meta-stable alumina phases from the beginning of high temperature oxidation of NiAl alloy in air moreover, slowing down the growth rate of this directly formed $\alpha\text{-Al}_2\text{O}_3$. The approach to solve the problem of undesired Al_2O_3 meta-phases formation is to clarify the correlation between long-term oxidation kinetics and oxidation products from one side and the Al_2O_3 scale morphology and structure from the other side. To do so, effects of different precoating such as; pure Ni, Fe, Cr, hybrid Ni- Fe_2O_3 or NiFe alloy on the properties of resulted Al_2O_3 scales were studied.

This could be obtained via the strategies as follow:

- Investigation of the effects of metal seeding layers on Al_2O_3 formed on NiAl alloy such as long-term oxidation kinetics, oxidation products, morphology and structure of scales, direct formation of $\alpha\text{-Al}_2\text{O}_3$ or transformation of meta-stable alumina to $\alpha\text{-Al}_2\text{O}_3$.
- In order to produce a protective $\alpha\text{-Al}_2\text{O}_3$ with a slow growth rate, a hybrid-seeding layer of Ni- Fe_2O_3 composites will be deposited on NiAl prior to the oxidation.
- Effects of Ni-Fe co-deposits on direct $\alpha\text{-Al}_2\text{O}_3$ formation with changing Fe/Ni ratio.

2.6 References

1. H. Birks, G. H. Mayer, Introduction to the High Temperature Oxidation of Metals, Published by Edward Arnold LTD, Pittsburgh, 1983
2. P. Kofstad, High Temperature Corrosion, Elsevier Science Publishers LTD, England 1988
3. N. Cabrera, N. F. Mott, Theory of the oxidation of metals, Rep. Prog. Phys. 12 163 (1948)
4. N. F. Mott, The theory of the formation of protective oxide films on metals. III, Trans. Faraday Soc. 43 429 (1947)
5. C. Wagner, Beitrag zur Theorie des Anlaufvorgangs, Z. Phys. Chem. B 21(1933) 25
6. C. Wagner, Reaktionstypen bei der Oxydation von Legierungen, Z. Elektrochem. 63 772 (1959)
7. F. Maak, Zur Auswertung von Messungen der Schichtdicken binärer Legierungen mit innerer Oxydation bei Gleichzeitiger äußerer Oxydation, Z. Metall. 52 545 (1961)
8. R. A. Rapp, Kinetics, Microstructures and Mechanism of Internal Oxidation- Its Effect and Prevention in High Temperature Alloy Oxidation, Corrosion 21 382 (1965)
9. J. H. Swisher, Oxidation of Metals and Alloys, ed. D. L. Douglass, ASM, Metals Park, Ohio, Chapter 12, 1971,
10. J. L. Meijering, Internal oxidation in alloys, Advances in Materials Research, Volume 5, ed. H. Herman, Wiley New York, 1971
11. Neil Birks, Gerald H. Meier, and Frederick S Pettit, Introduction to the High Temperature Oxidation Materials, 2nd. Ed, 2004
12. Pettit FS (1967) Trans Metall Soc AIME 239:1296
13. K. Wefers and C. Misra, "Oxides and Hydroxides of Aluminum", Alcoa Laboratories, Aluminum Company of America, Pittsburgh, (1987) p. 47.
14. R.W.G. Wyckoff, Crystal Structures, 2nd ed., vol. 2, Interscience, New York, 1964, pp. 6-8
15. I. Levin and D. Brandon, J. Am. Ceram. Soc. 81, 1995 (1998)
16. R.-S. Zhou and R.L. Snyder, Acta. Cryst. B 47, 617 (1991)

17. N. R. Linblad, A review of the behavior of aluminide coated super alloys, *oxid. Met.* 1(1) 143-170 (1969)
18. G W. Goward, recent developments in high temperature coatings for gas turbine airfoils, *high temp. corros. NACE* 6, 553-560 (1983)
19. W.E. Boggs, The oxidation of iron-aluminum alloys from 450 to 950C, *J. Electrochem. Soc.* 118(6), 906-913 (1971)
20. R. Molins, A. Germidis, E. Andrieu, Oxidation of thin FeCrAl strips: kinetic and microstructural studies, *Microscopy of Oxidation-3*, Cambridge, UK, 16-18 Sept, (1996.) 3-11
21. M. Kohono, S. Ishikawa, K. Ishii, S. Satoh, Growth behavior and microstructure of Al₂O₃ layer formed on La and Zr-added Fe-20Cr-5Al alloys, Cambridge, UK, 16-18 Sept, *Microscopy of Oxidation-3*, (1996) 55-62
22. K.S. Lee, K.H. Oh, W.W. Park, H.Y. Ra, *Scr. Mat.* 39 (1998) 1151-1155
23. J.K. Tien, F.S. Pettit, Mechanism of oxide adherence on Fe-25Cr-4Al -Y or Sc. alloys, *Metall. Trans.* 3 (1972) 1578-1599
24. T. B. MASSALSKI, *Binary Alloy Phase Diagrams Vol. I.* American Society for Metals, Metals Park, Ohio (1986)
25. G. SAUTHOFF, *Z. Metallkde* 81, 855 (1990)
26. R. HUTCHINGS and M. H. LORETTO, *Metal. Sci.* 12, 503 (1978)
27. J. L. SMIALEK, *Metall. Trans. A.* 9A, 309 (1978)
28. G. C. WOOD F. H. STOTT, *Br. Corros J.* 6, 247 (1971)
29. G. C. Rybicki and J. L. Smialek, *Oxidation of Metals* 31, 275-304 (1989)
30. J. DOYCHAK, Ph.D. Thesis, Case Western Reserve Univ., Cleveland, OH (1986)
31. Lehnert G, Meinhardt H (1972) *Electrodepos Surf Treat* 1:71
32. Felten EJ (1976) *Oxid Met* 10:23
33. Chen JH, Little JA (1997) *Surf Coat Technol* 92:69, Hou PY, McCarty KF (2006) *Scr Mater* 54:937
34. Grabke HJ, Wiemer D, Viehhaus H (1991) *Appl Surf Sci* 47:243
35. Pint BA (1997) *Oxid Met* 48:303
36. Pint BA, Wright IG, Lee WY, Zhang Y, Prueßner K, Alexander KB (1998) *Mater Sci Eng A* 245:201
37. Wood GC, Stott FH (1983) *High Temp Corros NACE* 6 227

38. Stott FH (1997) Mater Sci Forum 251–254:19
39. Felten EJ, Pettit FS (1976) Oxid Met 10:189
40. Prescott R, Graham MJ (1992) Oxid Met 38:233
41. Lipkin DM, Clarke DR, Hollatz M, Bobeth M, Pompe W (1997) Corros Sci 39:231
42. Hou PY, Paulikas AP, Veal BW (2004) Mater Sci Forum 461– 464:671
43. Doychak J (1994) In: Westbrook JH, Fleischer RL (eds) Intermetallic compounds, Chapter 43, vol 1. Wiley, New York
44. H.J. Grabke, M.W. Brumm, B. Wagemann Mat Corr;47 675 (1996)
45. I. Rommerskirchen, B. Eltester, H. J. Grabke Mat Corr; 47 646 (1996)
46. H. J. Grabke, Intermetallics 7, 1153–1158 (1999)
47. B. A. Pint, A. J. Garratt-Reed and L. W. Hobbs, Journal of American Ceramic Society, 81, 305-14 (1998)
48. L. B. Pfeil, U.K. Patent no 459848, (1937)
49. L. B. Pfeil, U.K. Patent no 574088, (1945)
50. S. Hayashi and B. Gleeson, Oxidation of Metals, 71, 5-19 (2009)
51. M. W. Brumm and H. J. Grabke, Corrosion Science 33, 1677–1690 (1992)
52. Z. Liu and W. Gao, Oxid. Met. 54, 189 (2000)
53. H. El Kadiri, R. Molins, Y. Bienvenu and M. F. Horstemeyer, Oxid. Met. 64, 63 (2005)
54. F. Liu, H. Gotlind, J. E. Svensson, L. G. Johansson and M. Halvarsson, Corr. Sci. 50, 2272–2281 (2008)
55. H. Josefsson, F. Liu, J. E. Svensson, M. Halvarsson and L. G. Johansson, Mat. Corr. 56, 801 (2005)
56. Y. Kitajima, S. Hayashi, T. Nishimoto, T. Narita and S. Ukai, Oxid. Met. 73, 375 (2010)
57. Y. Kitajima, S. Hayashi, T. Nishimoto, T. Narita and S. Ukai, Oxid. Met. 75, 41 (2011)
58. S. Hayashi, I. Saeki, Y. Nishiyama, T. Doi, S. Kyo, and M. Segawa, Materials Science Forum Vol 696 (2011) pp 63-69
59. S. Hayashi, Y. Takada, I. Saeki, A. Yamauchi, Y. Nishiyama, T. Doi, S. Kyo and M. Sato, Materials and Corrosion 2012, 63, No. 10

Chapter 3

EXPERIMENTAL SET UP

3.1 Sample Preparation

3.1.1 Alloy Making

The alloy of Ni50Al with high purity was prepared by using argon arc melting system shown in **Fig. 3.1.1**. Fragments of pure Al and Ni were put on the Cu-template inside the chamber and then the chamber was filled with Ar gas. Applying the arc current of 500 A D.C., the plasma produced between the electrode and the fragments that makes the high temperature melts Al and Ni together. Final product was a 50 g ingot of Ni50at.%Al alloy.

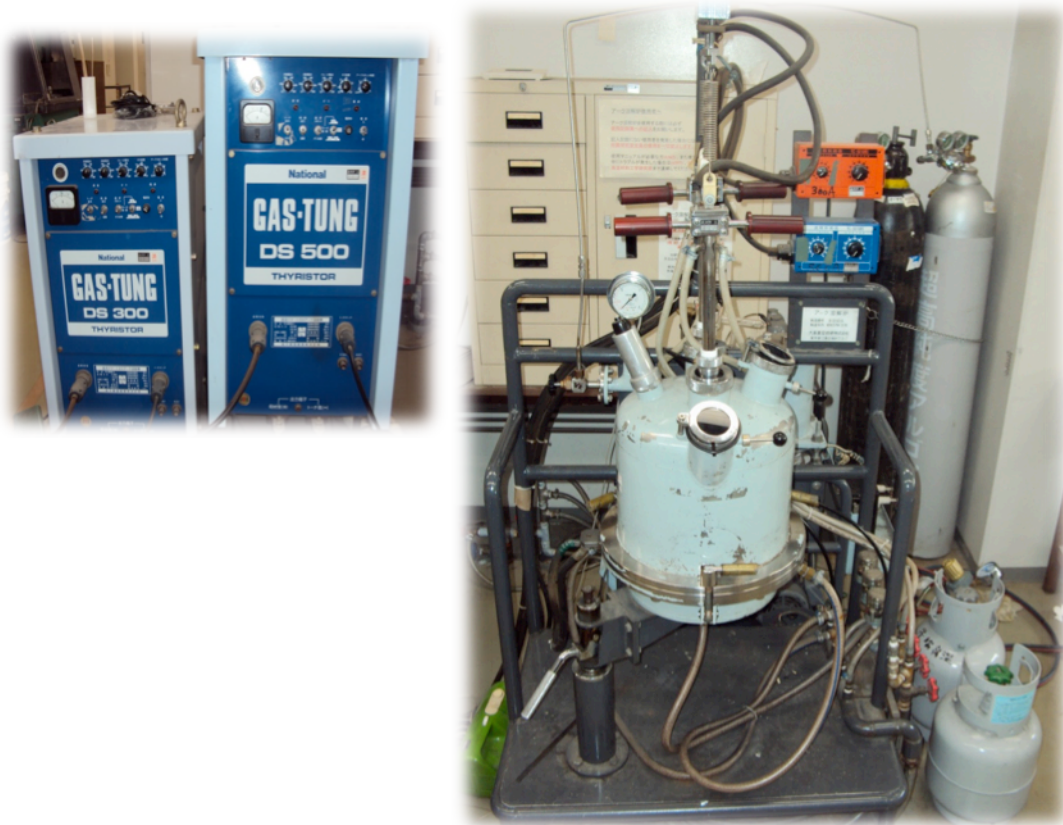


Figure 3.1.1: Argon arc melting system

3.1.2. Homogenization

The Ni50Al ingot was placed in a ceramic crucible and kept inside the hot zone of the tube furnace in order to homogenize the alloy ingot at 1200°C for 48h under vacuum (5×10^{-3} Pa) as shown in **Fig. 3.1.2**.



Figure 3.1.2: Vacuum tube furnace

After homogenization the alloy ingot was cut into slices of ~ 1 mm thickness. The surfaces of these samples grinded with SiC paper (grit 80, 200, 800, 1200 and 4000), cleaned in ethanol, and polished with $3\mu\text{m}$ diamond paste to obtain a mirror-like surface. Prior to metal deposition, it was ultrasonically degreased in acetone for 10min.

3.2. Pre-coating Methods

There are several techniques used for surface modifications of materials by applying coatings on metals and alloys.

- Physical Vapor Deposition (PVD) is the process involving vaporization of the coating material in vacuum, transportation of the vapor to the substrate and deposition of materials on the substrate surface.
- Chemical Vapor Deposition (CVD) is the process, in which the substrate was placed in an atmosphere of a mixture of gases and kept at high temperature, and thus chemical reaction or decomposition of the gases occurs on the substrate surface to form coatings.
- Thermal spraying is the deposition of the atomized at high temperature metal, delivered to the substrate surface in a high velocity gas stream.
- Hot dipping is a process of coating immersing the part into a molten metal, followed by removal of the substrate from the metal bath, which results in formation of the metal coating on the substrate surface.
- Electroplating is the process, in which metal electrodeposits on a cathode immersed in an electrolyte solution. In many case the anode is made of the depositing material, which is anodically dissolved in the solution to form metal ions which migrate through the electrolyte to cathode (sample) surface.
- Electroless deposition is the process in which metal deposits from electrolyte solution on the substrate due to cathodic reduction of metal ions by the reducing agents in the plating bath.
- Conversion coating is the process, in which non-metallic coatings are formed as a result of chemical reaction on the substrate surface.

3.2.1. Precoating by Physical Vapor Deposition

Metallic thin films are often grown by the vapor deposition, i.e., the film is formed on the substrate by deposition process with or without chemical reaction in a vapor phase. There are typical two methods; chemical vapor deposition (CVD) and physical vapor deposition (PVD). In CVD, the vapor that is consisted of volatile species which react to form the thin film on the surface of the substrate. In PVD, which is the method used in the present study, a piece of the source materials are heated to be evaporated in a form of atoms or molecules, transferred from the source metals to the substrate, and deposit on a substrate surface to form a thin film. PVD system is operated in a vacuum chamber to avoid the chemical reaction of vaporized elements with the other species. Usually a base pressure is used in the range from 10^{-4} Pa (high vacuum, HV) to 10^{-8} Pa (ultrahigh vacuum, UHV). In this work, HV system shown in **Fig. 3.2.1** was used because it provided sufficient performance to produce precoatings.

Precoating of pure Ni, Fe or Cr of 50 nm in thickness was deposited on the samples of Ni50Al alloy mirror finished. In order to avoid any handling errors, deposition parameters such as deposition time (10 s), amount of metal sources (10 mg) and the distance between the sources and substrate were kept constant.



Figure 3.2.1: Physical Vapor Deposition system

3.2.2. Precoating by Electrodeposition

Electrodeposition is a simple method for achieving high quality thin films at low temperatures and low production cost. In an electrodeposition process, ions are moved through a solution by an electric field to coat an electrode. The simplest form of an electrochemical cell is performed using a 2-electrode system, consisting of a cathode and an anode. In the 2-electrode system, the voltage is measured between these two electrodes, and the current is measured anywhere in the circuit. This system works very well under equilibrium conditions. However, if the electrochemical reactions taking place are not in equilibrium, the simple voltage measurement will be inaccurate due to red-ox potentials and overpotential. To counter this problem a third electrode is introduced with the sole task of measuring the voltage on the working electrode versus a known, stable reference potential. This electrode is called a reference electrode. Different reference

electrodes have different reduction potentials with a normalized hydrogen electrode (NHE) being defined as zero. The voltage is applied between the cathode and the anode. The cathode is the negative electrode and the anode is the positive electrode. In cathodic deposition the substrate is the cathode and the counter electrode is the anode, and opposite for anodic deposition.

Working electrode

The working electrode is where the desired reaction should take place, and in the case of electrodeposition this electrode is also often the substrate. In electrochemistry the working electrode should have small area. It also should not chemically react with the test solution, and the surface should be smooth.

Counter electrode

The counter electrode supplies current to the reaction on the working electrode. In order to reduce the overpotential as much as possible, the electrode process should be oxidation or reduction of an electrolyte component to oxidation or reduction products. If possible it could be the opposite reaction of the working electrode, thus keeping the electrolyte composition constant.

Reference electrode

A good reference electrode should be at a constant potential independent of current density, which it will be if the reaction is reversible. Often used reference electrodes are NHE, SCE (saturated calomel electrode) and Ag/AgCl compared to using NHE and SCE the AgCl electrode has the advantage of being both environmentally friendly and easy to make. The different reference electrodes have different potentials, the NHE is defined as zero, and SCE and Ag/AgCl have potentials around 0.2V/NHE. The counter electrode

may also act as reference electrode, though this setup gives less control over the applied potential due to overpotential. The counter electrode may work as reference for small currents.

Unlike physical vapor deposition (PVD) and many other techniques, electrodeposition is a conventional technique because of its low cost, low energy requirement, capability to handle complex geometry, simple scale-up with easily maintain equipment, good chemical stability, easily maintained equipment and after all very important potential of it is a very large number of pure metals, alloys, composites, ceramics, which can be electrodeposited with grain size less than 100nm [3]. Metals, alloys and polymers can be deposited in this process. Ni, Cu, Cr, Co, Au, Zn etc. are preferred metals in this field [4-7] and Co-Cu, Ni-Co etc. multilayer deposition done in this process [8, 9]. Polystyrene, perplex, PTFE, rubbers are the polymer materials apply for coating used in industrial application [10-13]. The coating materials cover the large applications as coatings of engine cylinders, high pressure valves, musical instruments, car accessories, small aircraft microelectronics, aerospace, medical devices, marine, agriculture and nuclear fields.

Nickel deposition is very popular for electrodeposition because nickel coating shows the properties of good mechanical properties, excellent corrosion resistance, high electrical conductivity, good thermal conductivity and good magnetic property [14, 15]. Deposition of ceramic particles on metal substrate can be used to improve the mechanical properties of substrate such as hardness, wear resistance, protection against high temperature, corrosion and oxidation [16-21].

In this study, effects of two electrodeposited precoating systems on the oxidation properties of Ni50Al alloy have been investigated.

1. Thin Ni or Ni-Fe₂O₃ composite was electrodeposited on Ni50Al sample from 200ml Watts bath containing 250 g dm⁻³ NiSO₄•6H₂O, 45 g dm⁻³ NiCl₂•6H₂O, 30 g dm⁻³ H₃BO₃ and 0 or 20 g dm⁻³ Fe₂O₃ powder of 40 nm in average diameter at pH 4 by using a potentiostat (Ivium Technologies Co., model Iviumstat) as shown in **Fig. 2.3a** and an electrochemical cell composed of Ag/AgCl reference electrode, Ni sheet counter electrode (about 4 cm² in area) and Ni50Al (about 2 cm² in area) sample working electrode **Fig. 2.3b**. PED was conducted using various conditions under solution stirring at 600 rpm.

2. Ni or Ni-Fe precoating layer was electrodeposited on the Ni50Al sample from a 200ml Ni-bath containing 15.5 g dm⁻³ NiSO₄•6H₂O as a source of Ni, (0, 1.4 or 27.8) g dm⁻³ FeSO₄•7H₂O as a source of Fe, (50 or 35) g dm⁻³ Na₂SO₄ and 12.5 g dm⁻³ H₃BO₃ as a buffer. Fe coating was electrodeposited on the Ni50Al sample from a Fe-bath containing 27.8 g dm⁻³ FeSO₄•7H₂O as a source of Fe, 35 g dm⁻³ Na₂SO₄ and 12.5 g dm⁻³ H₃BO₃ as a buffer. The solution acidity was adjusted by 0.1 M H₂SO₄ at pH 3. The electrodeposition process was conducted at deposition current of -10 mA.cm⁻² for 600 sec with solution agitation at 400 rpm by using a potentiostat (Ivium Technologies Co., model Iviumstat) and an electrochemical cell composed of Ag/AgCl reference electrode, Ni sheet counter electrode (about 4 cm² in area) and Ni50Al (about 2 cm² in area) sample working electrode. After electrodeposition, these samples were subjected to high-temperature oxidation tests. Samples were placed in a furnace exposed to air, and the temperature was elevated at a rate of 10 °C min⁻¹ to 1000 °C and kept for $t_{ox} = 0.5, 1, 4, 7$ and 9 h and then cooled down to room temperature. Weight of samples were measured before and after the oxidation tests to obtain oxidation mass gain.

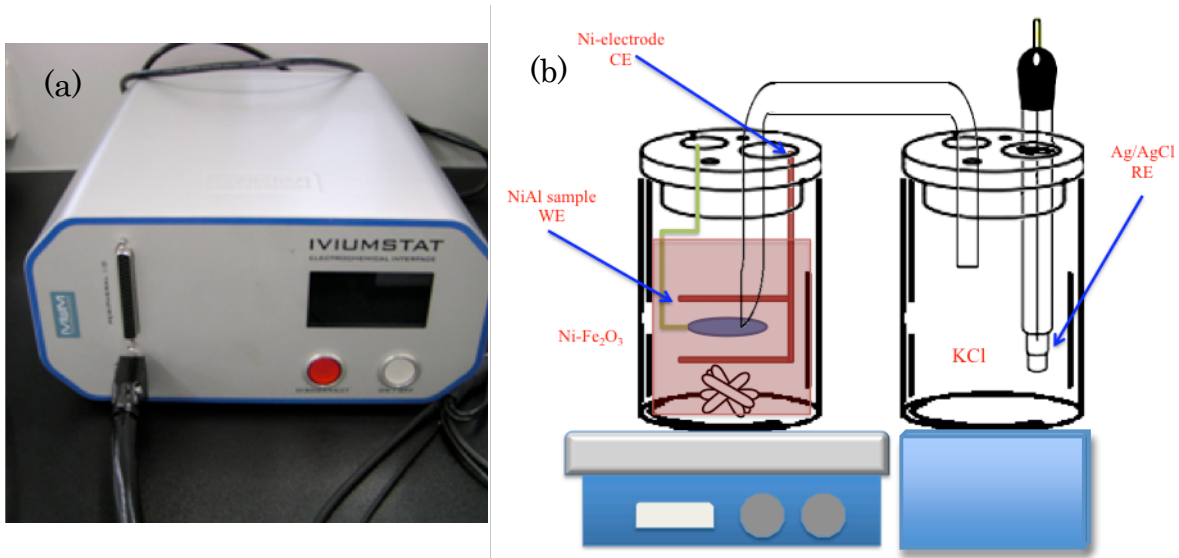


Figure 3.3: Potentiostat (Ivium Technologies Co., model Iviumstat) (a) and an electrochemical deposition three-electrode cell (b)

3.3. Oxidation Tests

After preparation, these samples were subjected to high-temperature oxidation test. Samples were placed in a furnace exposed to air (**Fig. 3.4.1a**), and the temperature was elevated with $10\text{ }^{\circ}\text{C min}^{-1}$ to $1000\text{ }^{\circ}\text{C}$ and kept for $t_{\text{ox}} = 1, 9, 25$ or 100 h and then cooled down to the room temperature (**Fig. 3.4.1b**). The weights of samples were measured before and after the oxidation test to obtain the oxidation mass gain.

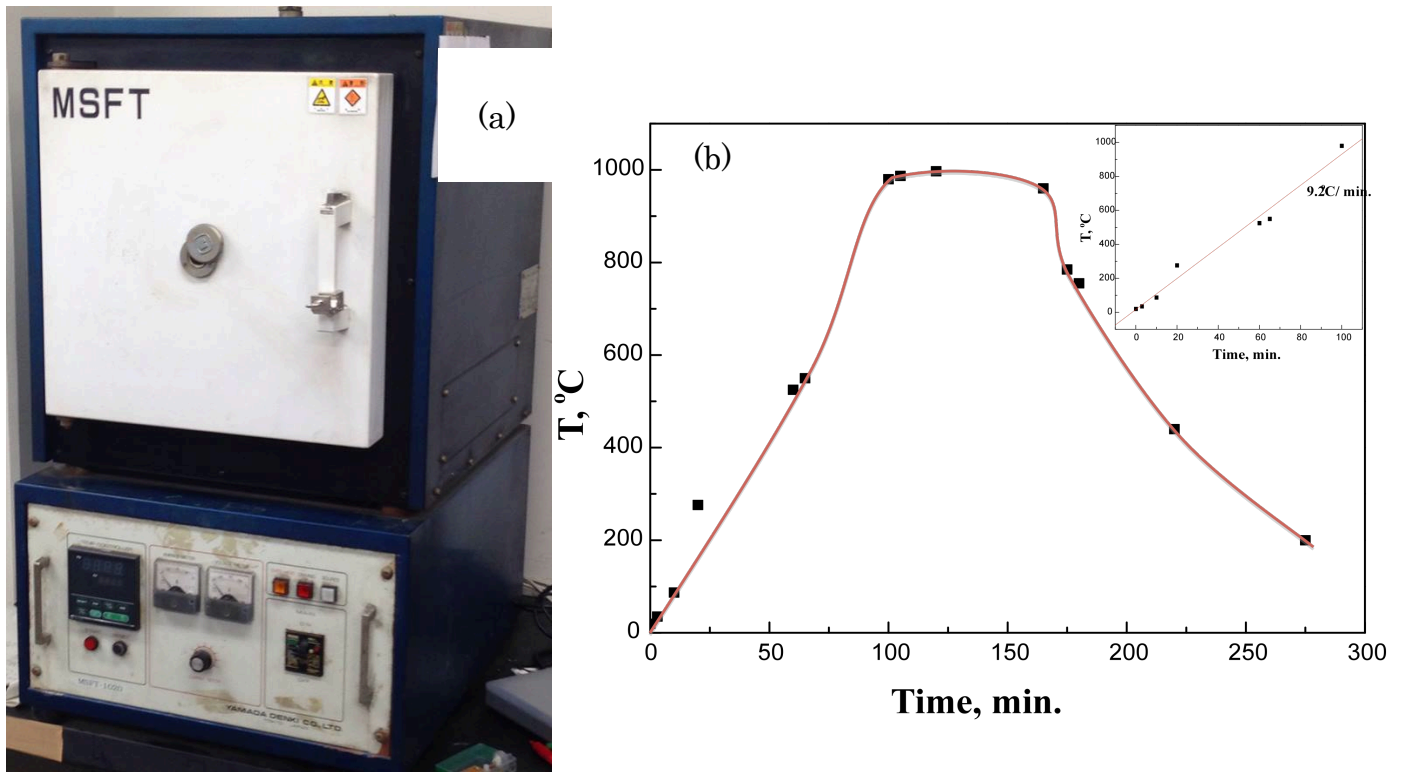


Figure 3.4.1: (a) Super furnace, (b) furnace's temperature calibration for 1 cycle of $10^{\circ}\text{C}\cdot\text{min}^{-1}$, heating rate and 1 h holding time at 1000°C

3.4. Surface and Cross-sectional Observations

3.4.1 Field Emission Scanning Electron Microscopy (FE-SEM)

Scanning Electron Microscopy (SEM) is a high-resolution surface imaging technique, which is based on focusing a beam of electrons onto the surface of a sample and scanning of the beam across it in a “raster” or pattern of parallel lines. When an electron is incident on the surface, a number of phenomena occurs but most important for the microscope are the emission of secondary electrons with energies of a few tens of eV and re-emission or reflection of the high energy backscattered electrons from the primary beam. The signals that provide the greatest amount of information in SEM are the

secondary electrons, backscattered electrons and X-rays. The intensity of the secondary electrons is very sensitive to the angle at which the incident electron beam strikes the surface, i.e. to topographical features on the sample. Also, the emitted X-rays have an energy characteristic of the parent element, detection and measurement of its energy permits elemental analysis of the selected area of the SEM image by means of Energy Dispersive X-Ray (EDX) spectroscopy. The JEOL JSM-6500F is a low voltage field emission gun SEM that operates at accelerating voltage 0.5~30kV, magnification $\times 10 \sim 500,000$, image resolution 1.5nm (15kV) , 5.0nm (1kV) and beam current 1pA~200nA. **Fig. 3.4.2** shows the FESEM system that was used in this study.



Figure 3.4.2: JEOL JSM-6500F Field Emission Scanning Electron Microscopy (FE-SEM)

3.4.2 Multi-beam System (Focused Ion Beam milling and FE-SEM imaging) (FIB)

Focused ion beam device is a powerful device for TEM sample preparation and microscopic observations. Soft, hard, and composite samples can be prepared with minimum sample damage or deformation. An Ga^+ ion beam mills cross sections in almost any material that is affixed to the continuously oscillating sample holder, creating a clean, polished cross section with a large viewing area. With the FIB, a mirrored cross-sectional surface of almost any material could be prepared in one step. This includes difficult-to-polish soft materials such as copper, aluminum, gold, solder, and polymers, as well as difficult-to-cut materials such as ceramic and glass. The electron microscope in FIB allows the user to select the position of the interest within a few microns of the precise.

JIB-4600F/HKD focused ion beam milling and FE-SEM imaging device, a high performance SEM and micro milling, combines a Schottky field emission electron column with real time milling and monitoring capability. This device is a multifunctional device where the milling process is simultaneously viewed and analyzed in SEM imaging, effective for inner structure analysis and TEM thin film sample preparation. Multi port specimen chamber for a complete operation from FIB milling to SEM imaging to 2D and 3D analysis by a variety of detectors including EDS and EBSD. The milling conditions are as follows; ion source Ga liquid metal ion source, accelerating voltage 1~30kV, magnification $\times 30$ (view area search), $\times 100 \sim 300,000$, image resolution 5nm (30kV), maximum beam current 60nA (30kV). **Fig. 3.4.3** shows the FIB system that was used in this study.

Micro Pickup System Micro Support Co., Ltd. (Axis Pro) is a micro-manipulating system, which enables collection of a fine subject and precision

processing of target area on samples through precise motion control, and mainly applied to lift out the TEM sample produced by FIB. For preparation of a sample for cross-sectional observation, a carbon layer was pre-deposited to protect the surface from Ga^+ milling, and then a cross-section was lifted out and attached to a Mo support grid by using. This grid fits into a specimen holder of TEM observation. **Fig. 3.4.4** shows the micro pickup system that was used in this study.



Figure 3.4.3: JIB-4600F/HKD focused ion beam milling and FE-SEM imaging device
(Multi-beam FIB)

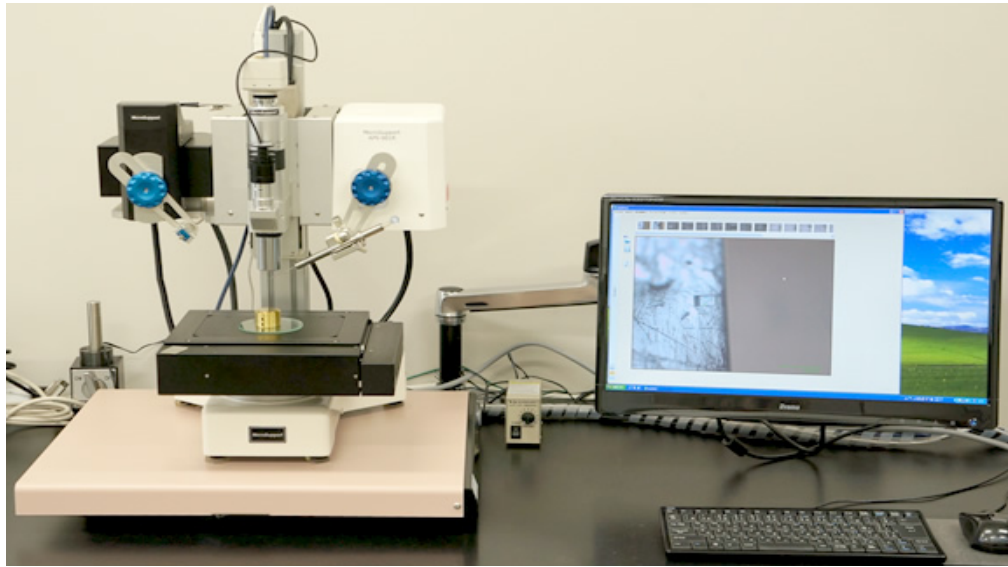


Figure 3.4.4: Micro Pickup System Micro Support Co., Ltd. (Axis Pro)

3.4.3 Transmission electron microscopy (TEM)

A multipurpose (imaging, SA diffraction, HD diffraction, CBED, NBD, EDS), 200 kV transmission electron microscope with the point resolution as high as 0.19 nm. In TEM measurements, microstructure observation using a bright field (BF), crystallographic analysis using selected area electron diffraction (SAED) with a double-tilt holder and EDX analysis were also carried out. **Fig. 3.4.5** shows the TEM system that was used in this study.



Figure. 3.4.5: Transmission Electron Microscope (Model : JEM-2010)

3.5. Oxidation products phases' identification

X-ray Diffraction Spectroscopy (XRD)

The method of X-ray diffraction (XRD) is probably the most widely used in the science of crystalline thin films. The simplest, and maybe most important, application of the technique is to determine the crystal structure of a sample. This can be done both for new materials, with the aid of simulations, and for previously known phases by comparison with reported data a beam of X-rays of a specific wavelength (often Cu $K\alpha$: 1.54\AA) is incident onto a sample and the resulting diffracted beams are detected. If the sample is crystalline, the detected intensity of diffracted beams will vary in different directions, depending on the interplanar lattice spacing, according to Bragg's law. By scanning incident (θ) and/or detecting (2θ) angles (with respect to the sample surface) a

unique diffraction pattern is produced, characteristic of the crystal structure of the sample. Since a relatively large volume of the sample is typically probed by XRD, it is a macroscopic method, in contrast to, e.g., the electron diffraction analysis in transmission electron microscopy (TEM).

Phase analysis of oxidized samples was carried out using a JEOL JDX 3500 X-ray diffractometer operating at 300mA and 30kV with CuK α radiation from $2\theta = 10$ to 90° (step size 0.02°) at 0.5s/step. **Fig. 3.4.6** shows the XRD system that was used in this study.



Figure. 3.4.6: JEOL jdx-3500 X-ray diffractometer

Chapter 4

EFFECTS OF NANO METALLIC PRECOATINGS ON GROWTH of Al_2O_3 SCALE FORMED ON NiAl ALLOY

In a previous study by Kitajima et al., it was found that the Cr or Fe precoating suppress formation of $\theta\text{-Al}_2\text{O}_3$ at 900 °C by oxidation in air, but Ni was found to delay the transformation. The rapid formation of $\alpha\text{-Al}_2\text{O}_3$ is attributed to the formation of coated metal oxides, Cr_2O_3 and Fe_2O_3 , which have an isomorphous corundum structure with $\alpha\text{-Al}_2\text{O}_3$. These metal oxides may provide a higher density of sites for $\alpha\text{-Al}_2\text{O}_3$ nucleation. However, the effect of the transformation on the long-term growth rate of Al_2O_3 scales, which formed without meta-stable Al_2O_3 by Fe or Cr precoating, has not been examined.

The aim of this chapter is “The evaluation of the long-term oxidation kinetics, oxidation products, surface morphology and oxide scale structure of direct-formed $\alpha\text{-Al}_2\text{O}_3$ and the transformed $\alpha\text{-Al}_2\text{O}_3$ on NiAl alloy”

NiAl bare alloy, Ni-, Cr- and Fe-coated samples were then pre-oxidized at 900°C for 4h in order to form $\alpha\text{-Al}_2\text{O}_3$ scale from the beginning according to the previous study by Kitajima *et al.* After that the pre-oxidized samples were used as starting alloys for this study.

Abstract

The effects of pure metal precoatings, including Ni, Fe and Cr, on long-term oxidation kinetics, surface morphology and structure were studied. Ni-50Al alloy and Ni-coated, Fe-coated and Cr-coated samples were pre-oxidized at 900 °C in air. Then they were oxidized isothermally at 1000 °C in air. The bare Ni-50Al alloy oxidized rapidly during the initial stage of oxidation due to the formation of θ -Al₂O₃, but the oxidation rate decreased after α -Al₂O₃ had developed. Oxidation of the Ni-coated sample was slow from the beginning of oxidation even though the θ -Al₂O₃ was predominated for a longer oxidation time. No θ -Al₂O₃ was developed on Cr and Fe-coated samples, but the oxidation rates of these samples were much faster than those of bare and Ni-coated samples. Cross-sectional images revealed that the grain size of α -Al₂O₃, which formed on Cr and Fe-coated samples, was smaller than those of bare and Ni-coated samples. These metal precoatings affected the microstructure of α -Al₂O₃ and they showed a strong effect on the growth rate of α -Al₂O₃ in the steady-state oxidation stage.

Keywords:

NiAl alloy; α -Al₂O₃; Oxidation; Oxide Scale; Growth kinetics

4.1. Introduction

The oxidation resistance of Al₂O₃-forming Ni- and Fe-based alloys depends on the formation of slowly growing protective Al₂O₃ scales. Several types of Al₂O₃ scales have been found to form on alumina-forming alloys, such as meta-stable γ -Al₂O₃, δ -Al₂O₃, and θ -Al₂O₃ and stable α -Al₂O₃ scales. α -Al₂O₃ is a good protective oxide scale because of its thermodynamic stability and slow growth rate [1, 2]. However, at lower temperatures and/or in the early stages of oxidation of Al₂O₃-forming alloys, the meta-stable oxides γ -Al₂O₃, δ -Al₂O₃ and θ -Al₂O₃ usually grow and transform into stable α -Al₂O₃. The growth rate of these meta-stable oxide scales is about two orders of magnitude higher than that of α -Al₂O₃ [2-4] because meta-stable Al₂O₃ contains a higher concentration of cation vacancies. Therefore, rapid formation of α -Al₂O₃ is required to improve the reliability and lifetime of Al₂O₃-forming alloys and coatings. Addition of certain amounts of various metals is known to affect the Al₂O₃ scale properties. Doping the alloy with less than 0.1% of reactive elements (REs) was reported [5, 6]. REs such as Y, Zr, La, and Hf are often used in high temperature alloys in order to improve their oxidation resistance, by improving scale adhesion and slowing the rate of oxide-scale growth during exposure to higher temperatures. However, doping of REs often causes delay in the meta-stable to α -Al₂O₃ phase transformation, and this delay results in a greater growth rate of Al₂O₃ scales, particularly during the initial stage of oxidation [7]. Addition of Cr or Fe is known to accelerate the transformation to α -Al₂O₃. This beneficial effect on the phase transformation is thought to be due to the isomorphism of the metal oxides and α -Al₂O₃, which are formed at the initial stage of oxidation [8].

In our previous study, it was found that meta-stable Al₂O₃ formation at 900 °C by oxidation in air was completely suppressed by a very thin (thickness of about 50 nm)

precoating of Fe or Cr, which was deposited directly on the Fe-50Al alloy [9], but Ni was found to delay the transformation. However, the effect of the transformation on the long-term growth rate of Al_2O_3 scales, which formed without meta-stable Al_2O_3 by Fe or Cr precoating, has not been examined. The aim of this study was to evaluate the effects of introduction of these metal precoatings and different transformation behaviors of $\alpha\text{-Al}_2\text{O}_3$ on long-term growth kinetics of oxide scales at 1000 °C on Ni50Al alloy in air.

4.2. Experimental details

An approximately 50 g ingot of Ni50Al alloy was prepared from pure (99.99%) constituent metals under Ar atmosphere by using the Ar-Arc melting method. The alloy ingot was homogenized at 1200 °C for 48 h under vacuum (5×10^{-3} Pa). After homogenization, the alloy ingot was cut into slices of ~ 1 mm in thickness. The surfaces of these samples were ground with SiC paper (grit 80, 200, 800, 1200 and 4000) and cleaned in ethanol, followed by polishing with 3 μm diamond paste. Finally and prior to metal deposition, the sample was ultrasonically degreased in acetone for 10 min. Equi-thickness layers of ~ 50 nm of pure metallic precoating of Ni, Fe or Cr were deposited by physical vapor deposition (PVD) onto samples of the Ni-50Al alloy. In order to avoid any errors during the PVD process, deposition parameters including deposition time (10 sec), distance and metal source in the tungsten basket (10 mg) were kept constant. Ni-50Al samples with/without Ni, Fe or Cr precoating were firstly heated at a rate of 10 °C/min up to 900 °C in air and kept for 4 h and then furnace-cooled in order to pre-form meta-stable or stable alumina scales. The pre-oxidized samples were then heated again at a rate of 10 °C/min up to 1000 °C in air and kept for different time intervals in order to evaluate the effects of metal precoatings on $\alpha\text{-Al}_2\text{O}_3$ scale growth

rate at 1000 °C. After oxidation the samples were furnace-cooled in air. A JEOL 6500F field emission scanning electron microscope (FE-SEM) was used for observation of the surfaces of the oxidized samples after each oxidation step. JEOL JDX 3500 X-ray diffractometer operating at 20 mA and 40 kV with CuK_α radiation was used to characterize the structure of the oxidation products formed on oxidized samples. **Fig. 4.1** shows the schematic illustration of the experimental sequence in this study.

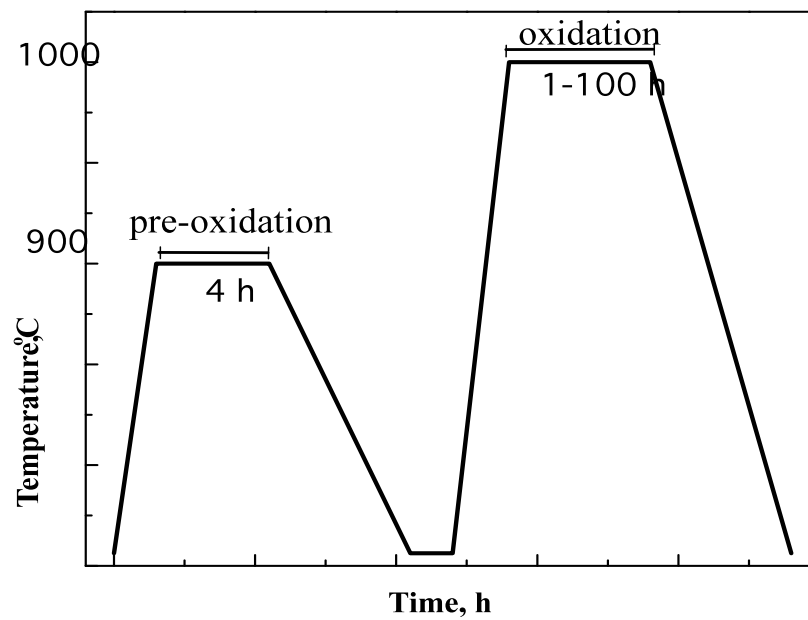


Figure 4.1: Schematic illustration of the oxidation cycles

4.3. Results and Discussion

4.3.1 Oxidation kinetics and products in the pre-oxidation stage

Fig. 4.2 shows the oxidation mass gain of Ni-50Al with/without Ni, Cr or Fe-coating for 4 h in air at 900 °C (pre-oxidation stage). The oxidation mass gain of the bare alloy and Ni-coated sample were greater than those of Cr-coated and Fe-coated samples. **Fig. 4.3** shows the surface morphologies and corresponding XRD patterns of the samples pre-oxidized at 900 °C for 4 h. An oxide scale of blade-like morphology covered the surface of the pre-oxidized bare alloy. This oxide scale was identified by XRD analysis to be a mixture of predominant θ -Al₂O₃ phase and α -Al₂O₃ phase as shown in **Fig. 4.3.1**. The Ni-coated sample was covered by an oxide scale of faceted morphology. This oxide scale was found to be mostly composed of NiO and α -Al₂O₃ phases. In addition to existence of NiO and α -Al₂O₃, weak signals were detected likely from NiAl₂O₄ and θ -Al₂O₃ oxide phases as shown in **Fig. 4.3.2**. On the other hand, a fine nodular oxide scale developed on the Cr-coated sample as shown in **Fig. 4.3.3**. This oxide was identified to be α -Al₂O₃. A tetrahedral-shaped oxide developed on the Fe-coated sample and was identified to be mainly α -Al₂O₃ coupled with weak signals from Fe₂O₃ as shown in **Fig. 4.3.4**. XRD phase identification (**Fig. 4.3.3** and **Fig. 4.3.4**) confirmed direct formation of α -Al₂O₃ at a relatively low temperature (900 °C) on the surfaces of Cr and Fe-coated samples. On the other hand, XRD analysis showed that θ -Al₂O₃ was still predominant on the bare alloy and Ni-coated sample after pre-oxidation at 900 °C for 4 h (**Fig. 4.3.1** and **Fig. 4.3.2**).

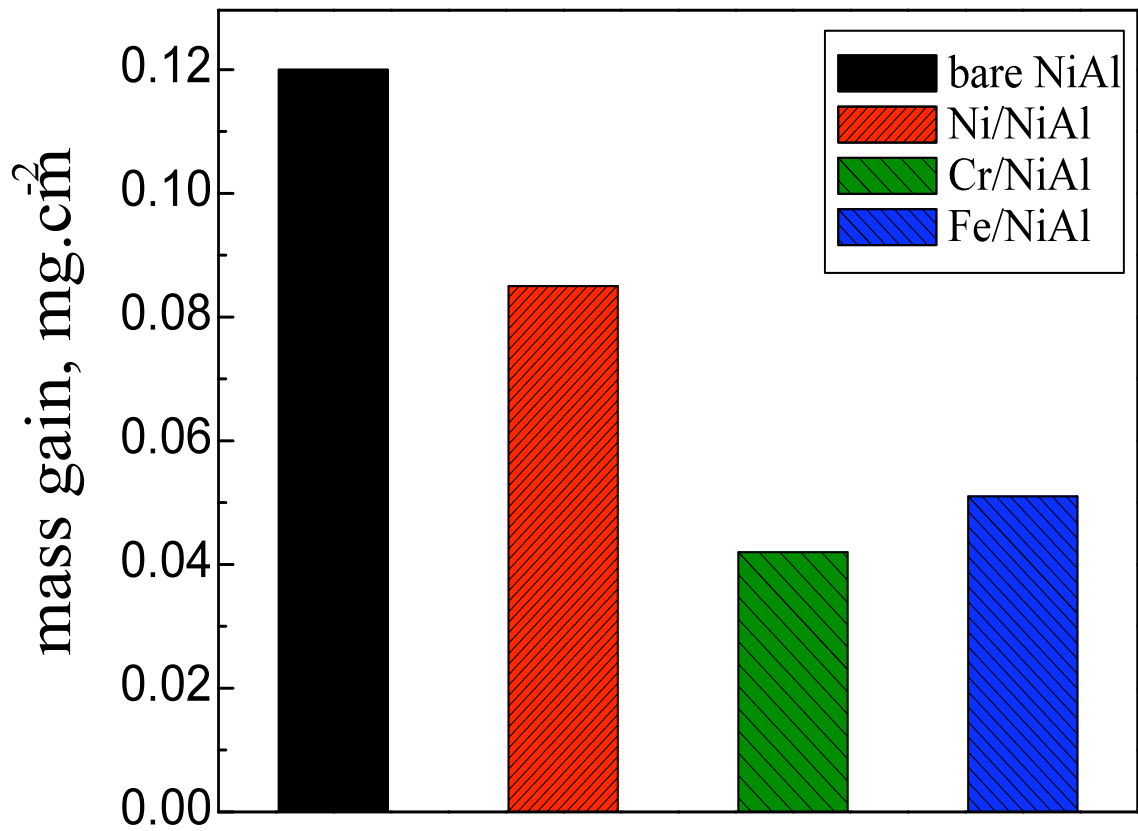


Figure 4.2: Oxidation mass gain of Ni-50Al with/without Ni, Cr or Fe pre-coating after pre-oxidation for 4 h at 900 °C in air

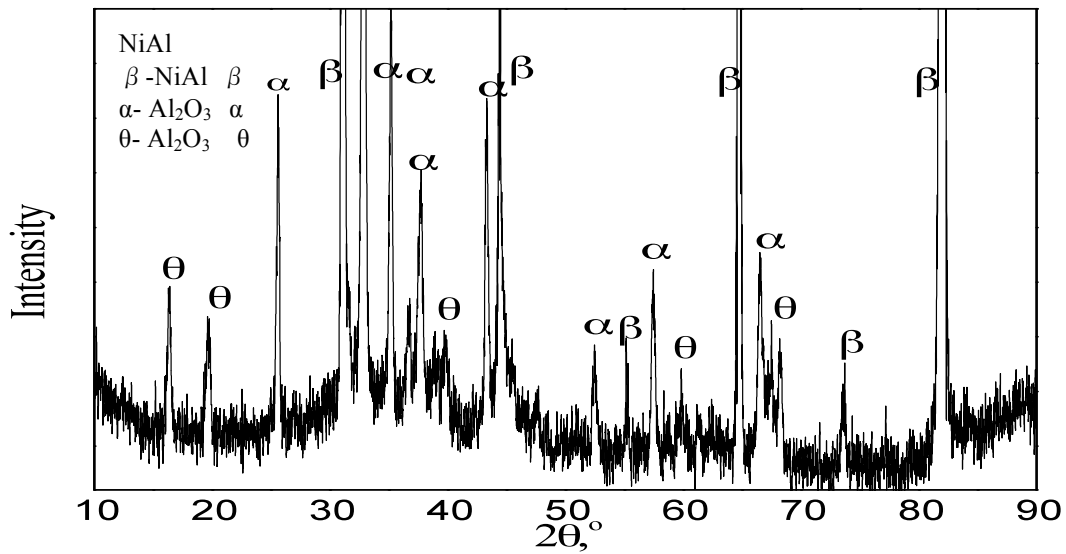
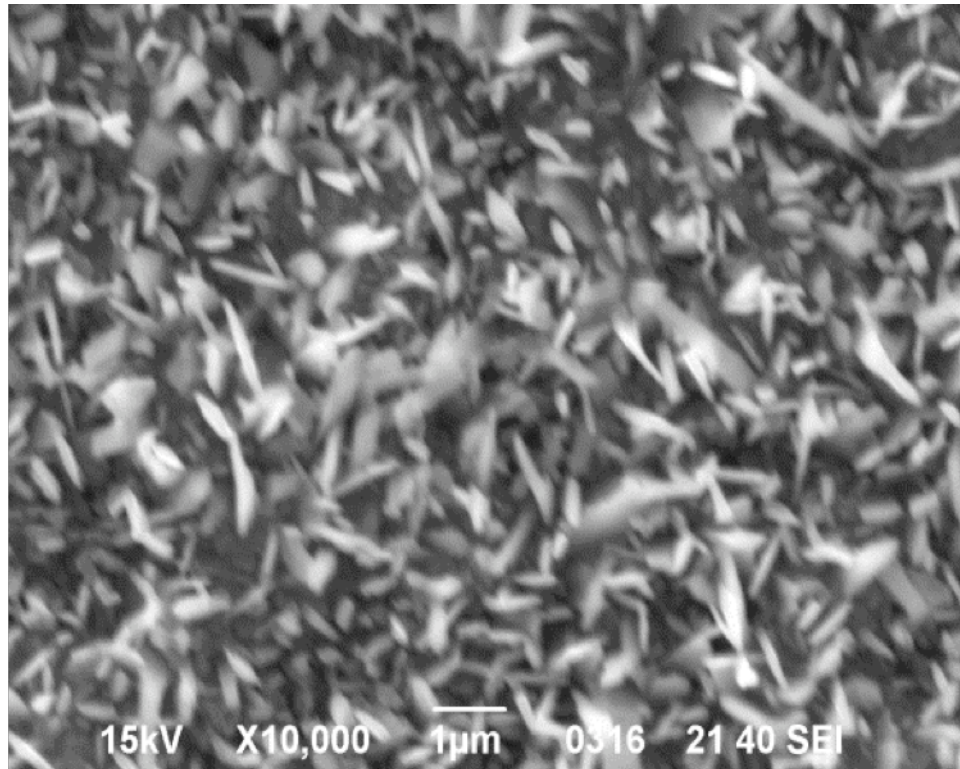


Figure 4.3.1: Surface morphology and corresponding XRD pattern of NiAl sample pre-oxidized for 4 h at 900 °C

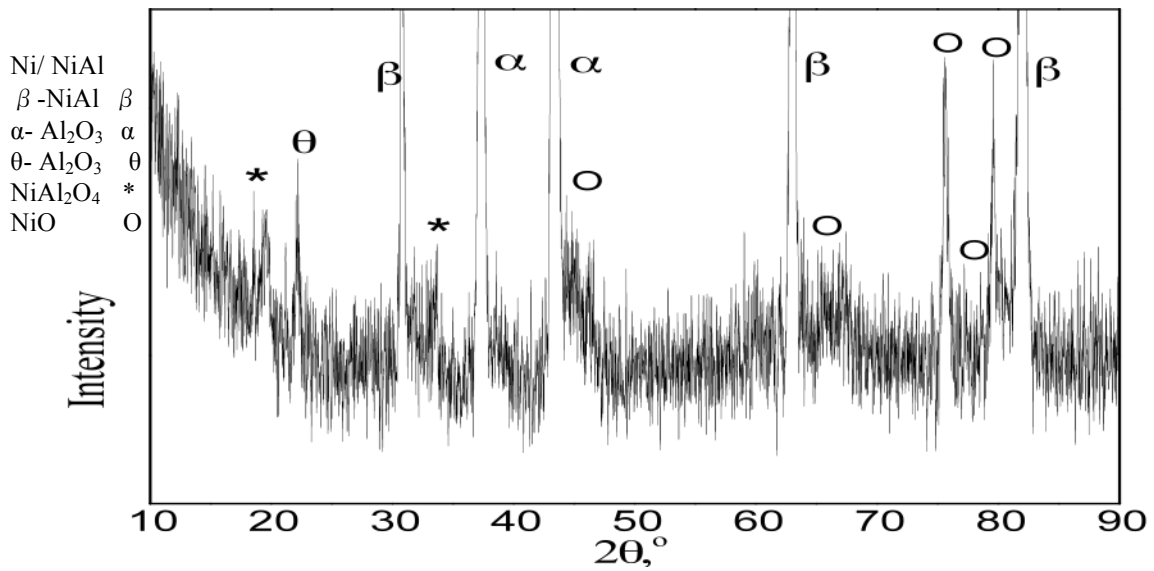
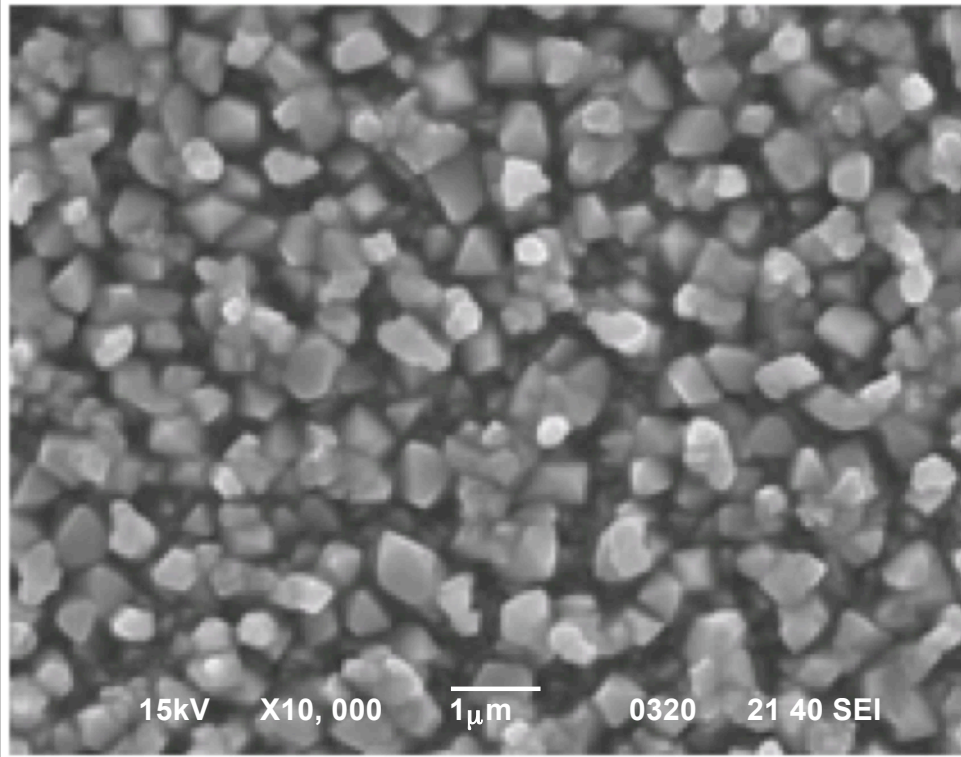


Figure 4.3.2: Surface morphology and corresponding XRD pattern of Ni-coated NiAl sample pre-oxidized for 4 h at 900 °C

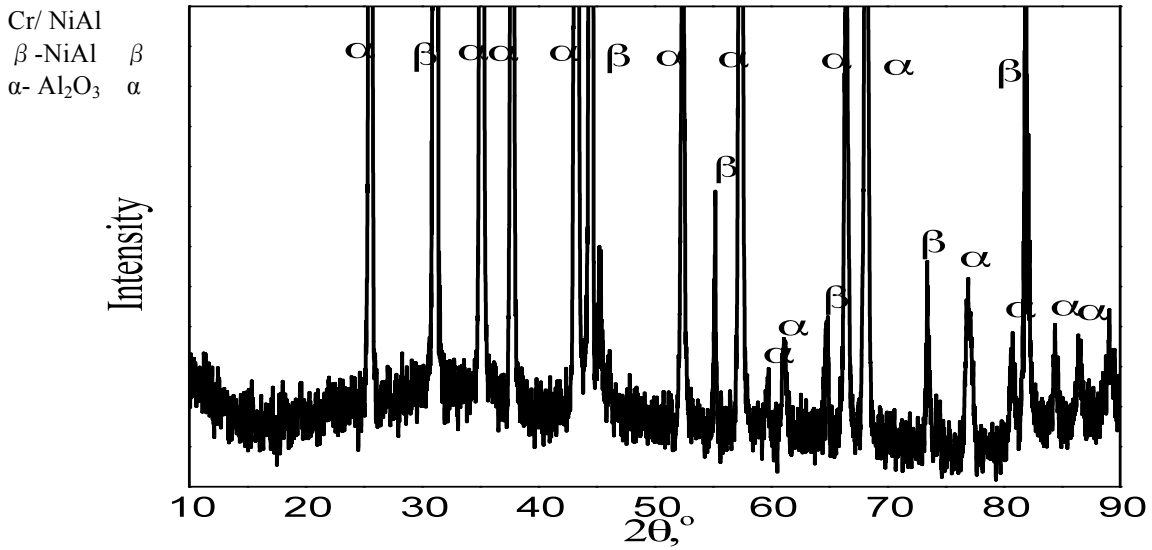
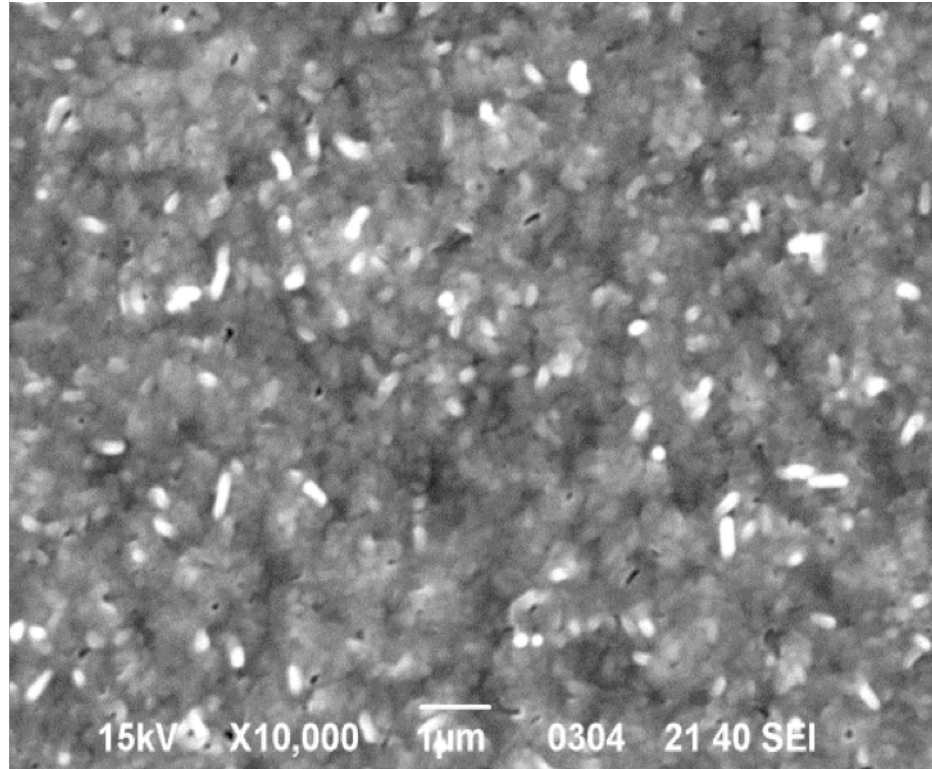


Figure 4.3.3: Surface morphology and corresponding XRD pattern of Cr-coated NiAl sample pre-oxidized for 4 h at 900 °C.

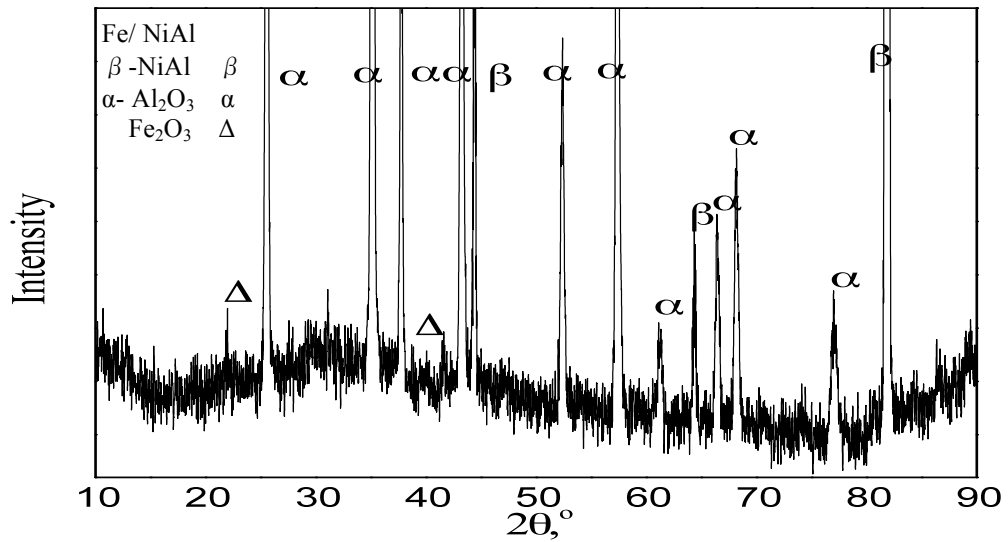
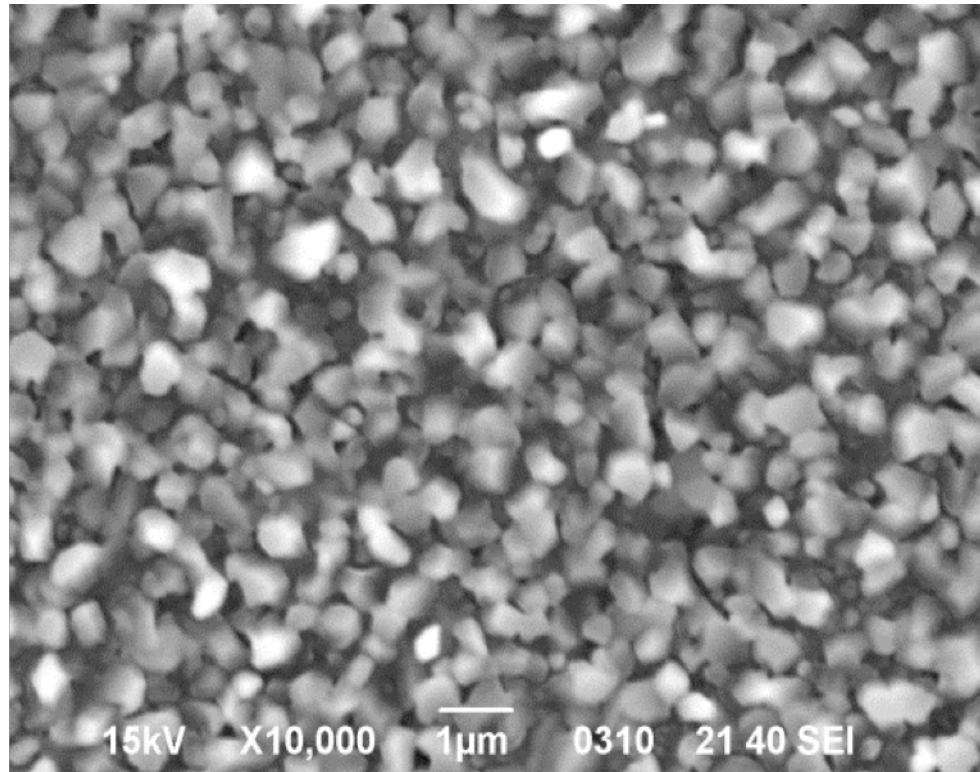


Figure 4.3.4: Surface morphology and corresponding XRD pattern of Fe-coated NiAl sample pre-oxidized for 4 h at 900 °C.

4.3.2. Oxidation kinetics and products of pre-oxidized samples at 1000 °C

The oxide scales that formed on pre-oxidized samples were confirmed to be predominantly θ -Al₂O₃ on the bare alloy, NiO and θ -Al₂O₃ on the Ni-coated sample, and α -Al₂O₃ on both the Cr and Fe-coated samples. The samples with those oxide scales were then oxidized isothermally at 1000 °C for different time intervals up to 100 h in air. **Fig. 4.4a** shows the oxidation kinetics of Ni-50Al with/without Ni, Cr or Fe precoating for up to 100 h at 1000 °C. Parabolic rate constants of the oxide scale growth were obtained from the parabolic plot shown in **Fig. 4.4b**. The oxidation behavior of the oxidized samples could be categorized into three different groups, bare NiAl alloy sample, Ni-coated sample, and Cr and Fe-coated samples.

During the main oxidation stage at 1000 °C, the oxidation mass gain of the pre-oxidized bare alloy was greater than those on the coated samples, but the k_p value of the bare alloy rapidly decreased to $1.1 \times 10^{-6} \text{ mg}^2 \cdot \text{cm}^{-4} \cdot \text{s}^{-1}$. This decrease in the k_p value is due to $\theta \rightarrow \alpha$ -Al₂O₃ phase transformation. The Ni-coated sample had the lowest oxidation mass gain from the beginning of oxidation and its k_p value was $0.2 \times 10^{-6} \text{ mg}^2 \cdot \text{cm}^{-4} \cdot \text{s}^{-1}$. The k_p values of the samples with Cr or Fe precoating, on which an α -Al₂O₃ scale had already developed before the main oxidation stage at 1000 °C, were both $1.4 \times 10^{-6} \text{ mg}^2 \cdot \text{cm}^{-4} \cdot \text{s}^{-1}$ and were greater than those of the bare alloy and Ni-coated sample.

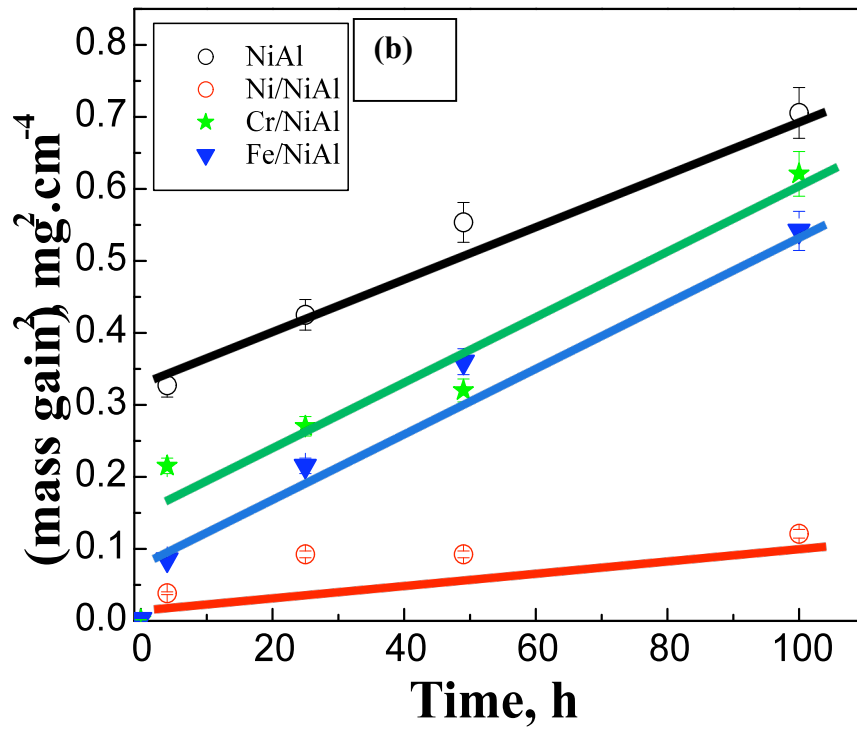
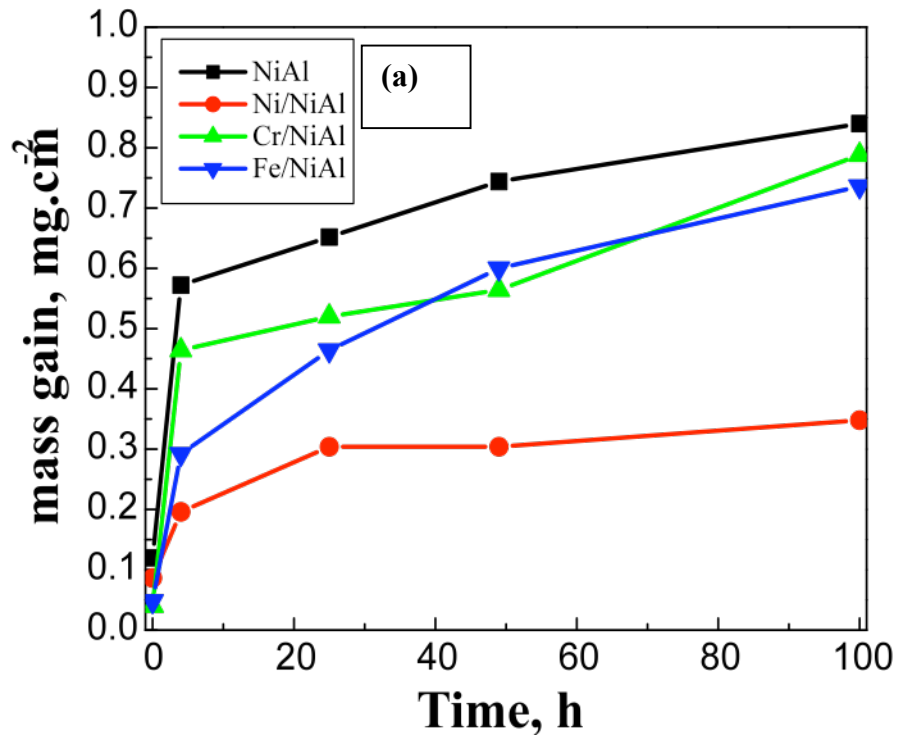


Figure 4.4: Oxidation mass gain of NiAl with/without Ni, Cr or Fe precoating for different time intervals at 1000°C in air (a) and rate constant, k_p , calculations (b)

4.3.2.1 Oxide scale evaluation at the early stage of oxidation

Fig. 4.5 shows the surface morphologies and corresponding XRD patterns of samples that were oxidized at 1000 °C after 4 h of oxidation. An oxide scale of feather-like morphology was observed on the surface of the bare alloy, and the XRD patterns indicated that θ -Al₂O₃ remained on the surface of the bare alloy as shown in **Fig. 4.5.1**. NiO, θ -Al₂O₃ and NiAl₂O₄ phases were detected on the surface of the Ni-coated sample by XRD analysis as shown in **Fig. 4.5.2**. No θ -Al₂O₃ was detected on Cr-coated and Fe-coated samples as shown in **Fig. 4.5.3** and **Fig. 4.5.4**.

4.3.2.2 Oxide scale evaluation at the late stage of oxidation

Fig. 4.6 shows fractured cross sections and corresponding XRD patterns of pre-oxidized samples that were oxidized at 1000 °C for 100 h. The XRD patterns showed that the α -Al₂O₃ phase was completely developed on all samples including the bare alloy and Ni-coated samples after 100 h of oxidation at 1000 °C. The thickness of the Al₂O₃ scale formed on the bare alloy was the largest, and the thickness decreased in the order of Cr-coated > Fe-coated > Ni-coated samples. This order of thickness of the Al₂O₃ scale was in agreement with that of oxidation mass gain after 100 h as shown in **Fig. 4.4**. Moreover, the size of α -Al₂O₃ grains was found to strongly depend on the pre-coating element. Dependence of the parabolic rate constants, k_p , that was calculated at the late stage of oxidation on columnar grain size, r_G , that was measured from cross-sectional morphology is shown in **Fig. 4.7**.

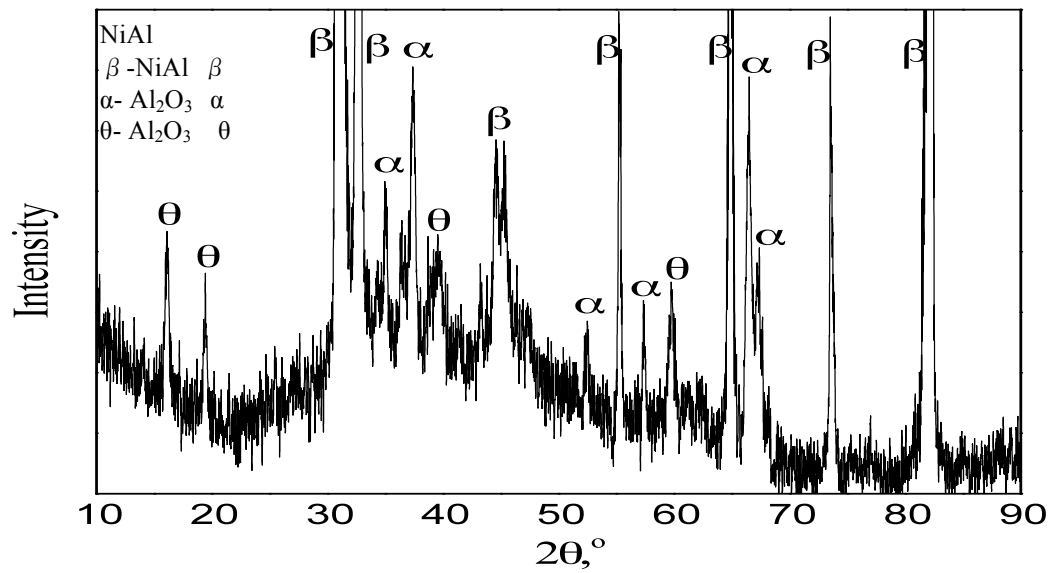
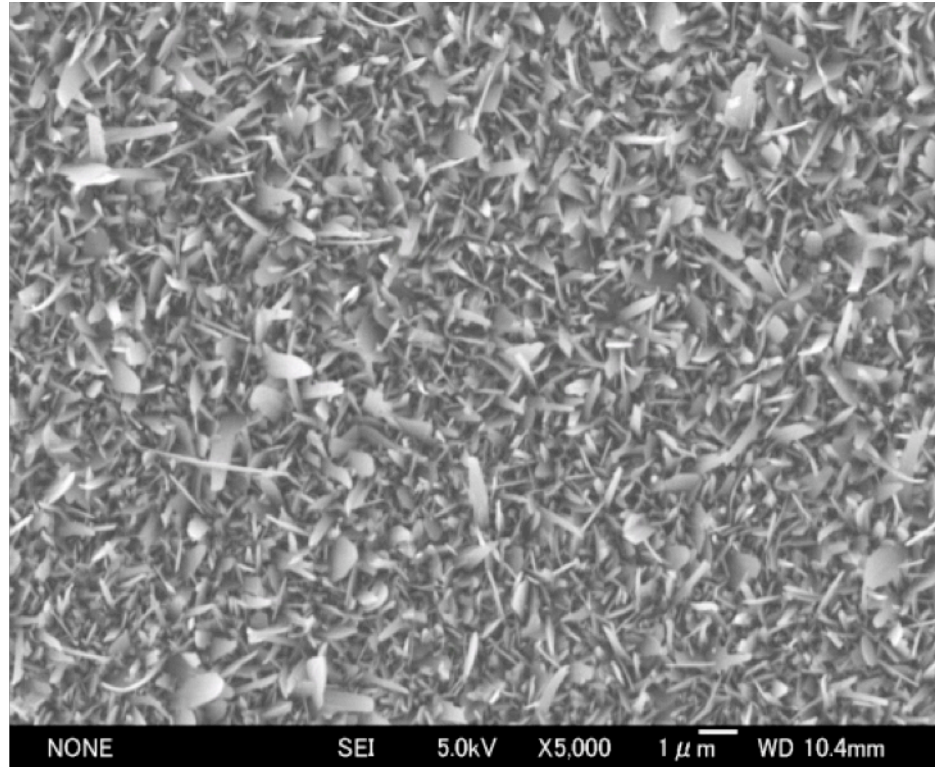


Figure 4.5.1: Surface morphology and corresponding XRD pattern of pre-oxidized NiAl sample (4 h at 900 °C) that was oxidized at 1000 °C for 4 h

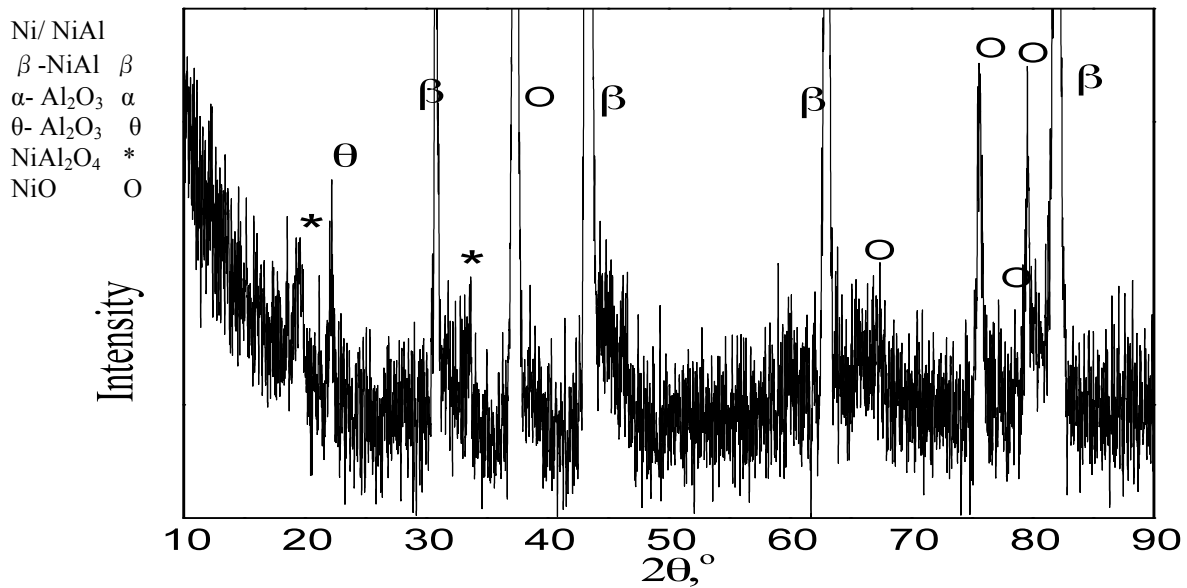
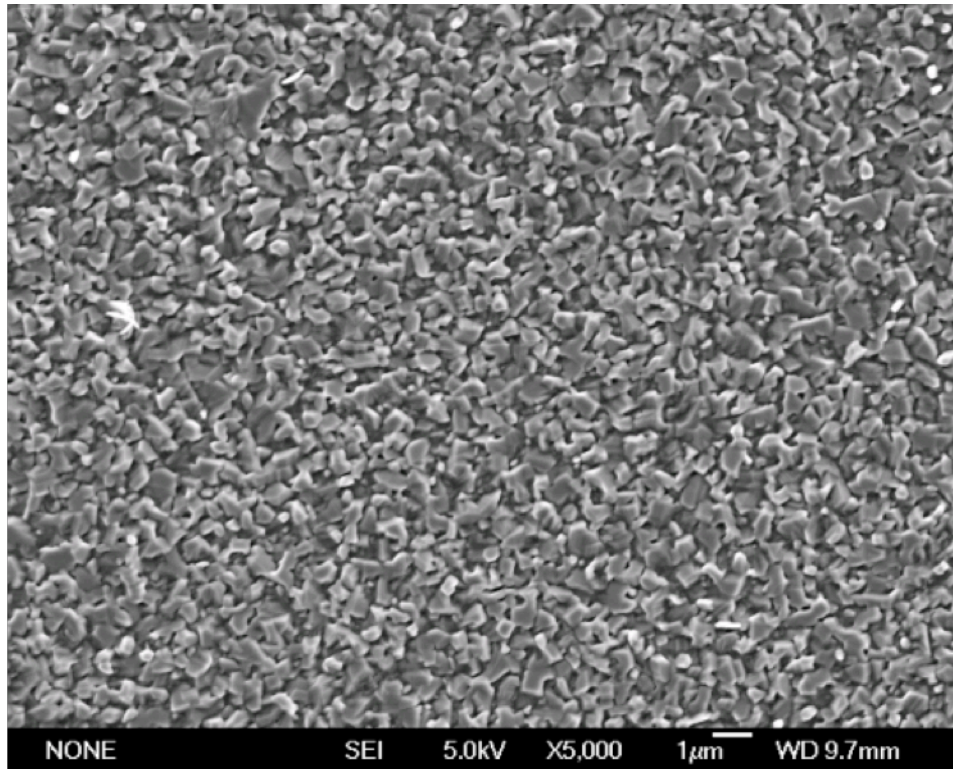


Figure 4.5.2: Surface morphology and corresponding XRD pattern of pre-oxidized Ni-coated NiAl sample (4 h at 900 °C) that was oxidized at 1000 °C for 4 h

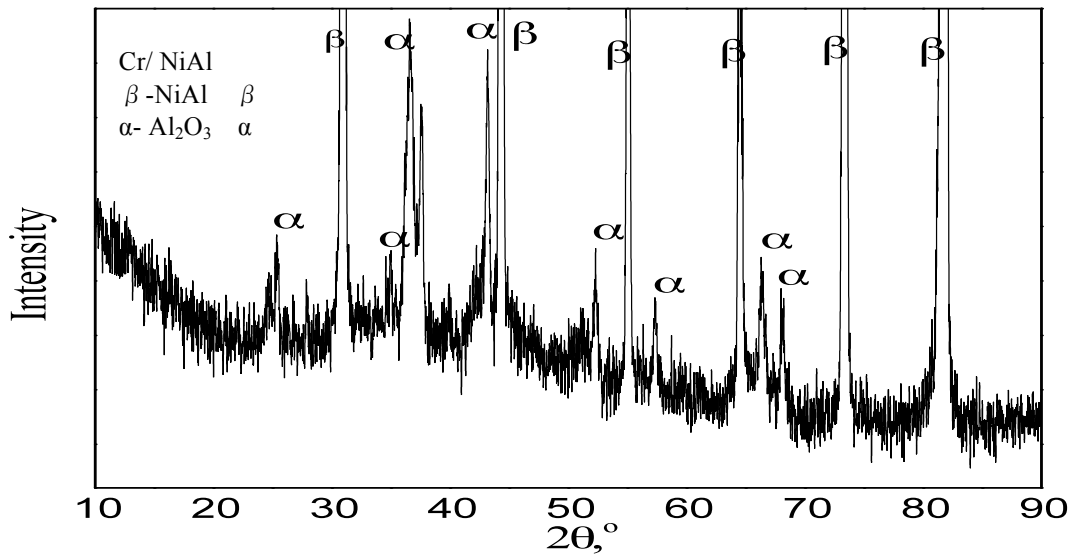
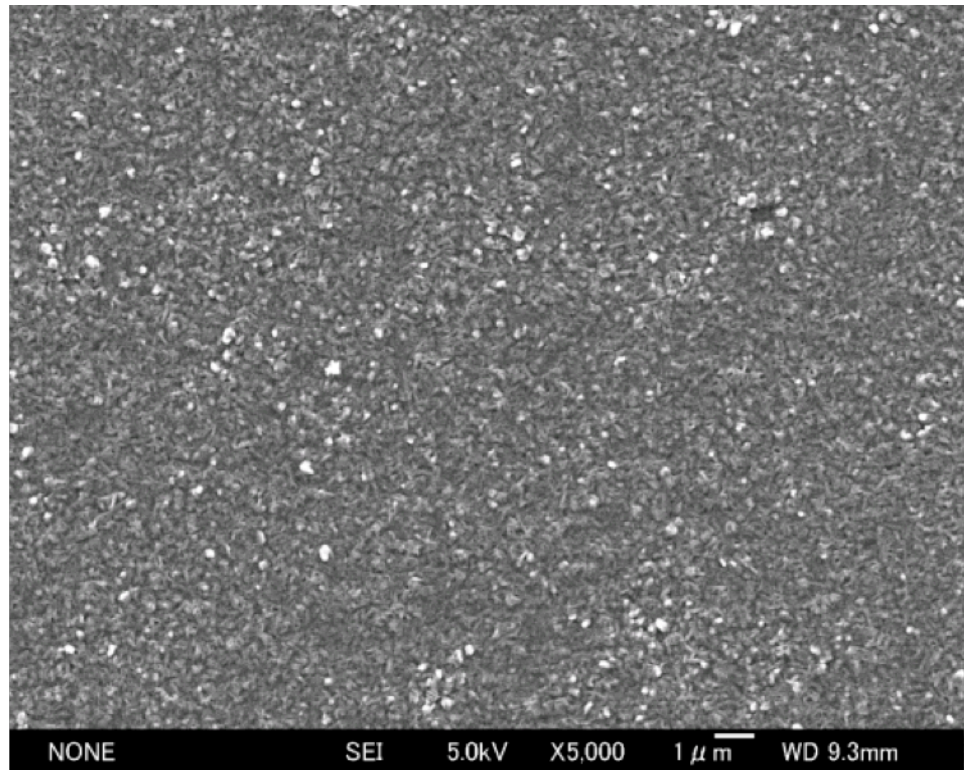


Figure 4.5.3: Surface morphology and corresponding XRD pattern of pre-oxidized Cr-coated NiAl sample (4 h at 900 °C) that were oxidized at 1000 °C for 4 h

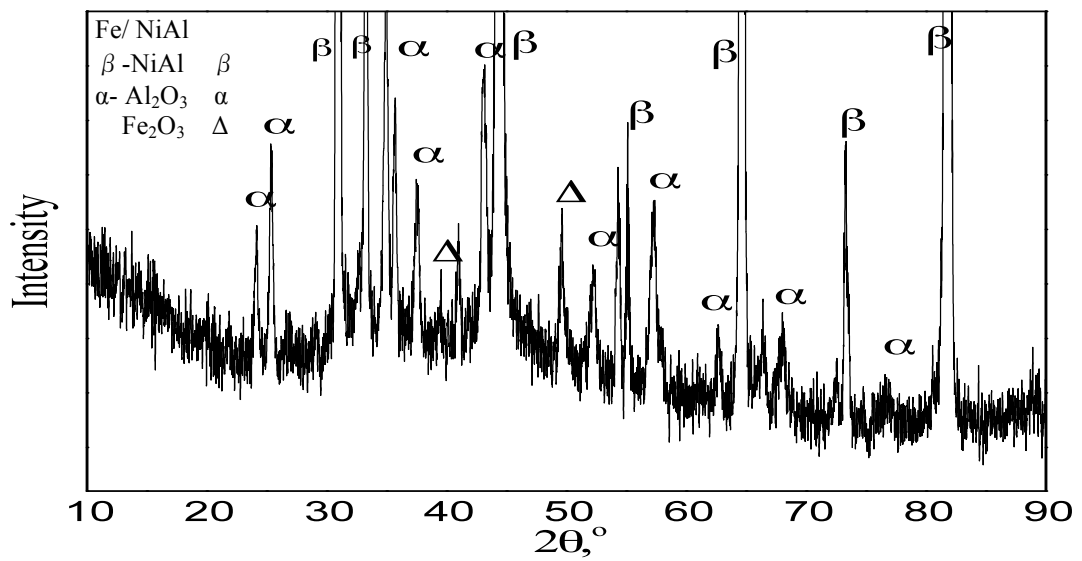
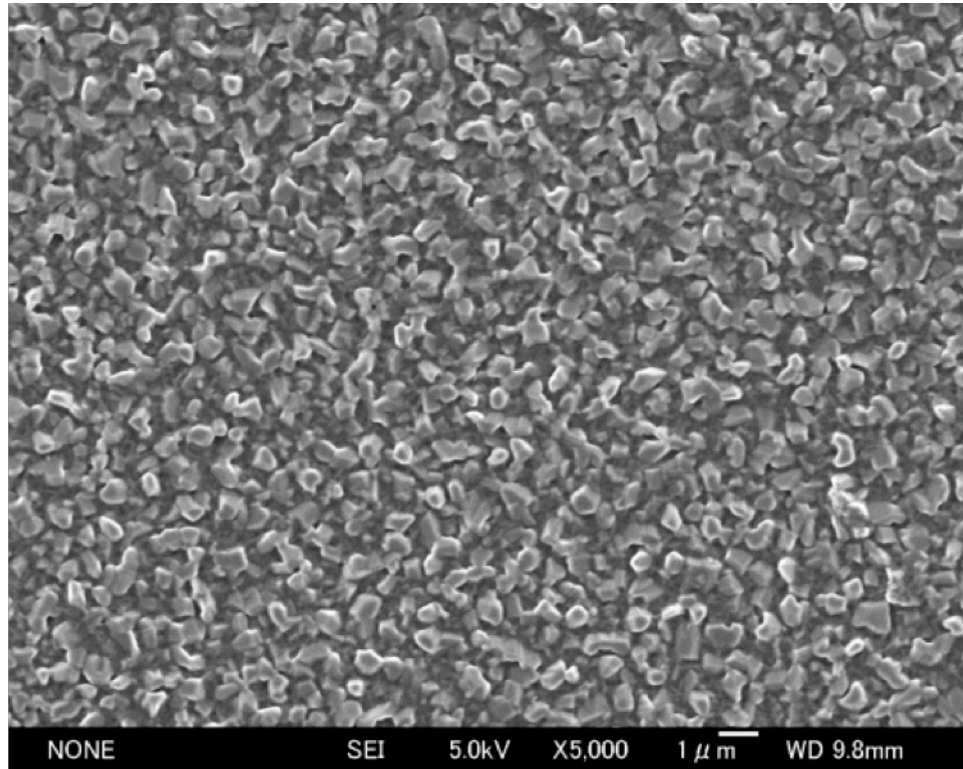


Figure 4.5.4: Surface morphology and corresponding XRD pattern of pre-oxidized Fe-coated NiAl sample (4 h at 900 °C) that were oxidized at 1000 °C for 4 h

The growth of alumina scales strongly depends on their microstructure [10, 11]. The growth of an Al₂O₃ scale is controlled by grain boundary diffusion of cations and anions [12]. Therefore, the parabolic rate constant of Al₂O₃ scale growth is strongly affected by the size of grains. A parabolic growth rate is defined as

$$\frac{dX}{dt} = k_p \cdot \frac{1}{X} \quad (1)$$

where X is the oxide scale thickness in cm , t is the oxidation time in s and k_p is the parabolic rate constant or oxide growth rate constant in $cm^2 \cdot s^{-1}$.

The diffusion flux of the diffusive carrier, i , is expressed as

$$J_i = \frac{-CD_{eff}}{RT} \frac{\partial \mu_i}{\partial y} \quad (2)$$

where C is the concentration of the mobile carriers, D_{eff} denotes the effective diffusion coefficient of cations or anions, μ_i is the chemical potential of the cations or anions, R is the gas constant and T is the kinetic temperature. Generally, D_{eff} can be defined as a weighted sum of the lattice diffusion D_L and the grain boundary diffusion D_{GB} coefficients with the fraction of the diffusion sites, f .

$$D_{eff} = (1 - f)D_L + fD_{GB} \quad (3)$$

For the grain size r_G and with a boundary width δ_{GB} , the number of the boundaries per unit area is $2/r_G$,

$$f = \frac{2\delta_{GB}}{r_G} \quad (4)$$

Aluminum and oxygen ions mainly diffuse through the grain boundaries [13]. Accordingly, the first term of eqn. (3) can be neglected and eqn. (3) can thus be approximated as

$$D_{eff} = \frac{2\delta_{GB}}{r_G} D_{GB}. \quad (5)$$

Combining eqns. (2) and (5),

$$J_i = \frac{-2C\delta_{GB}D_{GB}}{RTr_G} \frac{\partial\mu_i}{\partial y}. \quad (6)$$

By separation of variables and integration across the scale from $y=0$ to $y=X$,

$$\partial\mu_i = \frac{-J_i RTr_G}{2C\delta_{GB}D_{GB}} \int_0^X \partial y \quad (7)$$

It is assumed that the growth of an Al_2O_3 scale is mainly controlled by anion diffusion through grain boundaries and for simplicity the diffusion flux across the scale, J_i is assumed to be constant and independent of y ,

$$\mu_i = \mu'_i - \frac{J_i R T r_G}{2 C \delta_{GB} D_{GB}} X, \quad (8)$$

where μ'_i is the oxygen chemical potential at Al_2O_3 /air interface and X is the oxide scale thickness.

$$J_i = -2 C \delta_{GB} D_{GB} \frac{\Delta \mu_i}{RT} \frac{1}{X r_G} \quad (9)$$

From the diffusion analysis of scaling proposed by Wagner [14], the scale growth rate is given as,

$$\frac{dX}{dt} = J_i V_i, \quad (10)$$

Where V_i is the molar volume of the mobile carriers. Since $C_i V_i = 1$, eqn. (9) can be rewritten as

$$\frac{dX}{dt} = -2 \delta_{GB} D_{GB} \frac{\Delta \mu_i}{RT} \frac{1}{X r_G}. \quad (11)$$

Combining eqns. (1) and (11), parabolic rate constant of alumina scale growth, k_p , can be rewritten as a function of r_G :

$$k_p = -2 \left(\frac{\Delta\mu_i}{RT} \right) \delta_{GB} D_{GB} \frac{1}{r_G}. \quad (12)$$

This equation was obtained under the assumption that the oxide scale is uniform and has a constant thickness X . As shown in **Fig. 3.7**, fitting of the measured data shows the reverse proportional dependence of k_p on r_G , which qualitatively agrees with eqn. (12). By using the activity of Al in the NiAl alloy $a_{Al} = 9.3 \times 10^{-3}$ at 1273 K [15] and the standard free energy for the alumina formation $G^0_{1300K} = -1262 \text{ kJ.mol}^{-1}$ [16], the oxygen partial pressure $\ln P_{O_2}$ at the alloy/ Al_2O_3 interface could be obtained, and by neglecting $\ln P'_{O_2}$ because of the larger oxygen partial pressure P'_{O_2} at the Al_2O_3 /air interface, the value of the constant $(\Delta\mu_i/RT)$ could be calculated. By using this constant and the diffusion product value $\delta_{GB} D_{GB} = 2.1 \times 10^{-20} \text{ cm}^3 \cdot \text{s}^{-1}$ at 1000 °C [17] together with r_G that was measured from cross-sectional images, k_p values could be estimated and they are summarized in **Table 4.1**. Although some deviations were observed between the measured k_p values obtained from **Fig. 4.4b** and the values calculated from eqn. (12), the values are in a good agreement with each other.

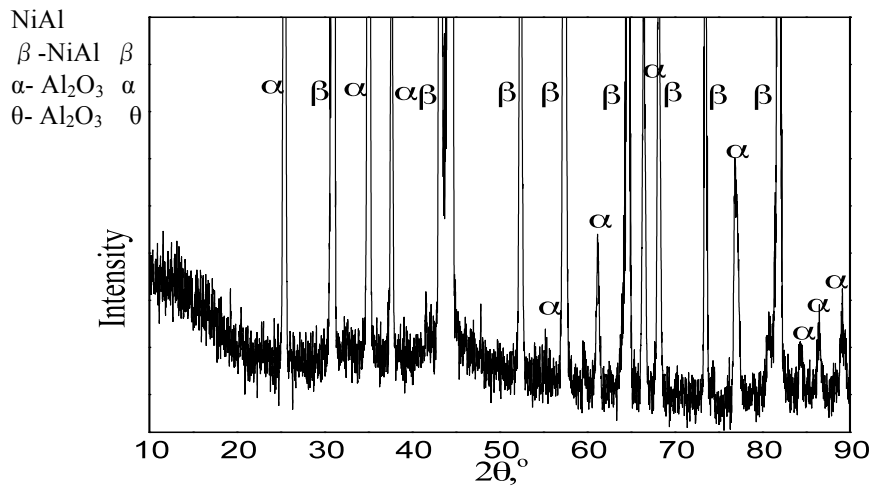
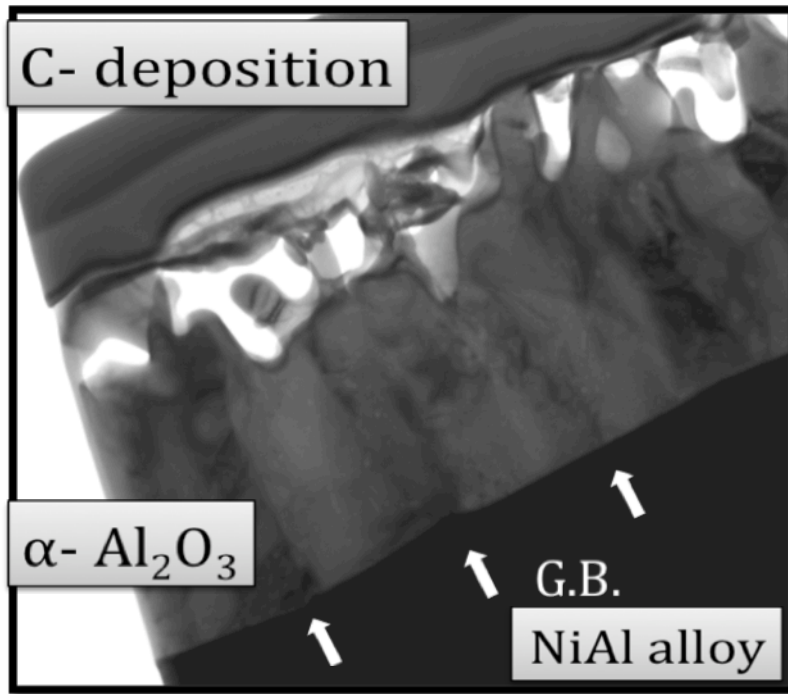


Figure 4.6.1: TEM cross-sectional morphology and corresponding XRD pattern of pre-oxidized NiAl sample (4 h at 900 °C) that was oxidized at 1000 °C for 100 h

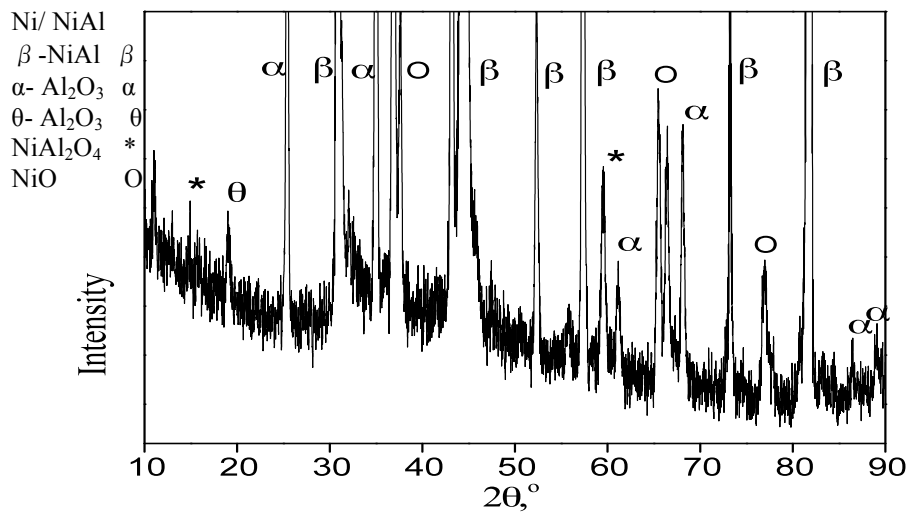
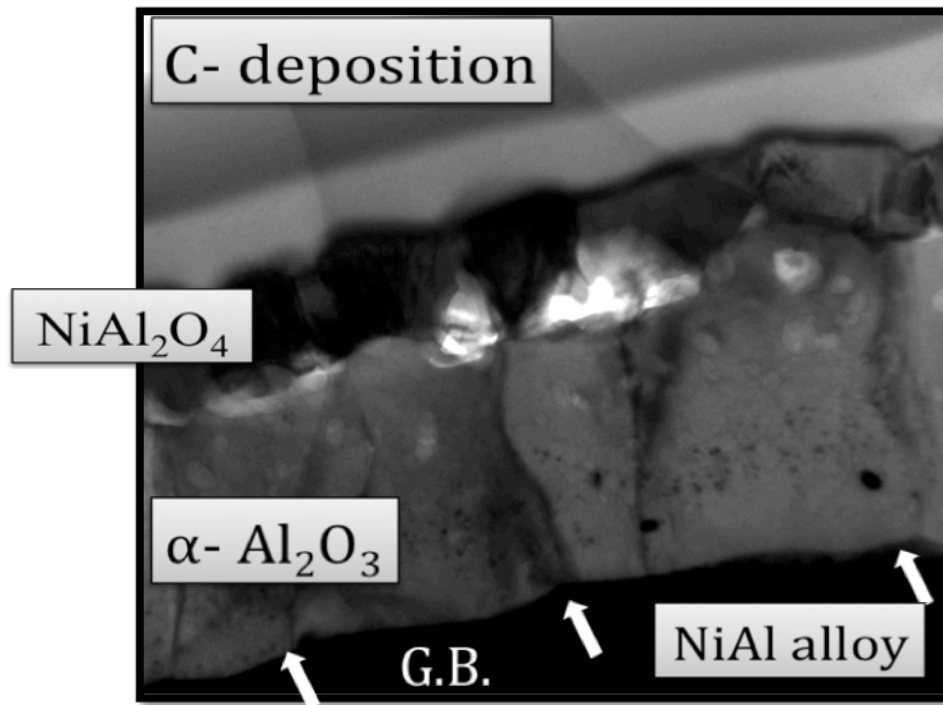


Figure 4.6.2: TEM cross-sectional morphology and corresponding XRD pattern of pre-oxidized Ni-coated NiAl sample (4 h at 900 °C) that was oxidized at 1000 °C for 100

h

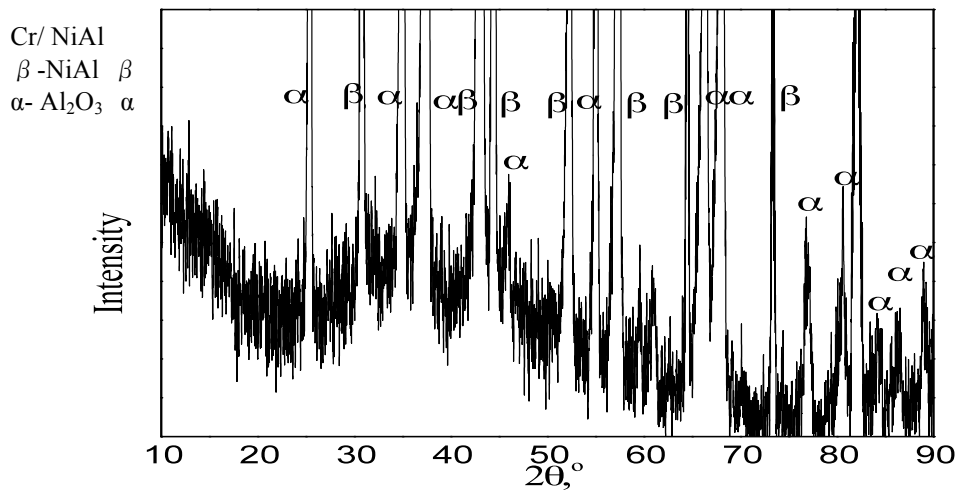
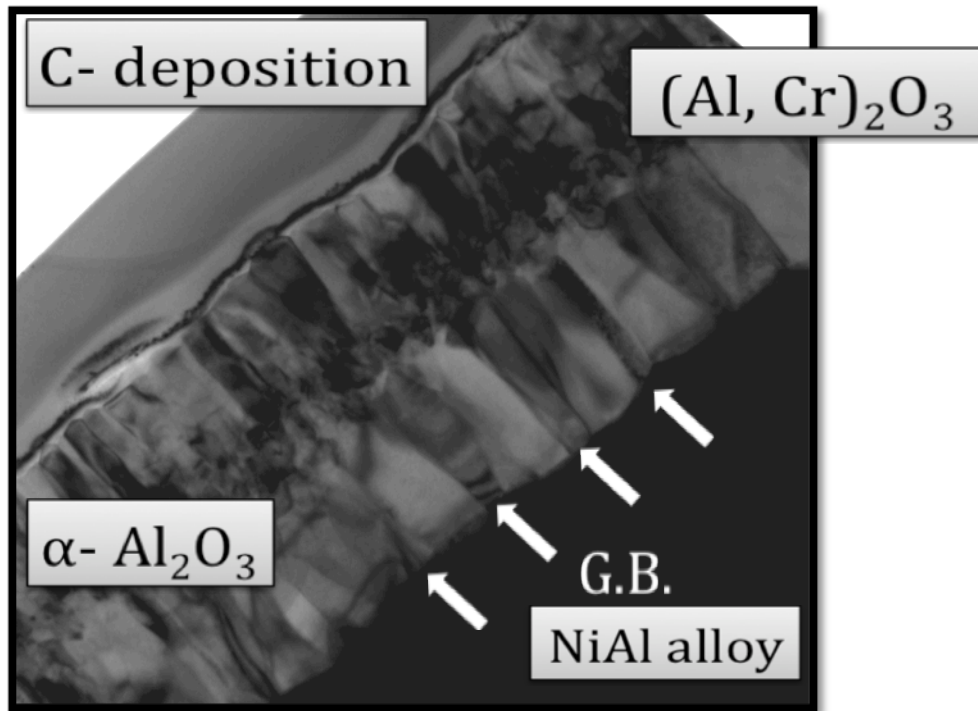


Figure 4.6.3: TEM cross-sectional morphology and corresponding XRD pattern of pre-oxidized Cr-coated NiAl sample (4 h at 900 °C) that were oxidized at 1000 °C for 100 h

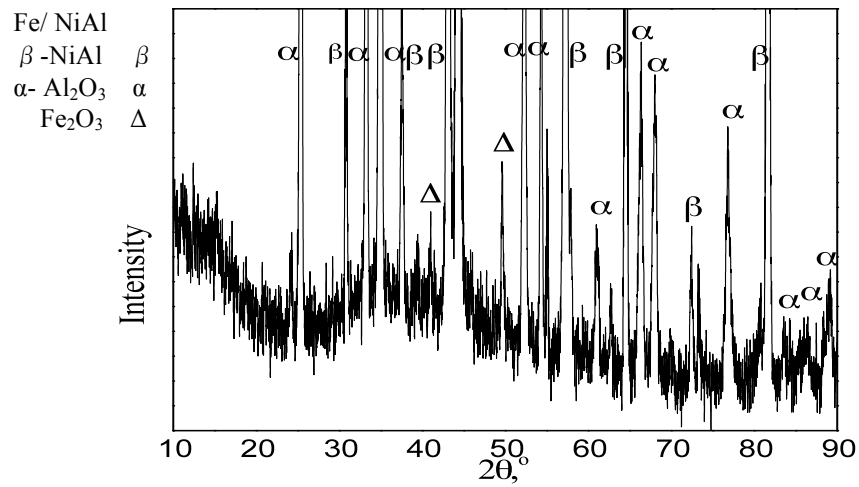
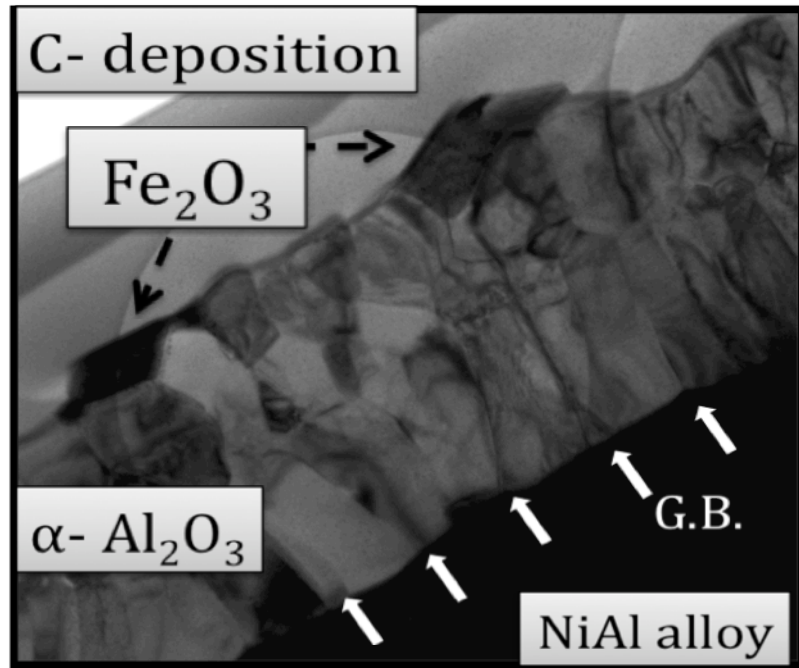


Figure 4.6.4: TEM cross-sectional morphology and corresponding XRD pattern of pre-oxidized Fe-coated NiAl sample (4 h at 900 °C) that were oxidized at 1000 °C for 100 h

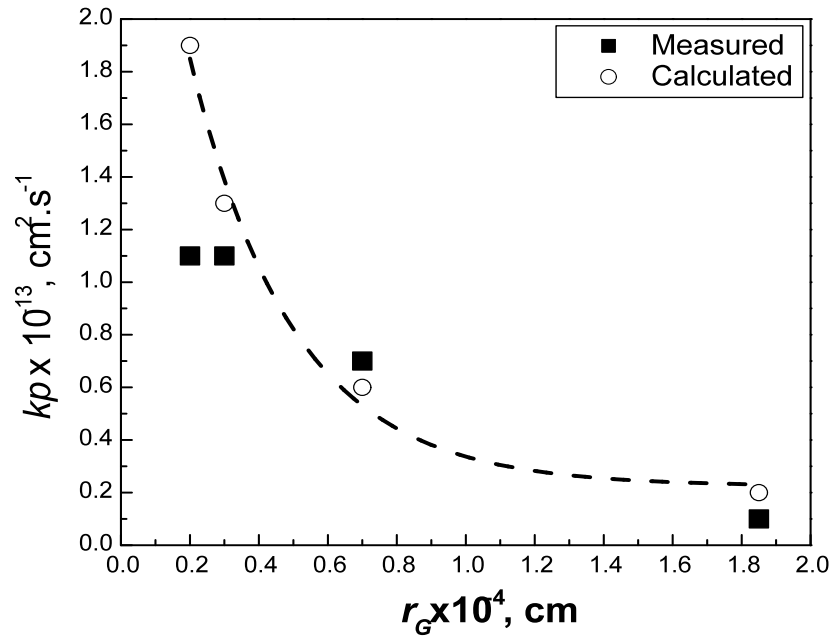


Figure 4.7: Dependence of the parabolic rate constant, k_p , of oxide scale growth of different coated samples on grain size, r_G , of the Al_2O_3 scale formed after 100 h of oxidation. Dashed curve represents the fitting of the calculated k_p values from eqn. (12)

Table 4.1. Parabolic rate constants of oxide scale growth, k_p values, at 1000 °C

Sample	Measured, TEM		Calculated, eqn. (12)	
	$\times 10^{-6} (\text{mg}^2 \cdot \text{cm}^{-4} \cdot \text{s}^{-1})$		$\times 10^{-13} (\text{cm}^2 \cdot \text{s}^{-1})$	
Bare alloy	1.1		0.7	0.6
Ni coating	0.2		0.1	0.2
Cr coating	1.4		1.1	1.9
Fe coating	1.4		1.1	1.3

As shown in **Figs. 4.3, 4.5 and 4.6**, the grain size of α -Al₂O₃ was smaller on alloys with a Cr or Fe precoating, on which θ -Al₂O₃ to α -Al₂O₃ transformation occurred rapidly. As mentioned previously from results of XRD analysis after pre-oxidation at 900 °C and as shown previously by Kitajima *et al.* [9], the Cr or Fe precoating suppress formation of θ -Al₂O₃. The rapid formation of α -Al₂O₃ is attributed to the formation of coated metal oxides, Cr₂O₃ and Fe₂O₃, which have an isomorphous corundum structure with α -Al₂O₃ [9, 18]. These metal oxides may provide a higher density of sites for α -Al₂O₃ nucleation, resulting in smaller grain size. A similar effect was observed on Ni-50Al with Cr addition by Brumm *et al.* [19]. They suggested that the introduction of Cr as an alloying element could increase the oxide mass gain, as shown in **Fig. 4.8**, due to the smaller size of grains.

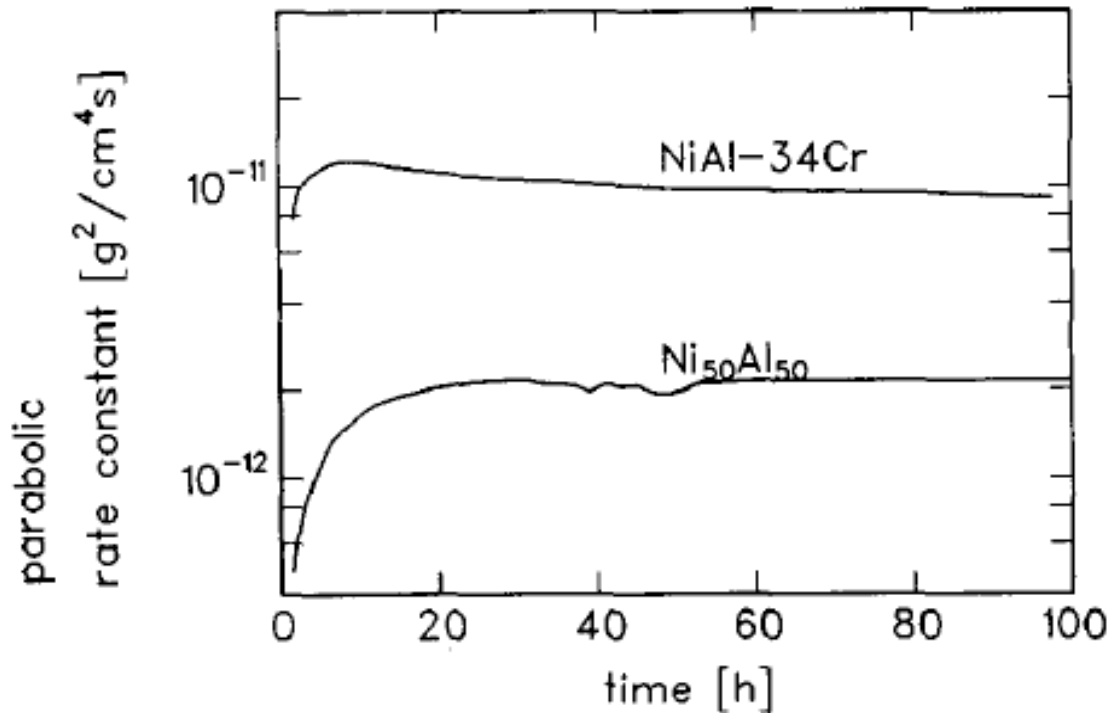


Figure 4.8: Effect of Cr addition on the oxidation growth rate constant of Ni50Al at 1200 °C [19]

On the alloy with the Ni precoating, the transformation to $\alpha\text{-Al}_2\text{O}_3$ was delayed; however, the oxidation mass gain was the smallest among the coated samples. The reason for the slower growth rate of $\theta\text{-Al}_2\text{O}_3$ formed on the Ni-coated sample is not clear present. It is likely that the formation of NiO and/or NiAl_2O_4 layer(s) above the $\theta\text{-Al}_2\text{O}_3$, at the early stage of oxidation, decreased the oxygen potential gradient across the $\theta\text{-Al}_2\text{O}_3$ scale because of the reduced oxygen potential at the NiO and/or $\text{NiAl}_2\text{O}_4/\theta\text{-Al}_2\text{O}_3$ interface and decreased the growth rate of $\theta\text{-Al}_2\text{O}_3$. The delay in transformation to $\alpha\text{-Al}_2\text{O}_3$ caused by the Ni precoating may be attributed to the similar isomorphism of $\theta\text{-Al}_2\text{O}_3$ and NiO and/or NiAl_2O_4 phases. It is well-known that $\theta\text{-Al}_2\text{O}_3$ and NiO and/or NiAl_2O_4 phases are related to the similar oxygen framework of face centred cubic (fcc) [20]. In the O^{2-} framework of $\theta\text{-Al}_2\text{O}_3$ phase, 1/2 of the Al^{3+} ions occupy octahedral interstitial sites and another 1/2 occupy tetrahedral sites. Meanwhile, the Ni^{2+} ions occupy all the octahedral interstitial sites of oxygen framework. Thus, the coexistence of NiO and/or NiAl_2O_4 phases probably stabilized $\theta\text{-Al}_2\text{O}_3$ phase for longer time and delayed the $\theta \rightarrow \alpha\text{-Al}_2\text{O}_3$ phase transformation. It is speculated that the delay in transformation to $\alpha\text{-Al}_2\text{O}_3$ apparently resulted in the largest grain size of $\alpha\text{-Al}_2\text{O}_3$ because of the low density of the nucleation sites of $\alpha\text{-Al}_2\text{O}_3$. The grain size of $\alpha\text{-Al}_2\text{O}_3$ formed on the bare alloy was not the smallest among the oxidized samples; however, the oxidation mass gain after 100 h of oxidation was the greatest. This is because of the rapidly growing $\theta\text{-Al}_2\text{O}_3$ that continuously grew thicker for a longer period of oxidation due to the delay in complete transformation to $\alpha\text{-Al}_2\text{O}_3$. Although the introducing of Ni-coating that resulted in largest grain size of $\alpha\text{-Al}_2\text{O}_3$ could slow the growth rate of the oxide scale, there is still a need for rapid $\theta \rightarrow \alpha\text{-Al}_2\text{O}_3$ phase transformation.

4.4. Conclusion

The effects of metal precoatings on the growth kinetics of α -Al₂O₃ formed on β -Ni-50Al at 1000 °C in air were investigated. The results are summarized as follows.

1. The parabolic rate constant of the α -Al₂O₃ scale formed on samples with different precoatings increased in the order of Ni-coated < bare alloy < Fe-coated < Cr-coated samples. This difference in the growth rate of α -Al₂O₃ was due to the different sizes of α -Al₂O₃ grains.
2. The size of α -Al₂O₃ grains formed on samples with different precoatings increased in the order of Cr-coated < Fe-coated < bare alloy < Ni-coated samples. This order was related to the time for θ -Al₂O₃ to α -Al₂O₃ phase transformation. The α -Al₂O₃ scale that transformed earlier always consisted of smaller grains, whereas the size of grains increased with delay in θ -Al₂O₃ to α -Al₂O₃ transformation.
3. Different metal precoatings affect the long-term oxidation kinetics of alumina scale growth at 1000 °C in air because they affect the θ -Al₂O₃ to α -Al₂O₃ phase transformation and the size of grains of the α -Al₂O₃ scale.

4.5. References

1. H. J. Grabke, *Intermetallics* 7, 1153–1158 (1999)
2. G. C. Rybicki and J. L. Smialek, *Oxidation of Metals*, 275–304 (1989)
3. H.J. Grabke, M.W. Brumm, B. Wagemann, *Materials and Corrosion*, 47, 675 (1996)
4. I. Rommerskirchen, B. Eltester, H. J. Grabke, *Materials and Corrosion*, 47, 646 (1996)
5. L. B. Pfeil, U.K. Patent no 459848, (1937)
6. L. B. Pfeil, U.K. Patent no 574088, (1945)
7. B. A. Pint, A. J. Garratt-Reed and L. W. Hobbs, *Journal of American Ceramic*

- Society, 81, 305-14 (1998)
8. S. Hayashi and B. Gleeson, *Oxidation of Metals*, 71, 5-19 (2009)
 9. Y. Kitajima, S. Hayashi, T. Nishimoto, T. Narita and S. Ukai, *Oxidation of Metals*, 73, 375–388 (2010)
 10. N. Birks, G. Meier, *Introduction to high temperature oxidation of metals*, Arnold, London (1993)
 11. K. Messaoudi, A. M. Huntz, B. Lesage, *Materials Science and Engineering*, A247, 248 (1998)
 12. A. H. Heuer, *Journal of the European Ceramic Society*, 28, 1495 (2008)
 13. S. Kitaoka, T. Matsudaira and M. Wada, *Materials Transactions*, 50, 1023-1031 (2009)
 14. C. Wagner, *Zeitschrift für Physikalische Chemie*, B21, 25 (1933)
 15. L. Bencze, D.D. Raj, D. Kath, W.A. Oates, L. Singheiser, and K. Hilpert, *Metallurgical and Materials Transactions B*, 35B, 867-876 (2004)
 16. I. Barin, *Thermochemical Data of Pure Substances*, 3rd edn., vol. I VCH Verlag Gesellschaft Weinheim, Germany (1995)
 17. D. J. Young, D. Naumenko, L. Niewolak, E. Wessel, L. Singheiser and W. J. Quadackers, *Materials and Corrosion*, 61, No. 10, 838- 844 (2010)
 18. Y. Kitajima, S. Hayashi, T. Nishimoto, T. Narita and S. Ukai, *Oxidation of Metals*, 75, 41–56 (2011)
 19. M.W. Brumm and H.J. Grabke, *Corrosion Science*, 33, 11, 1677-1690 (1992)
 20. N. Birks, G. Meier and S. Petit Frederick, *Introduction to high temperature oxidation of metals*, 2nd Ed., Cambridge, London (2004)

Chapter 5

PROMOTION OF α -Al₂O₃ FORMATION ON AN Ni-Al ALLOY USING A Ni-Fe₂O₃ NANO-COMPOSITE PRECOATING LAYER

In chapter four, effects of metal precoatings on the growth kinetics of α -Al₂O₃ formed on β -Ni-50Al at 1000 °C in air were investigated. The difference in the growth rate of α -Al₂O₃ was due to the different sizes of α -Al₂O₃ grains on different coated samples. The α -Al₂O₃ scale that transformed earlier always consisted of smaller grains, whereas the size of grains increased with delay in θ -Al₂O₃ to α -Al₂O₃ transformation. According to Kitajima *et al.* and based on the obtained results from the previous section, the formation of Fe-oxide (Fe₂O₃) may act as nucleation sites for α -Al₂O₃ phase formation and resulted in small grain size of α -Al₂O₃ while, Ni-coating was found to delay the transformation to α -Al₂O₃ and resulted in large grain size of α -Al₂O₃. Although the introducing of Ni-coating that resulted in largest grain size of α -Al₂O₃ could slow the growth rate of the oxide scale, there is still a need for rapid $\theta \rightarrow \alpha$ -Al₂O₃ phase transformation, which could be accomplished by adding heterogeneous nucleation sites for α -Al₂O₃.

In order to produce a protective α -Al₂O₃ with a slow growth rate, a hybrid-precoating layer of Ni-Fe₂O₃ composites will be deposited on NiAl prior to the oxidation.

Abstract

Thin precoating layers of Ni and Ni-Fe₂O₃ composites were successfully formed on an Ni50Al alloy using the pulse electrodeposition method (PED) from a Watts bath in order to promote α -Al₂O₃ formation for improving high temperature oxidation resistance of the Ni50Al alloy. The conditions for the PED and the effects of these precoating layers on Al₂O₃ scale formation on the Ni50Al alloy were investigated. The coated samples showed thicker oxide scales than bare Ni50Al samples in oxidation tests at 1000 °C in air. At the initial stage of oxidation (1 h), a single layer scale composed of blade-like crystals of meta-stable θ -Al₂O₃ was formed. The oxide scales formed on the PED coated samples had a multilayered structure consisting of an inner layer of either a mixture of θ -Al₂O₃ and α -Al₂O₃ or of single-phase α -Al₂O₃, intermediate NiAl₂O₄ layer and an outer NiO layer. The Ni-coating layer was found to delay the phase transformation of θ -Al₂O₃ to α -Al₂O₃ to 100 h of oxidation. Addition of 3.1%Fe₂O₃ to the Ni-coating layer accelerated the transformation of θ -Al₂O₃ to α -Al₂O₃ after 9 h of oxidation. Further addition of Fe₂O₃ nano-powder (5.2%~7.4%) to the Ni-coating layer successfully suppressed the θ -Al₂O₃ formation even at 1 h of oxidation. The Al₂O₃ phase structure and thickness of the oxide scales were found to be considerably affected by these precoating layers via two main factors: (i) formation of NiAl₂O₄ and (ii) the effect of Fe₂O₃ to accelerate the transformation of meta-stable Al₂O₃ to stable α -Al₂O₃ or to suppress the formation of meta-stable Al₂O₃.

Keywords: Ni50Al alloy; phase transformation; composite; Ni-coating; pulse electrodeposition

5.1. Introduction

Much interest has recently been shown in composite coatings because of the possible development of unique features [1-5]. For example, it has been reported that the addition of Al_2O_3 [6, 7], SiO_2 [8], TiO_2 [9], ZrO_2 [10], or La_2O_3 [11] to a coating layer improves hardness, wear resistance, corrosion resistance, and high temperature corrosion resistance and also induces electrical and magnetic properties. An electrochemical deposition method has been used to obtain composite coatings containing micro- and nano-sized particles [12]. Geng *et al.* studied the effect of a direct current (DC) electrodeposited Ni-2.12wt.% Fe_2O_3 composite coating on the thermal oxidation process of ferritic stainless steel used for the interconnects of a solid oxide fuel cell (SOFC) and found that the oxide scale formed at 800 °C showed high electric conductivity and provided an effective barrier against Cr outward migration to the surface but not against O inward migration [13]. It was also reported that pulse electrodeposition (PED) is more effective than DC electrodeposition in controlling or improving coating properties such as the particle distribution, structure, grain size, hardness, and wear resistance [14-22]. Various composite coatings including Ni-SiC [23], Ni-P-SiC [24], Ni- Al_2O_3 [25], Cu-CeO₂ [26], and Ni-TiO₂ [27] have been formed using PED.

The oxidation resistance of NiAl-based alloys depends on the formation of stable Al_2O_3 scales at a high temperature. Among these, α - Al_2O_3 is the most protective aluminum oxide because of its thermodynamic stability and slow growth rate [28, 29]. Therefore, rapid formation of α - Al_2O_3 is an attractive option to improve the high temperature oxidation resistance for alloys. It has been shown that the addition of small amounts of dopants to the substrate alloys promotes the formation of stable Al_2O_3 scales

[30, 31]. It was reported that Fe accelerated the transformation of meta-stable Al_2O_3 to stable $\alpha\text{-Al}_2\text{O}_3$ due to an isomorphism effect of Fe_2O_3 to $\alpha\text{-Al}_2\text{O}_3$, suggesting that Fe oxide acts as a “template” for the $\alpha\text{-Al}_2\text{O}_3$ scale formation [32-36]. Kitajima *et al.* reported that the formation of meta-stable Al_2O_3 was suppressed by oxidation in air at the relatively low temperature of 900 °C. They emphasized the beneficial effects of pre-deposition of Ti, Cr, and Fe on an Fe50Al alloy to form Ti_2O_3 , Cr_2O_3 , and Fe_2O_3 prior to the Al_2O_3 scale growth [37, 38]. They also observed detrimental effects of Al and Ni precoatings on the transformation of meta-stable Al_2O_3 to stable $\alpha\text{-Al}_2\text{O}_3$. It was found that Ni-coating both delays the transformation of $\theta\text{-Al}_2\text{O}_3$ to $\alpha\text{-Al}_2\text{O}_3$ at 1000°C in air as well as it results in enlarged grain sizes of the $\alpha\text{-Al}_2\text{O}_3$ and reduces the growth rate of oxide scales [39].

Based on these previous studies, the effects of Ni-coating layers co-deposited with different contents of Fe_2O_3 nano-powder electrodeposited by the PED method on the oxidation products and the thickness of oxide scales formed on an Ni50Al alloy in oxidation tests at 1000 °C in air were investigated. The influence of Fe_2O_3 nano-powder on the transformation of meta-stable Al_2O_3 to stable $\alpha\text{-Al}_2\text{O}_3$ and the rapid formation of $\alpha\text{-Al}_2\text{O}_3$ was also investigated.

5.2. Materials and methods

An Ni50Al alloy ingot was prepared from Al and Ni metals (~99.99% in purity) by the Ar-arc melting technique followed by homogenization at 1200 °C for 48 h in vacuum (5×10^{-3} Pa) and the alloy was cut into specimens of *ca.* 1 mm thickness. The specimens were ground with SiC paper (80, 200, 800, 1200, and 4000 grit) and finished with 3 μm diamond paste to obtain a mirror finish surface and then ultrasonically

degreased in acetone for 10 min. Then, Ni or Ni-Fe₂O₃ composite was electrodeposited on the Ni50Al sample from a Watts bath containing 250 g dm⁻³ of NiSO₄•6H₂O, 45 g dm⁻³ NiCl₂•6H₂O, 30 g dm⁻³ H₃BO₃, and 0, 20, or 100 g dm⁻³ of Fe₂O₃ powder of 40 nm average particle diameter at pH 4 by using a potentiostat (Ivium Technologies Co., model Iviumstat) and an electrochemical cell composed of an Ag/AgCl reference electrode, Ni sheet counter electrode, and Ni50Al working electrode. The PED was conducted at various conditions with solution stirring at 600 rpm. After the electrodeposition, the samples were subjected to high-temperature oxidation tests. Samples were placed in a furnace exposed to air, and the temperature was elevated at a rate of 10 °C min⁻¹ to 1000 °C and maintained for t_{ox} =1, 4, 9, 16, 25, 49, or 100 h and then cooled to room temperature. The resulting samples were used for an evaluation of the oxidation products, using FE-SEM with EDX (JEOL Co., model 6500F), TEM (JEOL Co., model JEM 2000FX, operated at 200 kV), multi-beam FIB-SEM (JEOL Co., model JIB-4600F/HDK), and XRD (JEOL Co., model JDX 3500, operated at 20 mA and 40 kV with CuK α radiation) for observation of the surface morphology and cross-sections, determination of the concentrations of Al, Ni, Fe, and O in the samples, and identification of oxidation products. For the cross-sectional observations of oxide scales by TEM, a carbon or tungsten layer was pre-deposited on the sample to protect the surface from Ga⁺ milling, and then a cross-sectioned sample was lifted out and attached to an Mo support grid that fits into the specimen holder of the TEM. In the TEM measurements, different microstructures were observed in bright field (BF) mode, and crystallographic analysis by selected area electron diffraction (SAED) with a double-tilt holder, and EDX analysis were also carried out.

5.3. Results and discussion

5.3.1. Properties of electrodeposited Ni and Ni-Fe₂O₃ composite precoating layers

The current waveform of the PED (pulse electro-deposition) is defined by the polarization time (t_{on}), resting time (t_{off}), and polarization (deposition) current density (i_{cd}).

Fig. 5.1 shows an example of the current waveform and potential response at the initial stage of the PED. The potential transient shows a decrease in overpotential during t_{on} due to the increase in the surface area of the Ni deposits and relaxation of the depleted layer of Ni²⁺ ions during t_{off} . Parameters for the electrodeposition conditions involved in PED are listed in **Table 5.1**.

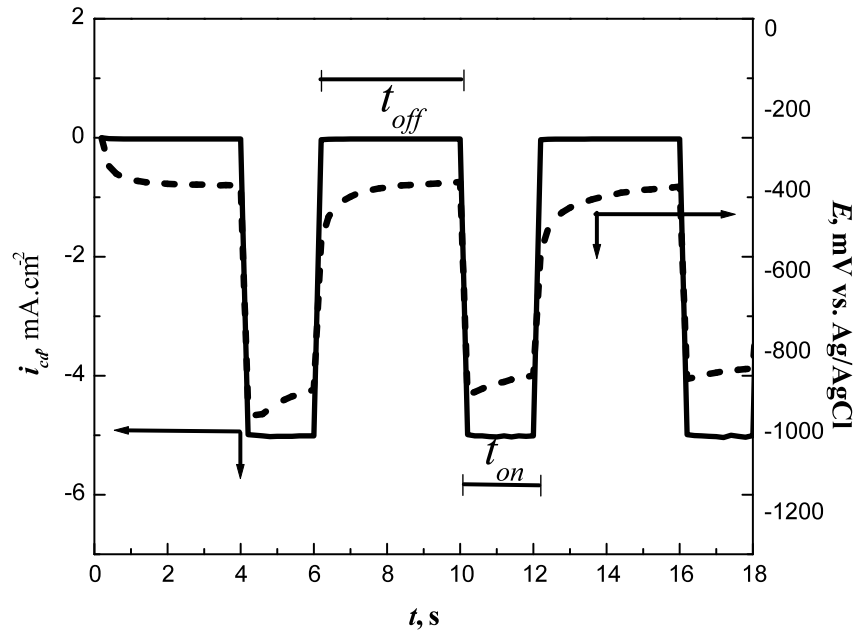


Figure 5.1: Current waveform for galvanostatic current pulse electrodeposition (PED) and potential response measured for electrodeposition of Ni on an NiAl alloy at $i_{cd} = -5$

$\text{mA}\cdot\text{cm}^{-2}$, $t_{on} = 2$ s, $t_{off} = 4$ s and $T = 25$ °C (Sample #1)

Table 5.1. PED conditions and resultant properties of Ni and Ni-Fe₂O₃ composite precoating layers

Sample #	[Fe ₂ O ₃] (g L ⁻¹)	<i>i</i> _{cd} (mA cm ⁻²)	<i>t</i> _{on} (s)	<i>t</i> _{off} (s)	<i>T</i> (°C)	[Fe] (wt. %)	[Fe ₂ O ₃] (V _f %)	<i>d</i> (nm)	<i>r</i> _{Ni} (nm)
1	0	-5	2	4	25	0	0	260	80-100
2	20	-5	2	4	25	3.5	3.1	270	50-70
3	20	-10	2	4	25	4.1	3.6	390	50 (200*)
4	20	-5	2	2	25	2.3	2.1	300	80-100
5	20	-5	2	4	45	1.3	1.1	530	50 (150*)
6	100	-10	2	4	45	5.8	5.2	580	100
7	100	-20	2	4	45	8.3	7.4	1270	100 (150*)

* Size of agglomerated particles

Formation of a compact Ni-coating layer with a nodular microstructure on the Ni50Al substrate was confirmed as shown in **Fig. 5.2** (sample #1 in **Table 5.1**). To avoid X-ray signals of the Ni50Al alloy substrate in the EDX analysis, a very small part of each of the precoating layers could be peeled off from the substrate by carbon double tape. The poor adhesion of the deposits did not affect the high temperature oxidation test. Average particle size of the Ni deposits was $r_{Ni} = ca. 100$ nm and the thickness of the Ni-coating layer was $d = ca. 260$ nm as estimated from the SEM images by ImageJ software. The electrodeposition efficiency calculated from the electric charge and the mass of deposits calculated with the assumption that the Ni-coating layer was a cubic crystal without voids or defects was $\eta = ca. 99\%$.

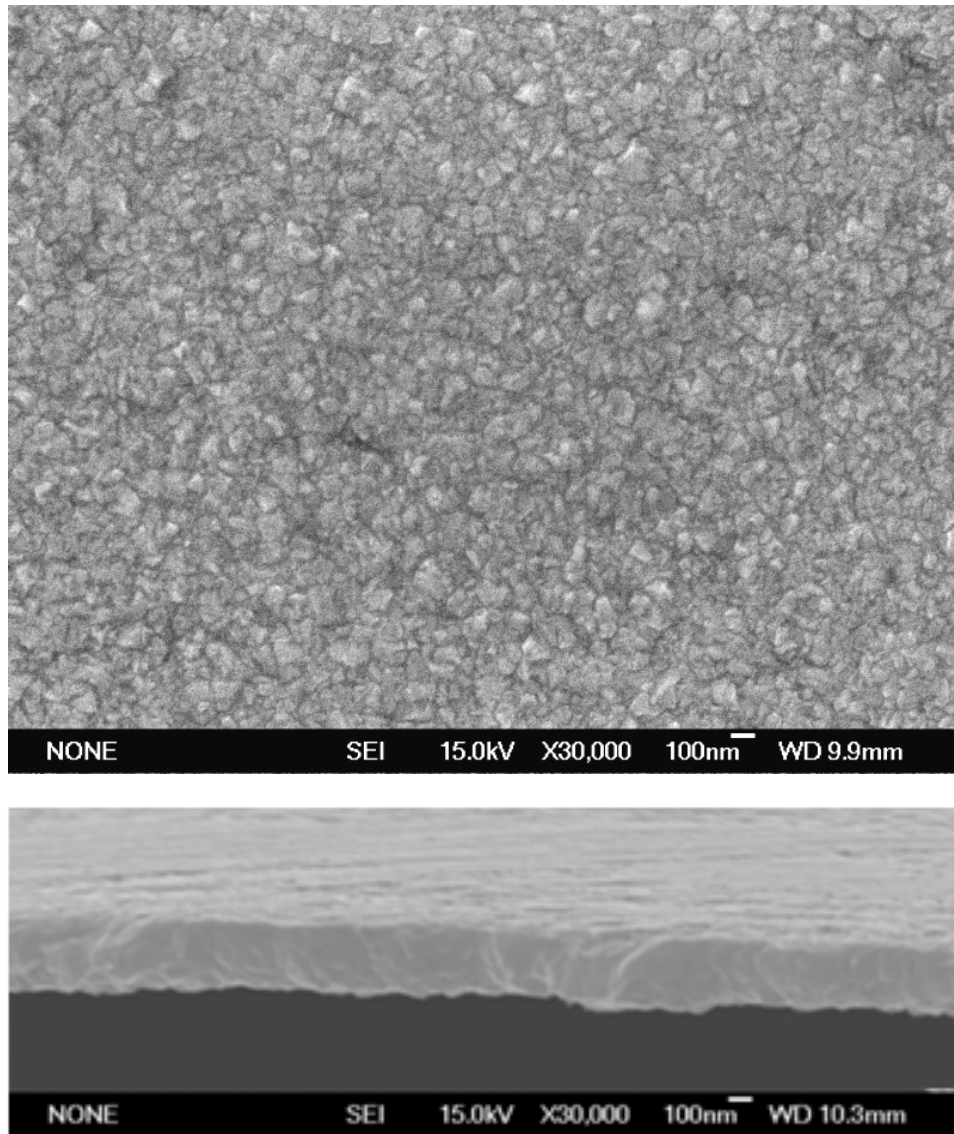


Figure 5.2: Surface and cross-sectional SEM images of an Ni-coating layer electrodeposited on NiAl with pulse conditions of $i_{cd} = -5 \text{ mA cm}^{-2}$, $t_{on} = 2 \text{ s}$, $t_{off} = 4 \text{ s}$ and $T = 25 \text{ }^\circ\text{C}$ (Sample #1)

Fig. 5.3 shows SEM images of the Ni-Fe₂O₃ composite precoating layer electrodeposited under the conditions listed in **Table 5.1**. The particle size of the composite precoating layer shown in **Fig. 5.3.1**, (sample #2), was smaller than that of the Ni-coating layer shown in **Fig. 5.2** (sample #1), which was deposited under the same

PED conditions. The smaller particle size may be attributed to the co-deposition of Fe_2O_3 nano-particles, which prevented continuous growth of the Ni nuclei in the deposition process. The thickness of the composite precoating layer was $d = ca. 270$ nm.

A comparison of **Fig. 5.3.1**, (sample #2), and **Fig. 5.3.2**, (sample #3), shows the influence of the deposition current density, i_{cd} , on the morphology of the precoating layer. The composite precoating layer deposited at $i_{cd} = -10$ mA cm⁻², which is shown in **Fig. 5.3.2**, was coarser and less uniform than that deposited at $i_{cd} = -5$ mA cm⁻², which is shown in **Fig. 5.3.1**, probably because the more rapid electrodeposition led to the growth of a depleted layer of Ni^{2+} ions near the surface in the bath and promoted preferential growth of larger particles. The precoating layer thickness increased from $d = 270$ nm at $i_{cd} = -5$ mA cm⁻² to $d = 390$ nm at $i_{cd} = -10$ mA cm⁻² due to the larger deposition charge.

A comparison of **Fig. 5.3.1**, (sample #2), and **Fig. 5.3.3**, (sample #4), suggests the effect of the duty ratio of the PED cycle on the precoating layer morphology. The surface of the composite precoating layer electrodeposited at $t_{on} = 2$ s and $t_{off} = 2$ s **Fig. 5.3.3** was rougher with larger particles than that of the composite precoating layer deposited at $t_{on} = 2$ s and $t_{off} = 4$ s **Fig. 5.3.1**. Generally, the PED method is used to mitigate undesired non-uniform electrodeposition caused by depletion of metal ions in the bath in the vicinity of the electrode surface. For example, a high deposition current density causes both rapid and dense nucleation on the surface and rapid growth of deposits as well as non-uniform growth of the deposits due to depletion of ions supplied from the bulk of the bath. To avoid non-uniform deposition, a resting time (t_{off}) is periodically introduced in the electrodeposition time (t_{on}). During t_{off} , metal ions migrate from the bulk of the bath to the depletion region to restore a sufficient concentration of ions for uniform deposition in the next t_{on} period [40]. The present results confirm that a longer t_{off} improves precoating

layer uniformity. From the potential response shown in **Fig. 5.1**, it is clear that $t_{\text{off}} = 4$ s was insufficient for a full recovery of the local concentration of Ni^{2+} ions but it seems adequate to mitigate the non-uniform deposition due to the localized depletion of ions.

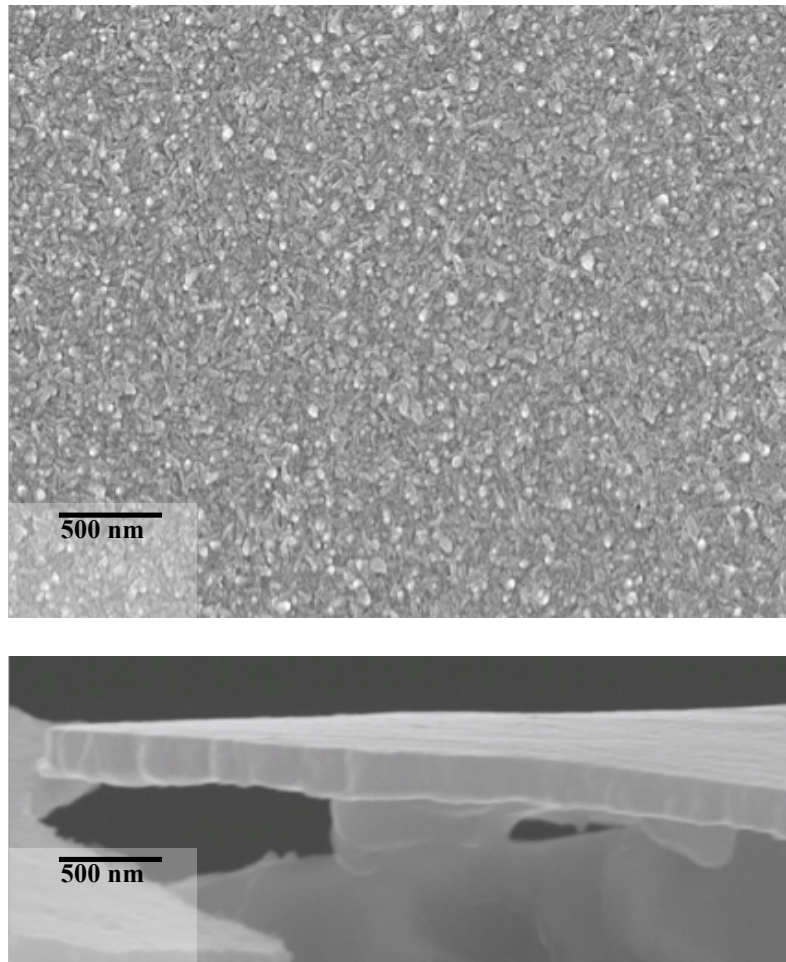


Figure 5.3.1: Surface morphology and cross-sectional SEM images of Ni-Fe₂O₃ composite precoating layers electrodeposited on Ni50Al for 450 s with pulse conditions of $i_{\text{cd}} = -5 \text{ mA cm}^{-2}$, $t_{\text{on}} = 2 \text{ s}$, $t_{\text{off}} = 4 \text{ s}$, 25 °C (sample #2)

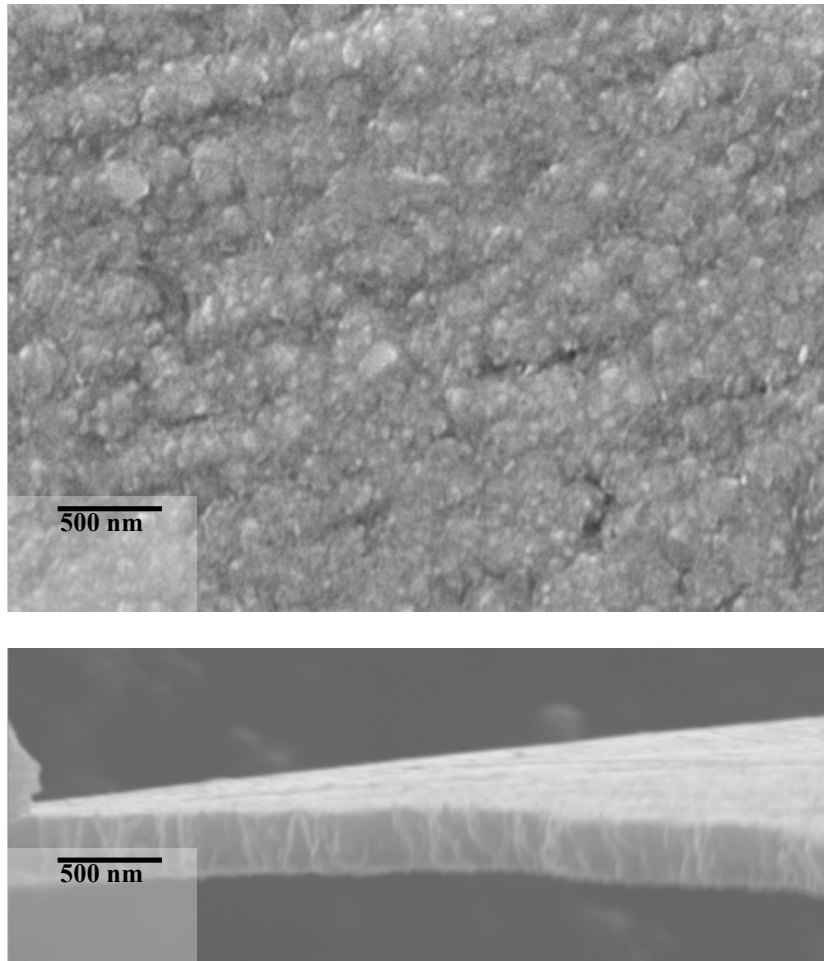


Figure 5.3.2: Surface morphology and cross-sectional SEM images of Ni-Fe₂O₃ composite precoating layers electrodeposited on Ni50Al for 450 s with pulse conditions of $i_{cd} = -10 \text{ mA cm}^{-2}$, $t_{on} = 2 \text{ s}$, $t_{off} = 4 \text{ s}$, 25 °C (sample #3)

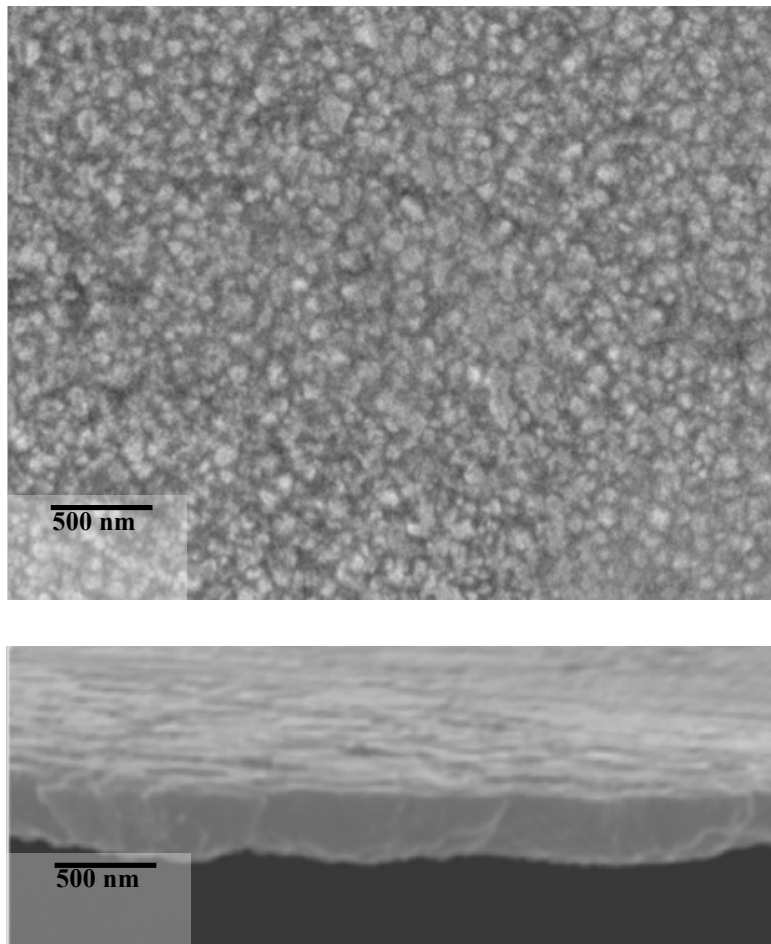


Figure 5.3.3: Surface morphology and cross-sectional SEM images of Ni-Fe₂O₃ composite precoating layers electrodeposited on Ni50Al for 450 s with pulse conditions of $i_{cd} = -5 \text{ mA cm}^{-2}$, $t_{on} = 2 \text{ s}$, $t_{off} = 2 \text{ s}$, 25 °C (sample #4)

Bath temperature is also an important parameter to consider in the control of deposit. Dini suggested that the grain size of the deposits increases with increases in bath temperature [41, 42]. A similar trend was also observed for nanocrystalline Al deposits [43]. It should be noted that increasing the bath temperature has two counteracting effects on the nucleation process: (i) an increase in the particle size of the Ni deposits due to the decrease in the thermodynamic driving force of crystallization, which leads to the aggregation of nuclei rather than the formation of new nuclei, as well as there is (ii) an increase in kinetic properties leading to a higher nucleation rate [44]. **Fig. 5.4** shows SEM images of the Ni-Fe₂O₃ composite precoating layer electrodeposited at a bath temperature of $T = 45$ °C as listed in **Table 5.1** (samples # 5-7). A comparison of **Fig. 5.3.1**, (sample #2), and **Fig. 5.4.1**, (sample #5), shows the effect of T on the morphology of deposits. Overall, the non-uniform deposition shown in **Fig. 5.4** would appear to be caused by the aggregation at a higher T than that in **Fig. 5.3**. The precoating layers deposited at $T = 45$ °C were more granular and thicker ($d = 530$ - 1270 nm) than the precoating layers deposited at 25 °C ($d = 270$ - 390 nm), it may be presumed that the precoating layers deposited at the temperature of $T = 45$ °C had lower densities due to the considerable amount of structural defects. The deposition temperature of $T = 45$ °C appears to be the less suitable for the formation of a uniform precoating layer, however the deposition at the higher temperature resulted in a higher content of Fe₂O₃ in the deposited layer, up to 7.4% when a high concentration of Fe₂O₃ nano-powder ($100 \text{ g}\cdot\text{L}^{-1}$) and a high electrodeposition current ($i_{cd} = -20 \text{ mA cm}^{-2}$) were used. These conditions could not be applied to electrodeposition at 25 °C.

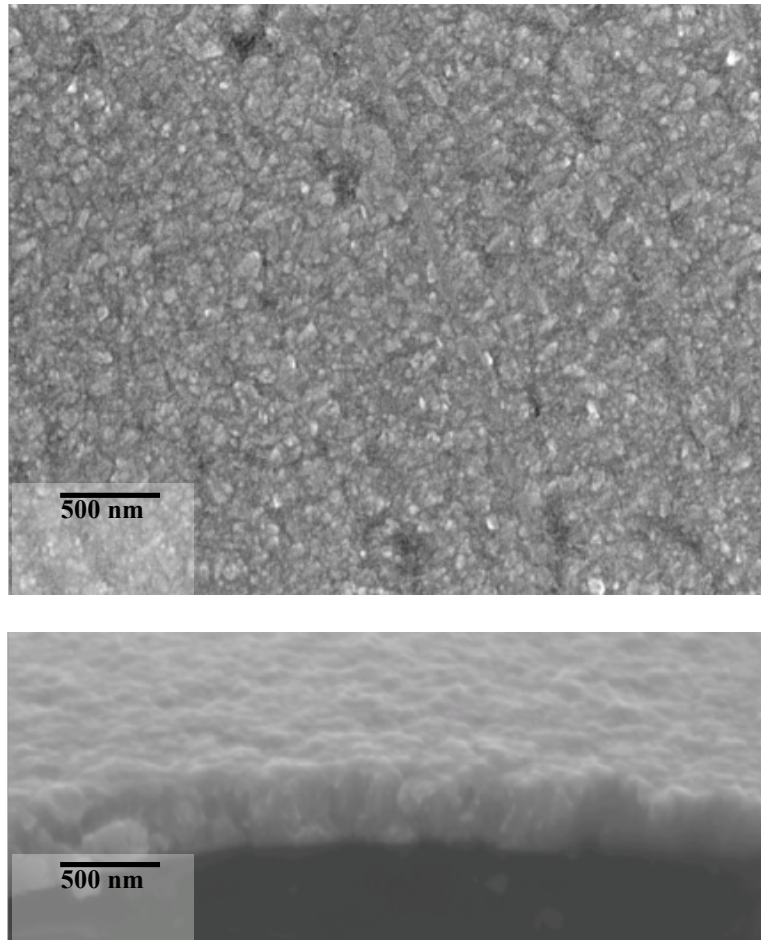


Figure 5.4.1: Surface morphology and cross-sectional SEM images of Ni-Fe₂O₃ composite precoating layers electrodeposited on Ni50Al for 450 s with pulse conditions of $i_{cd} = -5 \text{ mA cm}^{-2}$, $t_{on} = 2 \text{ s}$, $t_{off} = 4 \text{ s}$, 45 °C (Sample #5)

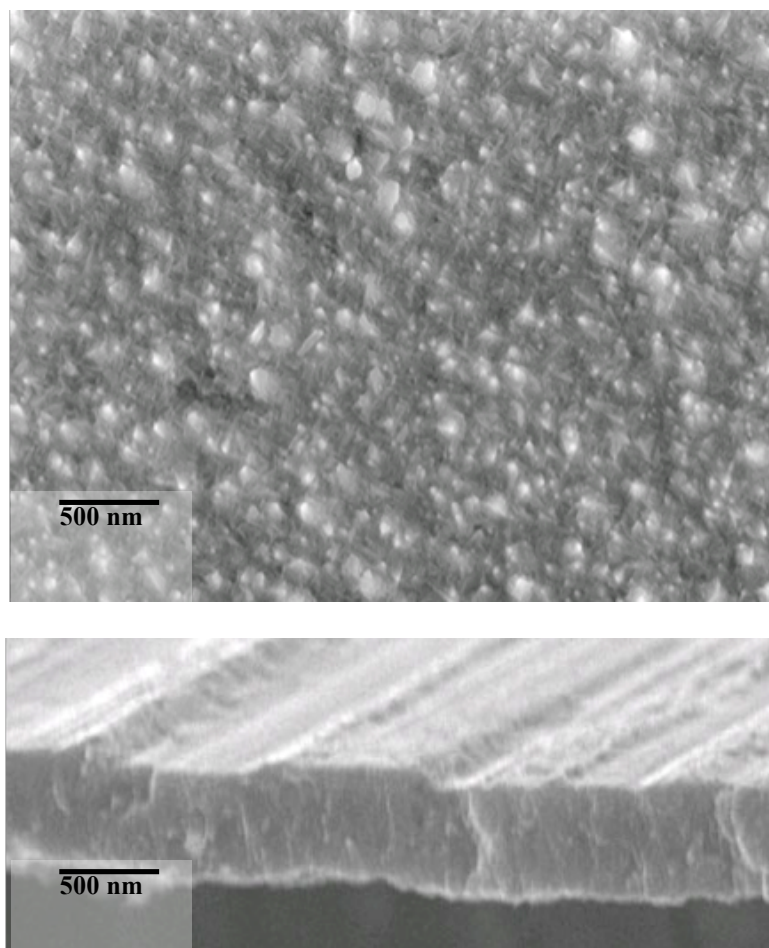


Figure 5.4.2: Surface morphology and cross-sectional SEM images of Ni-Fe₂O₃ composite precoating layers electrodeposited on Ni50Al for 450 s with pulse conditions of $i_{cd} = -10 \text{ mA cm}^{-2}$, $t_{on} = 2 \text{ s}$, $t_{off} = 4 \text{ s}$, 45 °C (Sample #6)

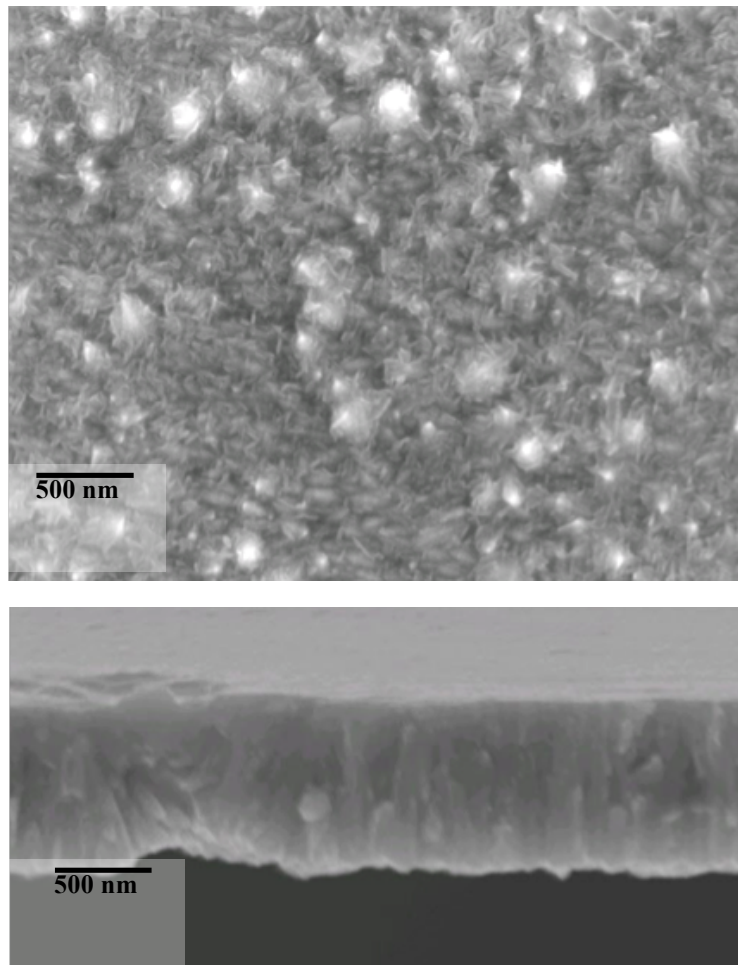


Figure. 5.4.3: Surface morphology and cross-sectional SEM images of Ni-Fe₂O₃ composite precoating layers electrodeposited on Ni50Al for 450 s with pulse conditions of $i_{cd} = -20 \text{ mA cm}^{-2}$, $t_{on} = 2 \text{ s}$, $t_{off} = 4 \text{ s}$, 45 °C (Sample #7)

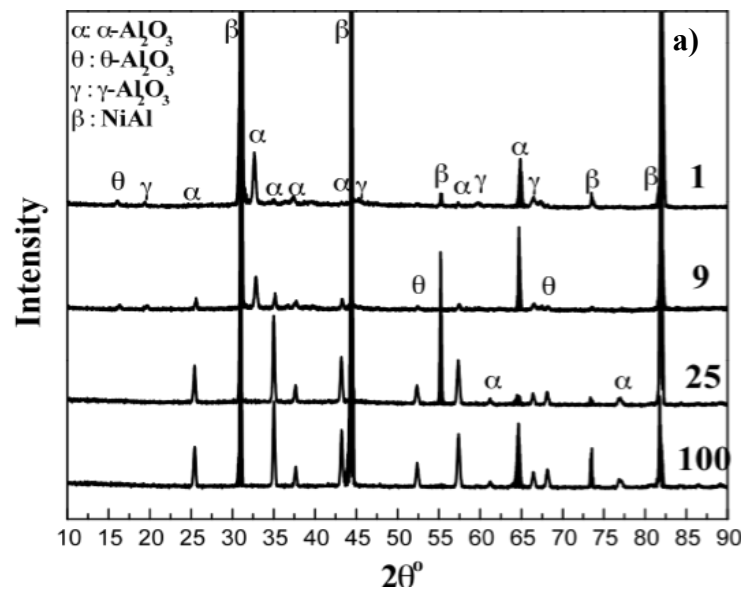
5.3.2. High temperature oxidation of Ni-coated and Ni-Fe₂O₃ composite-coated Ni50Al samples

The bare Ni50Al alloy, Ni50Al alloy coated with Ni (sample #1), Ni-3.1%Fe₂O₃ composite (sample #2), Ni-5.2%Fe₂O₃ composite (sample #6), and Ni-7.4%Fe₂O₃ composite (sample #7) precoating layers listed in **Table 5.1** were subjected to oxidation tests at 1000 °C in air. The XRD patterns of the oxidized samples and the generated peaks are shown in **Fig. 5.5** and **Table 5.2**. Peaks of the meta-stable γ -Al₂O₃, θ -Al₂O₃, and the stable α -Al₂O₃ phases were observed on the bare Ni50Al sample. Peaks of γ -Al₂O₃, θ -Al₂O₃, α -Al₂O₃, and NiO phases were observed on the Ni-coated and Ni-3.1%Fe₂O₃ composite-coated samples. Peaks of NiAl₂O₄, NiO, and α -Al₂O₃ phases were observed on the Ni-5.2%Fe₂O₃ and Ni-7.4%Fe₂O₃ composite-coated samples. At the initial stage of oxidation at $t_{ox} = 1$ h, strong peaks of predominantly NiO phase were detected for the Ni-coated **Fig. 5.5(b)** and Ni-Fe₂O₃ composite-coated (**Fig. 5.5(c), (d), and (e)**) samples due to oxidation of the Ni precoating layers. The θ -Al₂O₃ phase was detected on the Ni-coated and Ni-3.1%Fe₂O₃ composite-coated samples but not on the composite-coated samples with Fe₂O₃ content higher than 5%. No peaks of Fe₂O₃ were detected here because the remaining Fe₂O₃ concentration in the precoating layer was below the detection limit of the XRD. Peaks from FeAl₂O₄ or NiFe₂O₄ spinel phase were also not detected due to their low contents in the scale.

Fig. 5.6 shows the surface morphology and corresponding cross-sectional microstructure of oxide scales formed on the bare Ni50Al. At $t_{ox} = 1$ h there was a single layer composed of blade-like crystals as shown in **Figs. 5.6(a)** and **(c)**. This morphology is typical for transient phases of Al₂O₃ such as θ -Al₂O₃ [2, 7, 39, 45, 46]. Although α -Al₂O₃ was detected on the bare Ni50Al sample in the XRD sample as shown in **Fig.**

5.5(a), grains of α -Al₂O₃ were not observed in the surface or cross-sectional images in the limited area of the scale observed. The blade-like morphology at $t_{\text{ox}} = 1$ h changed to needle-like morphology at $t_{\text{ox}} = 100$ h, here columnar grains of α -Al₂O₃ were observed underneath the needle-like θ -Al₂O₃ layer as shown in **Fig. 5.6(d)**.

Fig. 5.7 shows the surface morphology and corresponding cross-sectional microstructure of oxide scales formed on Ni50Al samples coated with precoating layers at the early stage of oxidation ($t_{\text{ox}} = 1$ h) in air. It has been reported that the morphology of the oxidized Ni surface changes with the oxidation temperature [47]. In the temperature range above $T = 1000\sim 1100$ °C, the surface of the scale was composed of faceted NiO grains [47] similar to the morphology shown in **Fig. 5.7**. A cross-sectional image of the scale formed on the Ni-coated sample **Fig. 5.7.1** shows that the outer layer of the faceted NiO uniformly covered the inner oxide layer. There were also NiO grains covering the surface of the Ni-Fe₂O₃ composite-coated samples (**Fig. 5.7.2 - Fig. 5.7.4**), less uniformly than those covering the Ni-coated sample in **Fig. 5.7.1**.



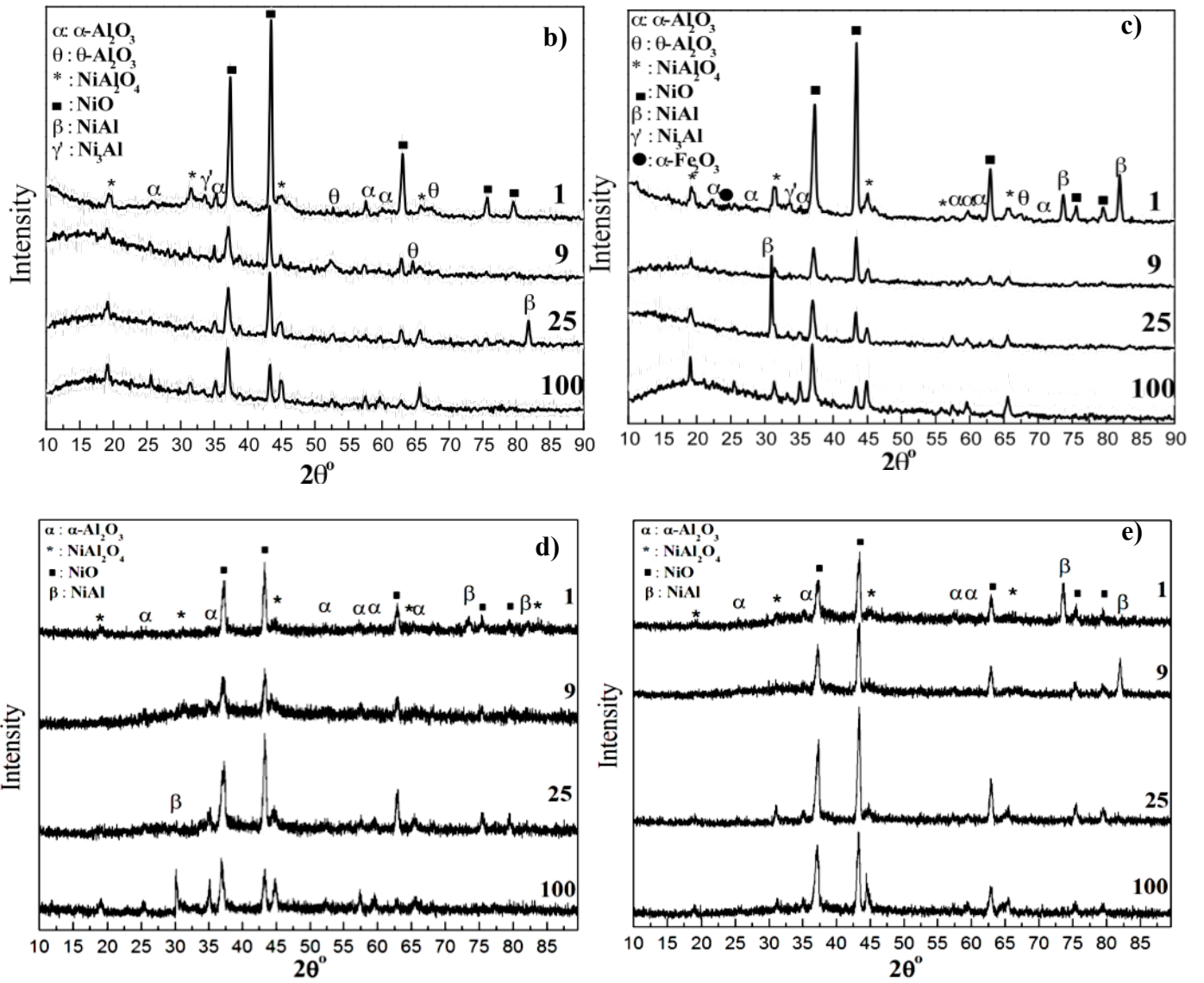


Figure 5.5: XRD patterns of oxidized samples at 1000 °C for different oxidation times, t_{ox} : bare Ni50Al (a), Ni50Al coated with Ni (Sample #1) (b), Ni-3.1% Fe_2O_3 (Sample #2) (c), Ni-5.2% Fe_2O_3 (Sample #6) (d) and Ni-7.4 Fe_2O_3 (Sample #7) (e)

Table 5.2. Details of the detected XRD phases

Precoating	t_{ox} (h)	β -NiAl	γ' -Ni ₃ Al	NiO	γ -Al ₂ O ₃	θ -Al ₂ O ₃	α -Al ₂ O ₃	NiAl ₂ O ₄
-----	1	β			γ	θ	α	
	9	β			γ	θ	α	
	25	β			γ		α	
	100	β			γ		α	
Ni	1		γ'	■		θ	α	*
	9		γ'	■		θ	α	*
	25	β	γ'	■		θ	α	*
	100		γ'	■		θ	α	*
Ni-3.1% Fe ₂ O ₃	1	β	γ'	■		θ	α	*
	9	β	γ'	■			α	*
	25	β	γ'	■			α	*
	100		γ'	■			α	*
Ni-5.2 % Fe ₂ O ₃	1	β		■			α	*
	9			■			α	*
	25	β		■			α	*
	100	β		■			α	*
Ni-7.4 % Fe ₂ O ₃	1	β		■			α	*
	9	β		■			α	*
	25			■			α	*
	100			■			α	*

The cross-sectional TEM images shown in **Figs. 5.7** indicate that the scales formed on the Ni-coated and Ni-Fe₂O₃ composite-coated samples had a triplex layer structure and were thicker than the scale of the bare Ni50Al sample, this may arise due to the fast growth of outer NiO phase at the initial stage of oxidation ($t_{\text{ox}} = 1$ h). An EDX point analysis revealed that the averaged compositions of the outer / intermediate / inner layers were Ni_{0.32}Al_{0.02}O_{0.66} / Ni_{0.31}Al_{0.33}O_{0.36} / Ni_{0.09}Al_{0.21}O_{0.70} for the Ni-coated sample and Ni_{0.39}Al_{0.01}O_{0.60} / Ni_{0.39}Al_{0.2}O_{0.41} / Ni_{0.01}Al_{0.31}O_{0.68} for the Ni-Fe₂O₃ composite-coated samples. The NiAl₂O₄ was present as an intermediate layer between the outer NiO and inner Al₂O₃ layers as shown in **Fig. 5.7.2b**, **Fig. 5.7.3b** and **5.7.4b** or as discontinuous islands as shown in **Fig. 5.7.1(b)**, here due to the insufficient thickness not being able to form a continuous layer. This triplex oxide scale can therefore be represented as NiO / NiAl₂O₄ / Al₂O₃ phases [37-39, 48]. According to the Pilling–Bedworth ratio of NiO (1.65) and from the cross-sectional TEM images shown in **Figs. 5.7**, the thickness of the outer NiO layer at $t_{\text{ox}} = 1$ h depended on the initial thickness of the Ni-coating layer, *i.e.*, a thicker Ni-coating layer provided a thicker NiO layer. The α -Al₂O₃ and/or θ -Al₂O₃ inner layers on all the coated samples were thinner than that on the bare Ni50Al sample as indicated by a comparison of **Fig. 5.7.1b**, **Fig. 5.7.2b**, **Fig. 5.7.3b** and **Fig. 5.7.4b**. The inner layer tends to become thinner with increases in the content of Fe₂O₃ in the Ni-coating layers. The thinning of an inner Al₂O₃ layer could be attributed to the rapid formation of α -Al₂O₃ on the coated samples at the higher Fe₂O₃ content as will be discussed below.

From the results obtained in this study, the following reactions may be postulated to occur during the oxidation of coated samples: (process I) formation and growth of NiO, (process II) formation of NiAl₂O₄ spinel by a solid phase reaction of NiO and Al₂O₃,

(process III) a meta-stable to stable- Al_2O_3 phase transformation, and (process IV) the direct formation of $\alpha\text{-Al}_2\text{O}_3$ without formation of meta-stable Al_2O_3 . At the initial stage of oxidation of the samples coated with Ni-coating layers in air, Ni is oxidized to form NiO. The NiO continues to grow until the surface layer of Ni is completely consumed by process I. Beneath the NiO scale, the Al in the substrate alloy is selectively oxidized to form stable or meta-stable Al_2O_3 . After the Al_2O_3 scale formation, solid phase reactions of NiO with Al_2O_3 of any phases present may occur to form NiAl_2O_4 spinel on all the coated samples (process II).

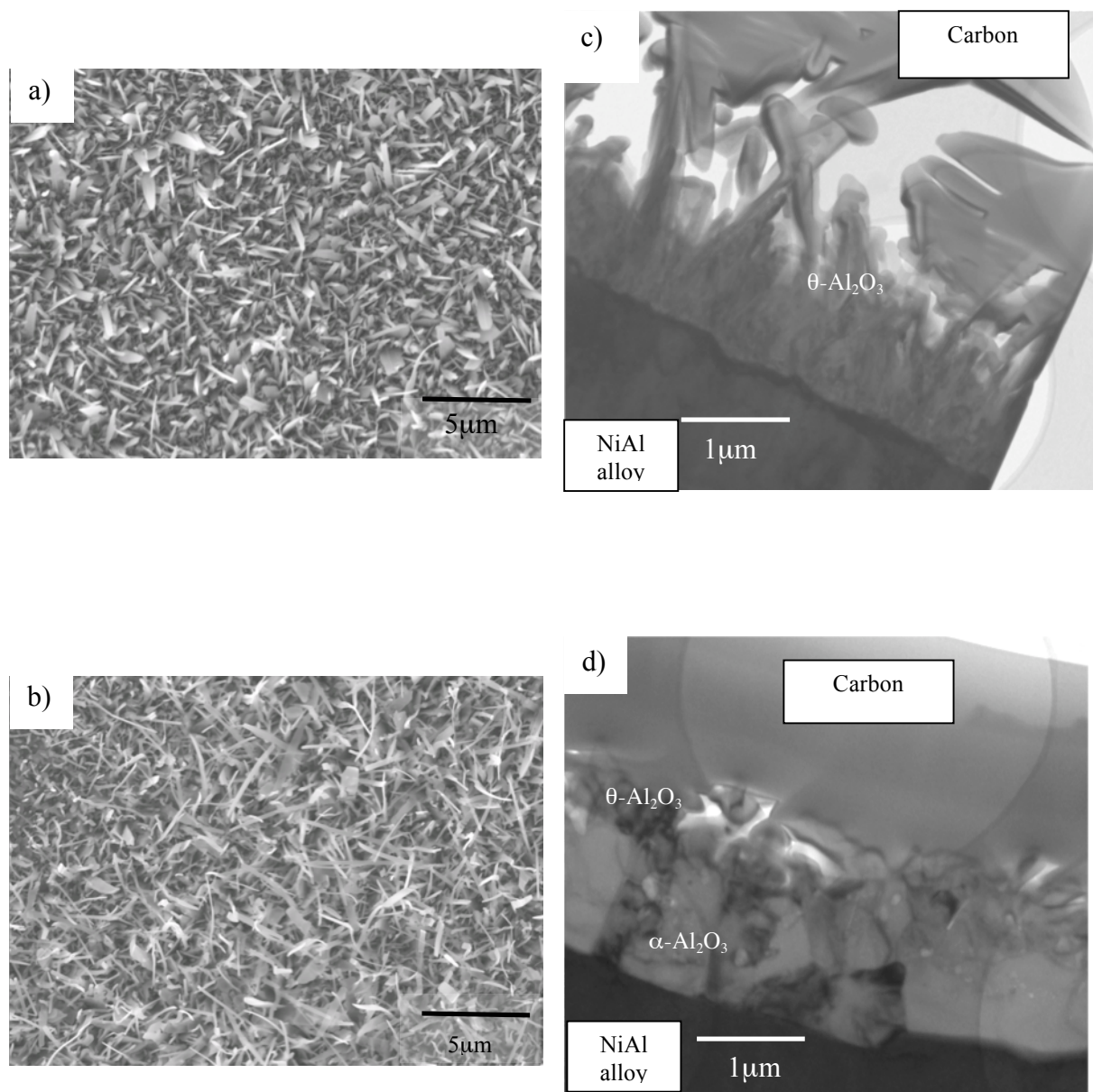


Figure 5.6 Surface SEM and cross-sectional TEM images of bare Ni50Al after oxidation tests for 1 h (a, c), and 100 h (b, d)

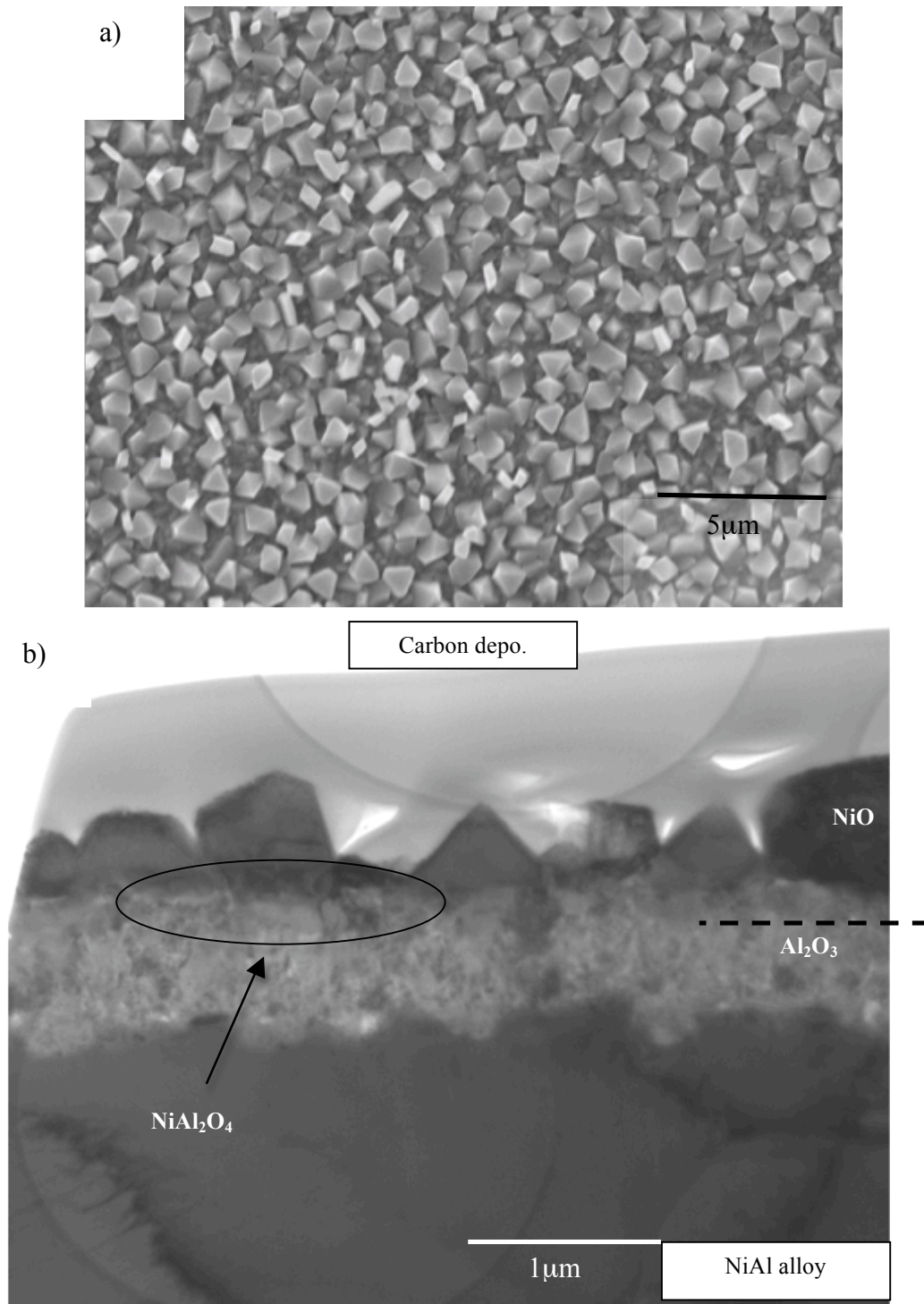


Figure 5.7.1 Surface SEM and cross-sectional TEM images of oxide scales formed on Ni50Al coated with Ni (Sample #1) layer after oxidation tests for 1 h at 1000 °C in air

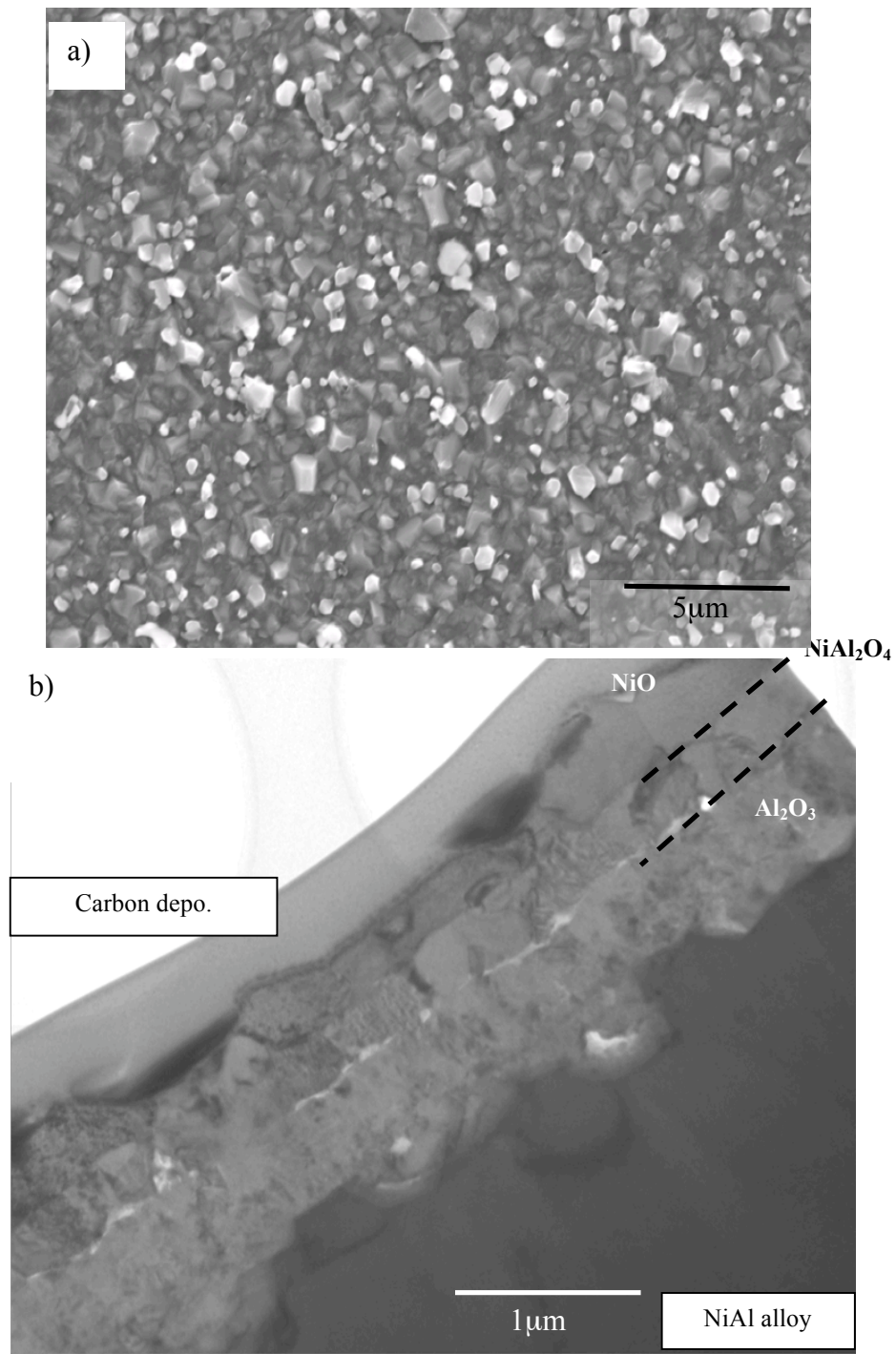


Figure 5.7.2 Surface SEM and cross-sectional TEM images of oxide scales formed on Ni50Al coated with Ni-3.1%Fe₂O₃ (Sample #2) layer after oxidation tests for 1 h at 1000 °C in air

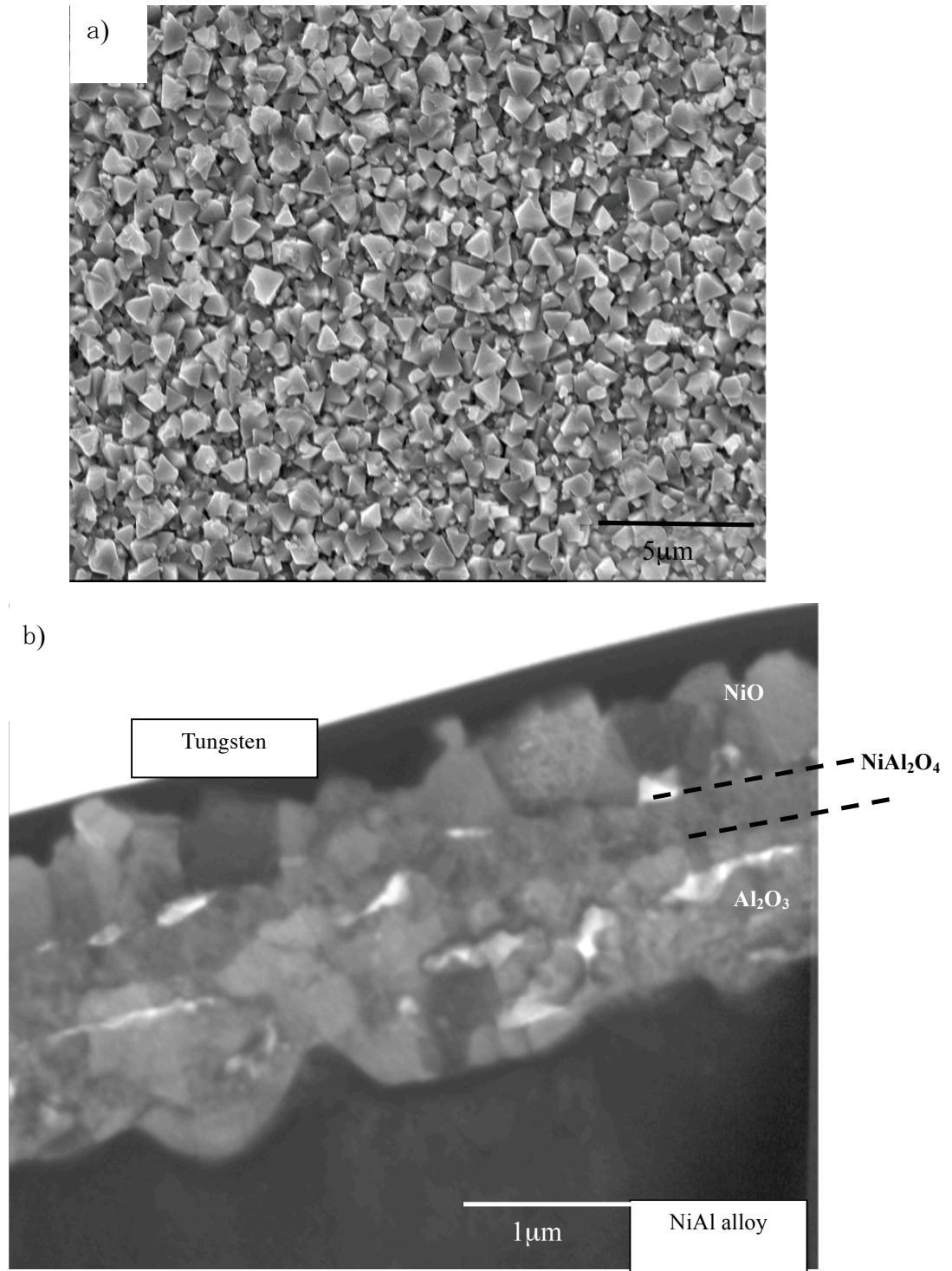


Figure 5.7.3 Surface SEM and cross-sectional TEM images of oxide scales formed on Ni50Al coated with 5.2%Fe₂O₃ (Sample #6) layer after oxidation tests for 1 h at 1000 °C in air

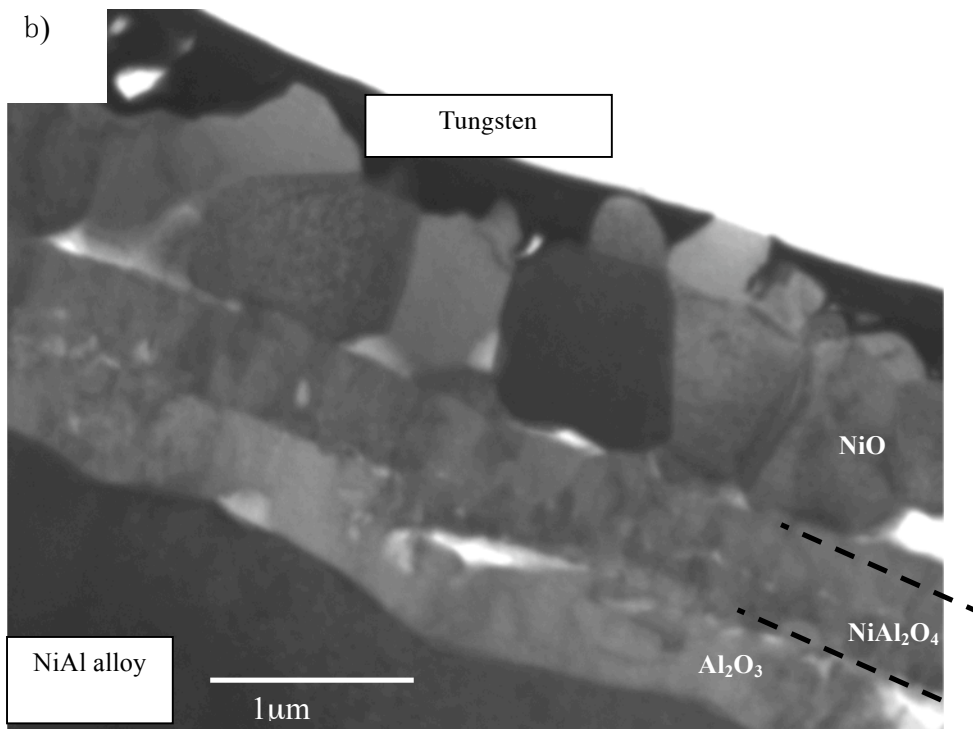
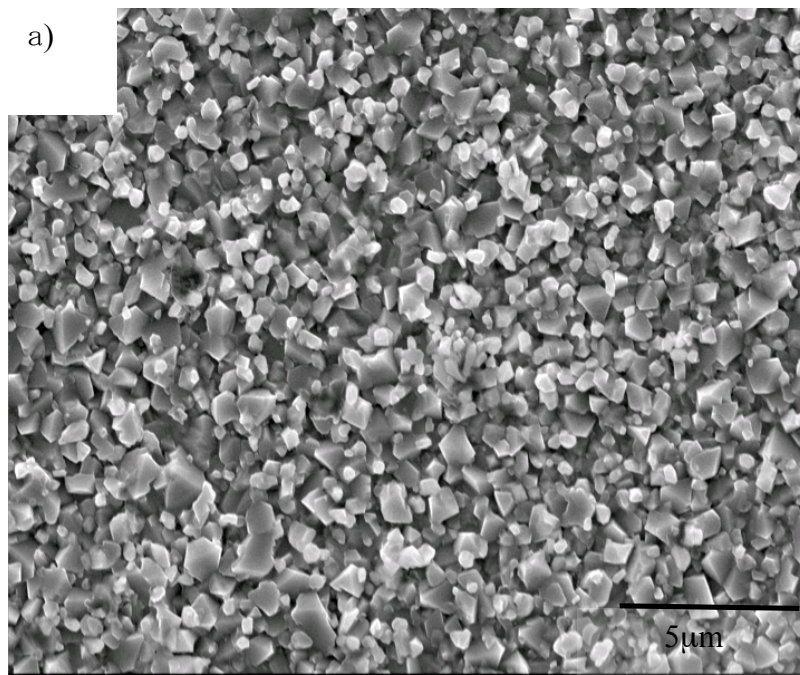


Figure 5.7.4 Surface SEM and cross-sectional TEM images of oxide scales formed on Ni50Al coated with Ni-7.4%Fe₂O₃ (Sample #7) layer after oxidation tests for 1 h at 1000 °C in air

The θ - Al_2O_3 was detected on the bare Ni50Al **Fig. 5.5(a)** and Ni-coated **Fig. 5.5(b)** samples at all t_{ox} . However, θ - Al_2O_3 was detected at $t_{\text{ox}} = 1$ h but not at $t_{\text{ox}} > 9$ h for the Ni-3.1% Fe_2O_3 composite-coated sample **Fig. 5.5(c)**. The absence of θ - Al_2O_3 peaks may be due to the consumption of θ - Al_2O_3 (process II) or an acceleration of the phase transformation (process III) of θ - Al_2O_3 to α - Al_2O_3 by co-existing α - Fe_2O_3 nano-powder in a Ni-coating layer. For the Ni-5.2% Fe_2O_3 **Fig. 5.5(d)** or Ni-7.4% Fe_2O_3 **Fig. 5.5(e)** samples, no θ - Al_2O_3 was detected but α - Al_2O_3 was detected even at $t_{\text{ox}} = 1$ h. On these samples containing more than 5% of Fe_2O_3 , α - Al_2O_3 could have been formed directly (process IV) or the transformation reaction may have been further accelerated (process III); Fe_2O_3 is an isomorph of a corundum structure as is α - Al_2O_3 and could provide heterogeneous nucleation sites for α - Al_2O_3 phase formation in the oxidation process.

In this study, thin Ni and Ni- Fe_2O_3 composites pre-coating layers electrodeposited on Ni50Al alloy and their effect on the phase structure and thickness of oxide scales were investigated and it was found that two factors dominate the effects: (process II) formation of NiAl_2O_4 , and (process III) rapid transformation of meta-stable Al_2O_3 to stable α - Al_2O_3 or (process IV) suppression of meta-stable Al_2O_3 formation by Fe_2O_3 . It was found that process II delays process III even at $t_{\text{ox}} = 100$ h. Incorporation of 3.1% Fe_2O_3 nano-powder into the Ni-coating layer resulted in an accelerating effect on process III at $t_{\text{ox}} = 1$ h. Further addition of Fe_2O_3 nano-powder, above 5%, to a Ni-coating layer was found to promote process IV. According to the results presented in this paper, it is evident that the incorporation of Fe_2O_3 nano-powder into a Ni-coating layer is a promising technique to improve the controllability of high-temperature oxidation of Al_2O_3 forming alloys.

5.4. Conclusions

The formation of thin Ni and Ni-Fe₂O₃ composite precoating layers by the PED technique on Ni50Al alloy in a Watts bath with or without Fe₂O₃ nano-powder and its effects on the oxidation products and Al₂O₃ scale formation were studied.

1. Ni precoating layers of different thicknesses (260 to 1270 nm) and with different contents of Fe₂O₃ nano-powder (3.1% to 7.4%) could be obtained by using the PED technique.
2. An Ni-coating layer did not suppress the formation of θ -Al₂O₃ phase, while an Ni3.1%Fe₂O₃-coating layer accelerated the transformation of θ -Al₂O₃ to α -Al₂O₃ phases. Further addition of Fe₂O₃ (5.2% and 7.4%) may completely suppress the formation of θ -Al₂O₃ phase or promote direct formation of α -Al₂O₃.
3. Two factors strongly affect the structure, composition, and thickness of the oxide scales: (i) formation of NiAl₂O₄ and (ii) the effect of Fe₂O₃ to accelerate the transformation of meta-stable Al₂O₃ to stable α -Al₂O₃ or to suppress the formation of meta-stable Al₂O₃.

5.5. References

1. Y. Cai, D. Taplin, M.J. Tan, W. Zhou, *Scr. Mater.* 41, 967(1999)
2. S.R. Allahkaram, M. Honarvar Nazari, S. Mamaghani, A. Zarebidaki, *Mater. Des.* 32, 750 (2011)
3. H. Zhao, L. Liu, Y. Wu, W.B. Hu, *Comput. Sci. Technol.* 67, 1210 (2007)
4. M. Stroumbouli, P. Gyftou, E.A. Pavlatou, N. Spyrellies, *Surf. Coat. Technol.* 195, 325 (2005)
5. Y. Zhou, H. Zhang, B. Qian, *Appl. Surf. Sci.* 253, 8335 (2007)

6. B.R. Tian, Y.F. Cheng, *Electrochim. Acta* 53, 511 (2007)
7. L. Chen, L.P. Wang, Z.X. Zeng, J.Y. Zhang, *Mater. Sci. Eng., A* 434, 319 (2006)
8. T.J. Tuaweri, G.D. Wilcox, *Surf. Coat. Technol.* 200, 5921 (2006)
9. T.V. Nguyen, H.C. Lee, M. Alam Khan, O.B. Yang, *Sol. Energy* 81, 529 (2007)
10. Espitia-Cabrera, H. Orozco-Hernández, R. Torres-Sánchez, M.E. Contreras-García, P. Bartolo-Pérez, L. Martínez, *Mater. Lett.* 58, 191 (2003)
11. X. Peng, *Oxid. Met.* 51, 291 (1999)
12. C.T.J. Low, R.G.A. Wills, F.C. Walsh, *Surf. Coat. Technol.* 201, 371 (2006)
13. Shujiang Geng, Shaojun Qi, Qicheng Zhao, Shenglong Zhu, Fuhui Wang, *Int. J. hydrogen energy* 37, 10850 (2012)
14. P. Ganesan, S.P. Kumaraguru, B.N. Popov, *Surf. Coat. Technol.* 201, 3658 (2006)
15. W.H. Lee, S.C. Tang, K.C. Chung, *Surf. Coat. Technol.* 120–121, 607 (1999)
16. B. Tury, G.Z. Radnoczi, G. Radnoczi, M.L. Varsanyi, *Surf. Coat. Technol.* 331, 202 (2007)
17. Z.J. Huang, D.S. Xiong, *Surf. Coat. Technol.* 202, 3208 (2008)
18. S.K. Ghosh, A.K. Grover, G.K. Dey, M.K. Totlani, *Surf. Coat. Technol.* 126, 48 (2000)
19. C.R. Tomachuk, *Surf. Coat. Technol.* 122, 6 (1999)
20. Y.H. Song, G. Wei, R.C. Xiong, *Trans. Nonferrous Met. Soc. China* 17, 363 (2007)
21. S.O. Pagotto Jr., *Surf. Coat. Technol.* 122, 10 (1999)
22. P. Gyftou, E.A. Pavlatou, N. Spyrellis, *Appl. Surf. Sci.* 254, 5910 (2008)
23. A.F. Zimmerman, D.G. Clark, K.T. Aust, U. Erb, *Mater. Lett.* 52, 85 (2002)
24. A. Zoikis-Karathanasis, E.A. Pavlatou, N. Spyrellis, *J. Alloys Compd.* 494, 396 (2010)
25. Li Chen, Liping Wang, Zhixiang Zeng, Xu. Tao, *Surf. Coat. Technol.* 201, 599 (2006)
26. Venu Mangam, Sumit Bhattacharya, Karabi Das, Siddhartha Das, *Surf. Coat. Technol.* 205, 801 (2010)
27. S.A. Lajevardi, T. Shahrabi, *Appl. Surf. Sci.* 256, 6775 (2010)
28. H. J. Grabke, *Intermetallics* 7, 1153–1158 (1999)
29. G. C. Rybicki and J. L. Smialek, *Oxidation of Metals* 31, 275–304 (1989)
30. L. B. Pfeil, U.K. Patent no 459848, (1937)

31. L. B. Pfeil, U.K. Patent no 574088, (1945)
32. M. W. Brumm and H. J. Grabke, *Corrosion Science* 33, 1677–1690 (1992)
33. Z. Liu and W. Gao, *Oxid. Met.* 54, 189 (2000)
34. H. El Kadiri, R. Molins, Y. Bienvenu and M. F. Horstemeyer, *Oxid. Met.* 64, 63 (2005)
35. F. Liu, H. Gotlind, J. E. Svensson, L. G. Johansson and M. Halvarsson, *Corr. Sci.* 50, 2272–2281 (2008)
36. H. Josefsson, F. Liu, J. E. Svensson, M. Halvarsson and L. G. Johansson, *Mat. Corr.* 56, 801 (2005)
37. Y. Kitajima, S. Hayashi, T. Nishimoto, T. Narita and S. Ukai, *Oxid. Met.* 73, 375 (2010)
38. Y. Kitajima, S. Hayashi, T. Nishimoto, T. Narita and S. Ukai, *Oxid. Met.* 75, 41 (2011)
39. A. Shaaban, S. Hayashi, K. Azumi, *Oxid. Met.* 82, 85 (2014)
40. J.J. Kelly, P.E. Braddey, D. Landolt, *J. Electrochem.* 147, 2975 (2000)
41. J.W. Dini: *Electrodeposition: The Material Science of Coatings and Substrates*, Noyes Publications, New Jersey, 141, 1993
42. J.W. Dini: *Plat. Surf. Finish.*, 75, 11 (1988)
43. H. Natter and R. Hempelmann: *Electrochim. Acta.*, 49, 51 (2003)
44. J. Vazquez-Arenas, R. Cruz and L.H. Mendoza- Huizar: *Electrochim. Acta*, 52, 892 (2006)
45. J. Doychak, J.L. Smialek, T.E. Mitchell, *Metall. Trans. A* 20, 499 (1989)
46. P. van Manen, E.W.A. Young, D. Schalkoord, C.J. van der Wekken, J.H.W. de Wit, *Surf. Interface Anal.* 12, 391 (1988)
47. R. Haugsrud, *Corr. Sci.* 45, 211 (2003)
48. S. C. Choi, H. J. Cho, Y. J. Kim, and D. B. Lee, *Oxid. Met.* 46, 51 – 72 (1996).

Chapter 6

EFFECTS OF Ni-Fe CO-DEPOSITED LAYER ON DIRECT α -Al₂O₃ FORMATION

In chapter five, the formation of thin Ni and Ni-Fe₂O₃ composite precoating layers by the PED technique on Ni50Al alloy in a Watts bath with or without Fe₂O₃ nano-powder and its effects on the oxidation products and Al₂O₃ scale formation were studied. An Ni-coating layer did not suppress the formation of θ -Al₂O₃ phase, while an Ni3.1%Fe₂O₃-coating layer accelerated the transformation of θ -Al₂O₃ to α -Al₂O₃ phases. Further addition of Fe₂O₃ (5.2% and 7.4%) may completely suppress the formation of θ -Al₂O₃ phase or promote direct formation of α -Al₂O₃. Two factors strongly affect the structure, composition, and thickness of the oxide scales: (i) formation of NiAl₂O₄ and (ii) the effect of Fe₂O₃ to accelerate the transformation of meta-stable Al₂O₃ to stable α -Al₂O₃ or to suppress the formation of meta-stable Al₂O₃. According to the results presented in the previous section, it is evident that the incorporation of Fe₂O₃ nano-powder into a Ni precoating layer is a promising technique to improve the controllability of high-temperature oxidation of Al₂O₃ forming alloys.

But due to the limitation of introducing Fe₂O₃ nano powder in Ni-coating layer as a composite up to max (7.4%), Effects of Ni-Fe co-deposits on direct α -Al₂O₃ formation with changing Fe/Ni ratio will be studied.

Abstract

Effects of Ni, Fe metal or Ni-Fe alloy deposits on the oxidation behavior and oxidation products of Ni50Al alloy at 1000°C in air atmosphere were studied. The surface morphologies of the deposited layers and/or oxide scale were examined by using field emission scanning electron microscope (FE-SEM) and transmission electron microscopy (TEM). The chemical composition of the deposited layers were determined before and after oxidation by using energy dispersive X-ray (EDX). The deposited layer and the resultant oxidation products were identified by using X-ray diffractometer (XRD). The morphology of deposits was found to depend on the deposited Fe/Ni ratio consequently; it affected the final oxidation products. θ -Al₂O₃ was detected for bare, Ni-coated and Ni17%Fe-coated Ni50Al alloy samples. θ -Al₂O₃ phases were not detected for Fe-coated and Ni72%Fe-coated samples at all oxidation times, but the oxidation mass gain after 100 h on Fe-coated and Ni72%Fe-coated samples were the highest among the coated samples. Cross-sectional images revealed that the grain size of α -Al₂O₃ on both Fe-coated and Ni72%Fe-coated samples were the smallest among the coated samples. XRD and EDX point analysis confirmed the formation of different multilayered structure oxide scales on different oxidized samples. NiO/NiAl₂O₄/Al₂O₃ on Ni-coated, complex spinel Ni(Fe)Al₂O₄/Al₂O₃ on Ni17%Fe-coated, Fe₂O₃/ (Fe, Al)₂O₃/ α -Al₂O₃ on Ni72%Fe-coated and Fe₂O₃/ α -Al₂O₃ on Fe-coated samples. Introducing Fe or Ni72%Fe precoating layer prior to the oxidation of Ni50Al alloy resulted in suppression of θ -Al₂O₃ formation and influenced the microstructure of α -Al₂O₃, which reflected on oxide scale growth rate.

Keywords:

Ni50Al alloy; α -Al₂O₃; oxidation; co-deposition; oxide scale; spinel oxide

6.1. Introduction

The promotion of oxidation resistance of highly Al-content alumina-forming alloys by the stable Al₂O₃ scale arises from slowing the diffusion kinetics of both oxygen and Al. Al₂O₃ scales of mixed phases have been found to form on these alloys, such as meta-stable γ -Al₂O₃, δ -Al₂O₃, and θ -Al₂O₃ and stable α -Al₂O₃ phases. α -Al₂O₃ is a good protective oxide scale because of its thermodynamic stability and slow growth rate [1, 2]. However, at lower temperatures and/or in the early stages of oxidation of Al₂O₃-forming alloys, the meta-stable oxide phases usually grow simultaneously with α -Al₂O₃ until the complete transformation into stable α -Al₂O₃ occurs. The growth rate of these meta-stable oxide phases is about two orders of magnitude higher than that of α -Al₂O₃ [2-4]. Therefore, direct formation of α -Al₂O₃ is required to improve the reliability and lifetime of Al₂O₃-forming alloys and coatings.

In a previous study by Kitajima *et al.*, it was found that the Cr or Fe precoating suppress formation of θ -Al₂O₃ at 900 °C by oxidation in air, but Ni was found to delay the transformation [5]. The rapid formation of α -Al₂O₃ is attributed to the formation of coated metal oxides, Cr₂O₃ and Fe₂O₃, which have an isomorphous corundum structure with α -Al₂O₃ [5]. These metal oxides may provide a higher density of nucleation sites for α -Al₂O₃. Also, the effect of the transformation on the long-term growth rate of Al₂O₃ scales, which formed on β -Ni-50Al at 1000 °C in air without meta-stable Al₂O₃ by Fe or Cr precoating, has been examined in Ref. [6]. These metallic precoatings were found to

affect the size of α -Al₂O₃ grains, which in turn affected the growth kinetics of α -Al₂O₃. The α -Al₂O₃ scale that transformed earlier always consisted of smaller grains, whereas the size of grains increased with delay in θ -Al₂O₃ to α -Al₂O₃ transformation. The coexistence of Fe-oxide (Fe₂O₃) may act as nucleation sites for α -Al₂O₃ phase formation and resulted in small grain size of α -Al₂O₃ while, Ni-coating was found to delay the transformation to α -Al₂O₃ and resulted in large grain size of α -Al₂O₃. Although the introducing of Ni-coating that resulted in largest grain size of α -Al₂O₃ could slow the growth rate of the oxide scale, there is still a need for rapid $\theta \rightarrow \alpha$ -Al₂O₃ phase transformation, which could be accomplished by impeding heterogeneous nucleation sites for α -Al₂O₃ inside Ni-coating as It was discussed in the previous work [7]. An Ni-coating layer did not suppress the formation of θ -Al₂O₃ phase, while an Ni3.1%Fe₂O₃-coating layer accelerated the transformation of θ -Al₂O₃ to α -Al₂O₃ phases. Further addition of Fe₂O₃ (5.2% and 7.4%) may completely suppress the formation of θ -Al₂O₃ phase or promote direct formation of α -Al₂O₃. Two factors strongly affect the structure, composition, and thickness of the oxide scales: (i) formation of NiAl₂O₄ and (ii) the effect of Fe₂O₃ to accelerate the transformation of metastable Al₂O₃ to stable α -Al₂O₃ or to suppress the formation of metastable Al₂O₃. At the moment this technique showed a limitation of introducing more than 7.4% Fe₂O₃ nano powder in Ni-coating as a composite precoating layer. However there is a possibility to deposit Ni-Fe alloy precoating on Ni50Al alloy to evaluate the effect of Fe/Ni ratio on the oxidation products and growth kinetics of Al₂O₃ scale at 1000 °C in air. Co-electrodeposition of Ni and Fe as an alloy is considered to be an anomalous co-deposition because of their different deposition rates [8-12]. Grimmitt *et al.* have reported that the properties of the Ni-Fe alloy deposits may be affected by different current waveforms [13]. It was also reported

that PED is more effective than direct current (DC) electrodeposition for controlling and improving the coating properties such as particle distribution, structure, grain size, hardness and wear resistance [14-22]. Ni-Fe alloy coating will be deposited on Ni50Al alloy via pulsed electrodeposition (PED) as a surface modification technique prior to the oxidation test at 1000°C in air atmosphere.

6.2. Materials and methods

An Ni50Al alloy ingot was prepared from Al and Ni metals (~99.99% in purity) by the Ar-arc melting technique followed by homogenization at 1200 °C for 48 h in vacuum (5×10^{-3} Pa) and was cut into specimens of *ca.* 1 mm in thickness. These specimens were ground with SiC paper (80, 280, 500, 800, 1000, 1500, 2400 and 4000 grit) and finished with 3 μ m diamond paste to obtain a mirror finish surface and then ultrasonically degreased in acetone for 10 min. Ni or Ni-Fe precoating layer was electrodeposited on the Ni50Al sample from a Ni-bath containing 15.5 g dm⁻³ NiSO₄•6H₂O as a source of Ni, (0, 1.4 or 27.8) g dm⁻³ FeSO₄•7H₂O as a source of Fe, (50 or 35) g dm⁻³ Na₂SO₄ and 12.5 g dm⁻³ H₃BO₃ as a buffer. Fe precoating was electrodeposited on the Ni50Al sample from a Fe-bath containing 27.8 g dm⁻³ FeSO₄•7H₂O as a source of Fe, 35 g dm⁻³ Na₂SO₄ and 12.5 g dm⁻³ H₃BO₃ as a buffer. The solution acidity was adjusted by 0.1 M H₂SO₄ at pH 3. The electrodeposition process was conducted at deposition current of -10 mA.cm⁻² for 600 sec with solution agitation at 400 rpm by using a potentiostat (Ivium Technologies Co., model Iviumstat) and an electrochemical cell composed of Ag/AgCl reference electrode, Ni sheet counter electrode and Ni50Al (about 2 cm² in area) sample working electrode. After electrodeposition, these samples were subjected to high-temperature oxidation tests.

Samples were placed in a furnace exposed to air, and the temperature was elevated at a rate of $10\text{ }^{\circ}\text{C min}^{-1}$ to $1000\text{ }^{\circ}\text{C}$ and kept for $t_{\text{ox}} = 0.5, 1, 4, 7, 9, 25, 49$ and 100 h and then cooled down to room temperature. Weight of samples were measured before and after the oxidation tests to obtain oxidation mass gain.

Surface morphologies and chemical compositions of different PED precoating layers were observed by FE-SEM with EDX (JEOL Co., model 6500F). Phase analysis of these precoating layers was conducted by using X-ray diffractometer XRD (JEOL Co., model JDX 3500, operated at 20 mA and 40 kV with $\text{CuK}\alpha$ radiation). TEM (JEOL Co., model JEM 2000FX, operated at 200 kV), multi-beam FIB-SEM (JEOL Co., model JIB-4600F/HDK) was used for observation of surface morphologies and cross-sections, determination of the concentrations of Al, Ni, Fe and O in oxide scales, and identification of oxidation products. For cross-sectional observation of oxide scales by using TEM, a carbon layer or a tungsten layer was pre-deposited on the sample to protect the surface from Ga^+ milling, and then a cross-section was lifted out and attached to a Mo support grid that fits into a specimen holder.

6. 3. Results and Discussion

6.3.1. Properties of co-electrodeposited Ni, Ni-Fe and Fe precoating layers

The current waveform of PED was defined by the polarization time (t_{on}), resting time (t_{off}) and polarization (deposition) current density (i_{cd}). **Fig. 6.1** shows the current waveform and potential response at the initial stage of PED form Ni-bath containing (0, 1.4 or 27.8) g dm^{-3} $\text{FeSO}_4 \cdot 7\text{H}_2\text{O}$ or Fe-bath containing 27.8 g dm^{-3} $\text{FeSO}_4 \cdot 7\text{H}_2\text{O}$. The potential transient shows a decrease in the overpotential during t_{on} due to an increase in the surface area of deposits and relaxation of the depletion layer of Ni^{2+} or Fe^{2+} ions

during t_{off} . When i_{cd} is applied the value of response potential is suddenly dropped to a less noble value for all samples. This value increased after t_{off} is applied and it shifted to a nobler value. During the recovery time t_{off} the profile of the potential response of PED from Ni-bath including (0 or 1.4) g dm^{-3} $\text{FeSO}_4 \cdot 7\text{H}_2\text{O}$ is different from those from Ni-bath including 27.8 g dm^{-3} $\text{FeSO}_4 \cdot 7\text{H}_2\text{O}$ and Fe-bath containing 27.8 g dm^{-3} $\text{FeSO}_4 \cdot 7\text{H}_2\text{O}$. This difference in appearance of the potential response during t_{off} is attributed to the oxidation of Fe^{+2} in baths of high $\text{FeSO}_4 \cdot 7\text{H}_2\text{O}$ concentrations PED.

Ni-Fe alloy co-deposition is one of the most famous anomalous co-deposition alloys. Various mechanisms have been reported for anomalous co-deposition of Ni-Fe alloys. Mechanisms of anomalous deposition of Ni-Fe alloys and metal hydroxide formation were reported in ref. [8-9, 23] and confirmed by direct measurements in ref. [24-26]. Hydroxide suppression mechanism by Dahms *et al.* in which the nobler (Ni) deposition was suppressed by the formation of less noble hydroxide ($\text{Fe}(\text{OH})_2$) during electrodeposition process. $\text{Fe}(\text{OH})_2$ formation is preferentially occurs in the cathode layer and adsorbed on the cathode [8, 9]. Hessami *et al.* reported another mathematical model in which they focused on the difference in the dissociation or hydrolysis constants between intermediate compounds FeOH^+ and NiOH^+ [23].

The electrochemical reactions of Ni and Fe at the surface of the electrode (cathode) are given as



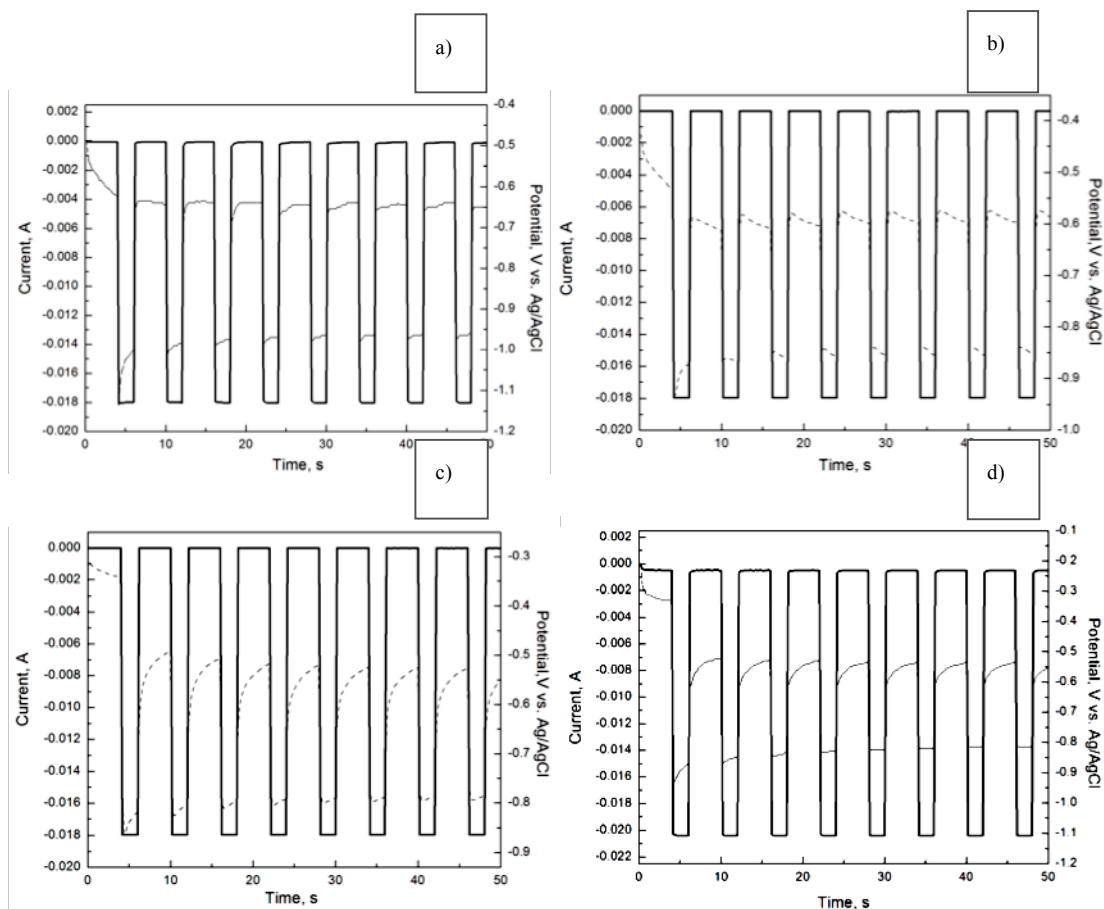


Figure 6.1. Current waveform for galvanostatic PED and potential response measured for electrodeposition from Ni-bath containing $15.5 \text{ g dm}^{-3} \text{ NiSO}_4 \cdot 6\text{H}_2\text{O}$ (a), Ni-bath containing $15.5 \text{ g dm}^{-3} \text{ NiSO}_4 \cdot 6\text{H}_2\text{O}$, $1.4 \text{ g dm}^{-3} \text{ FeSO}_4 \cdot 7\text{H}_2\text{O}$ (b), Ni-bath containing $15.5 \text{ g dm}^{-3} \text{ NiSO}_4 \cdot 6\text{H}_2\text{O}$, $27.8 \text{ g dm}^{-3} \text{ FeSO}_4 \cdot 7\text{H}_2\text{O}$ (c) and Fe-bath containing $27.8 \text{ g dm}^{-3} \text{ FeSO}_4 \cdot 7\text{H}_2\text{O}$ (d) on Ni50Al samples at $i_{\text{cd}} = -10 \text{ mA cm}^{-2}$, $t_{\text{on}} = 2 \text{ s}$, $t_{\text{off}} = 4 \text{ s}$ and $T = 25 \text{ }^\circ\text{C}$, pH 3, for 600 sec with solution agitation at 400 rpm.

The homogeneous equilibrium reactions of Ni and Fe in the electrodeposition system are given as



According to these equations and based on the dissociation mechanism, Ni(OH)^+ (4.5×10^{-5}) has three order of magnitude higher dissociation constant than Fe(OH)^+ (5.8×10^{-8}) in the cathode layer. Fe(OH)^+ is preferentially formed at the expense of Ni(OH)^+ , resulting in preferential deposition of Fe to Ni.

EDX analysis of the surface of PED coated samples from Ni-bath containing (1.4 or 27.8) g dm⁻³ FeSO₄•7H₂O showed Fe content of 17 wt.% and 72 wt.%, respectively. EDX analysis, which was taken from localized innermost and outermost areas of the cross sections of the precoating layers showed a variation in Fe concentrations. This variation could be represented as 85.4/55.7 wt. % Fe on Ni72 wt.% Fe and 19.6/3.9 wt. % Fe on Ni17 wt.% Fe. Formation of compact, dense and crack-free PED precoatings with different microstructures on the Ni50Al substrate was confirmed as shown in **Fig. 6.2**. Ni-coating is consisted of small facet-structured particles, Ni17 wt.% Fe coating is fine nodular-structured, Ni72 wt.% Fe precoating is fine fluffy-structured and Fe precoating is consisted of coarse tetrahedral-structured particles. Average particle sizes of PED precoating layers were in the order of Fe > Ni > Ni72 wt.% Fe > Ni17 wt.% Fe. The particle sizes of Ni-Fe co-deposited precoating layers shown in **Fig. 6.2.2** and **6.2.3** were smaller than those of Ni and Fe precoating layers shown in **Fig. 6.2.1** and **6.2.4**, which were deposited at the same PED condition. The reduction in the particle size and the thinning of the Ni-Fe alloy precoating layers than those of Ni and Fe precoating layers could be attributed to the anomalous co-deposition of Ni-Fe alloy.

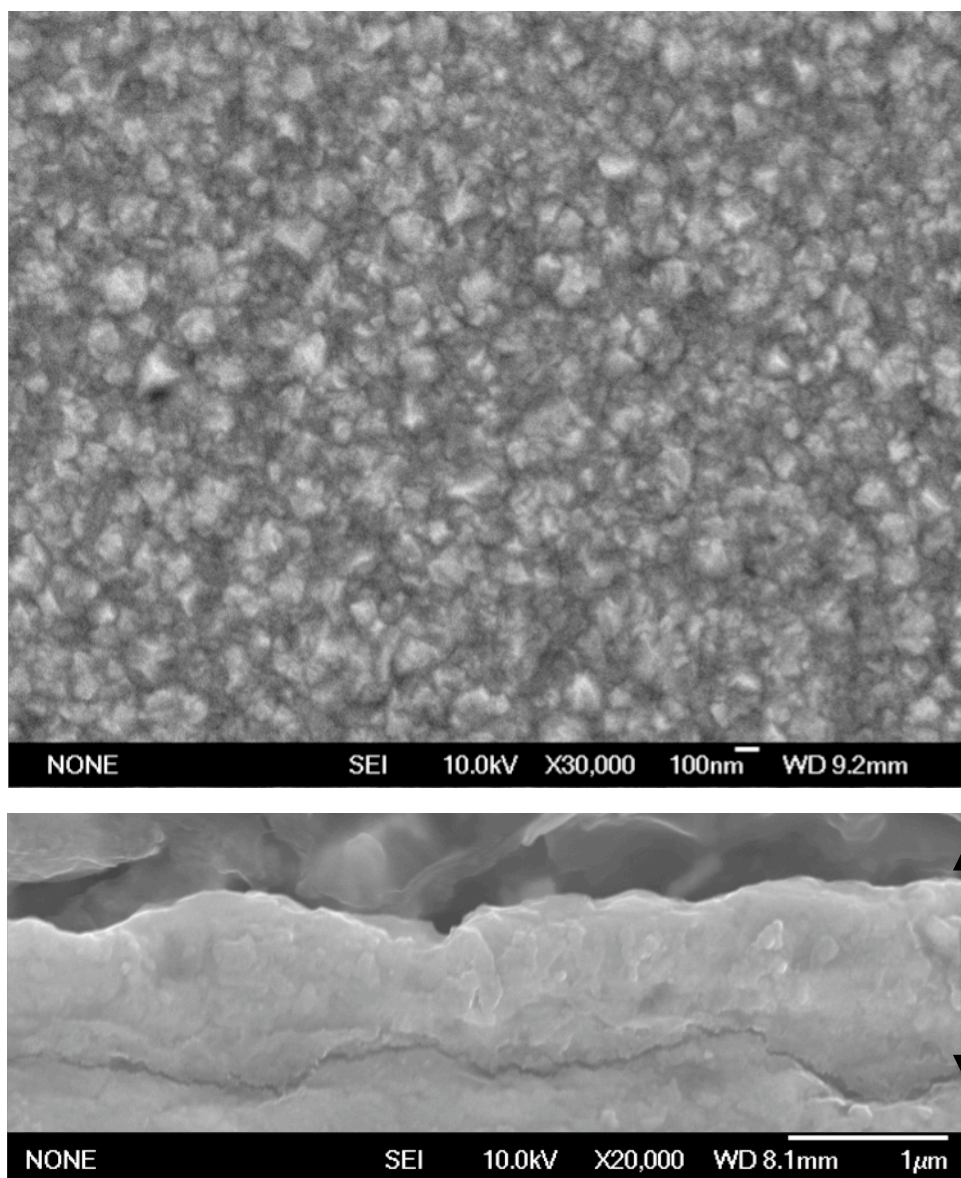


Figure 6.2.1: Surface and cross-sectional morphologies FE-SEM images of Ni on an Ni50Al samples, which was deposited for 600 s with pulse conditions at $i_{cd} = -10 \text{ mA}$

cm^{-2} , $t_{on} = 2 \text{ s}$, $t_{off} = 4 \text{ s}$ and $T = 25 \text{ }^\circ\text{C}$

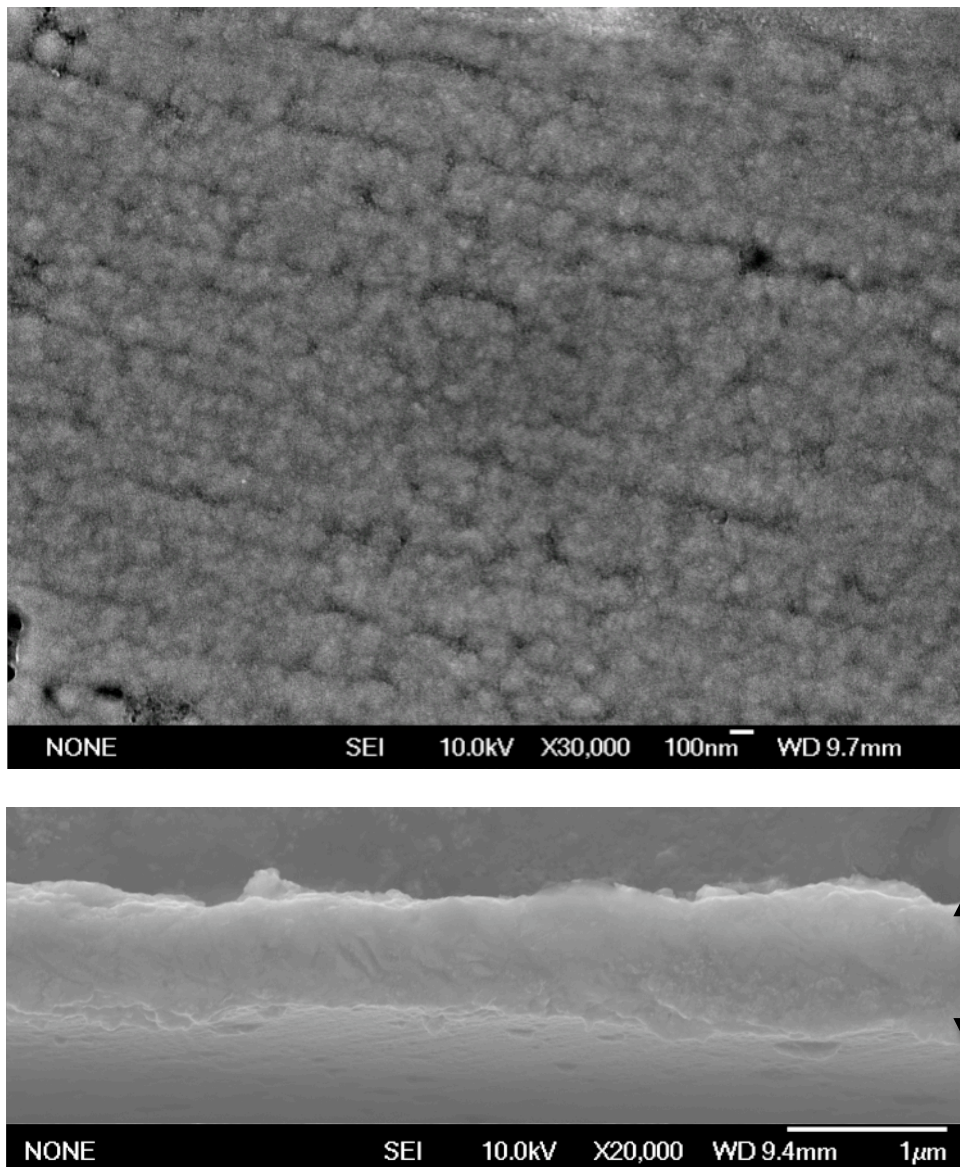


Figure 6.2.2: Surface and cross-sectional morphologies FE-SEM images of Ni17 wt. %Fe, on an Ni50Al samples, which was deposited for 600 s with pulse conditions at $i_{cd} = -10 \text{ mA cm}^{-2}$, $t_{on} = 2 \text{ s}$, $t_{off} = 4 \text{ s}$ and $T = 25 \text{ }^\circ\text{C}$

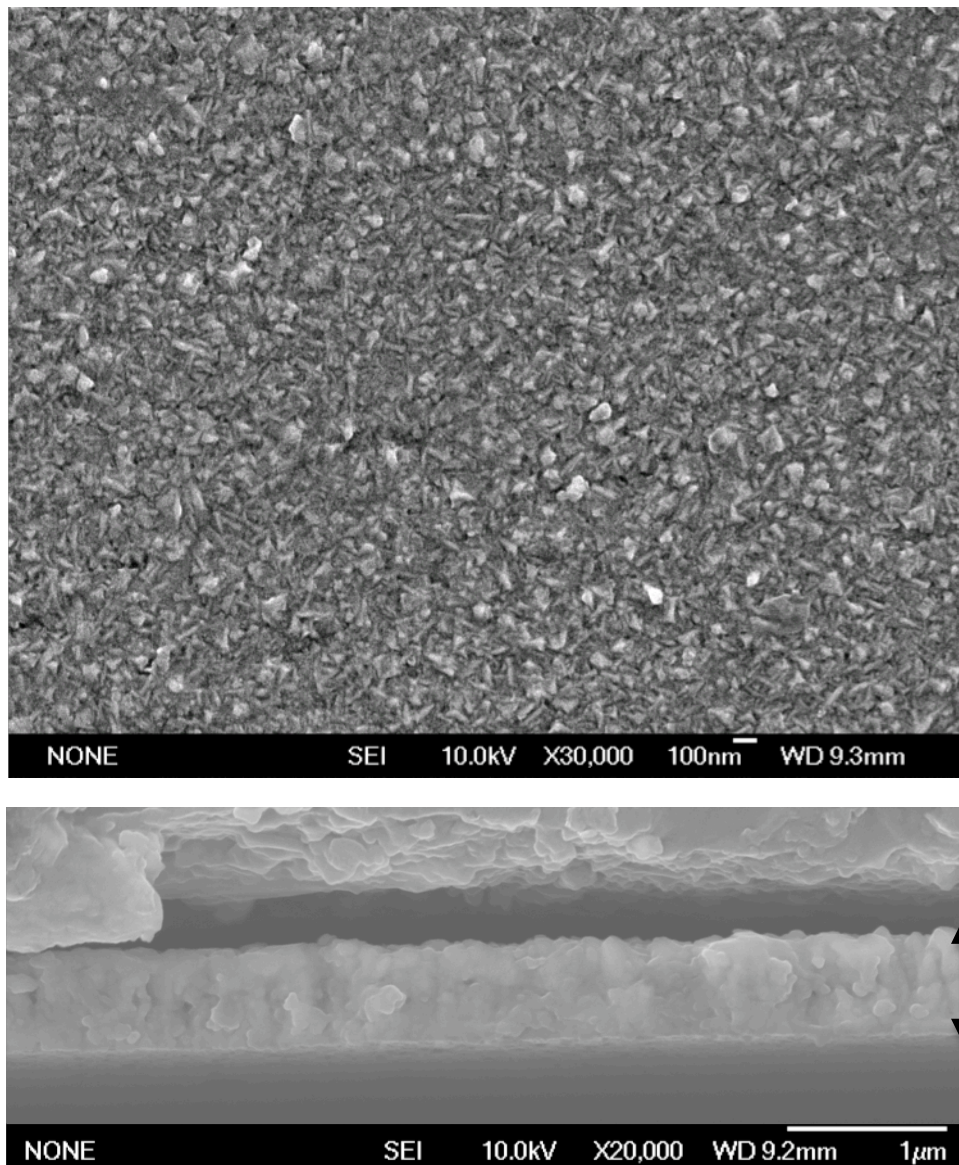


Figure 6.2.3: Surface and cross-sectional morphologies FE-SEM images of Ni72 wt. %Fe on an Ni50Al samples, which was deposited for 600 s with pulse conditions at $i_{cd} = -10 \text{ mA cm}^{-2}$, $t_{on} = 2 \text{ s}$, $t_{off} = 4 \text{ s}$ and $T = 25 \text{ }^\circ\text{C}$

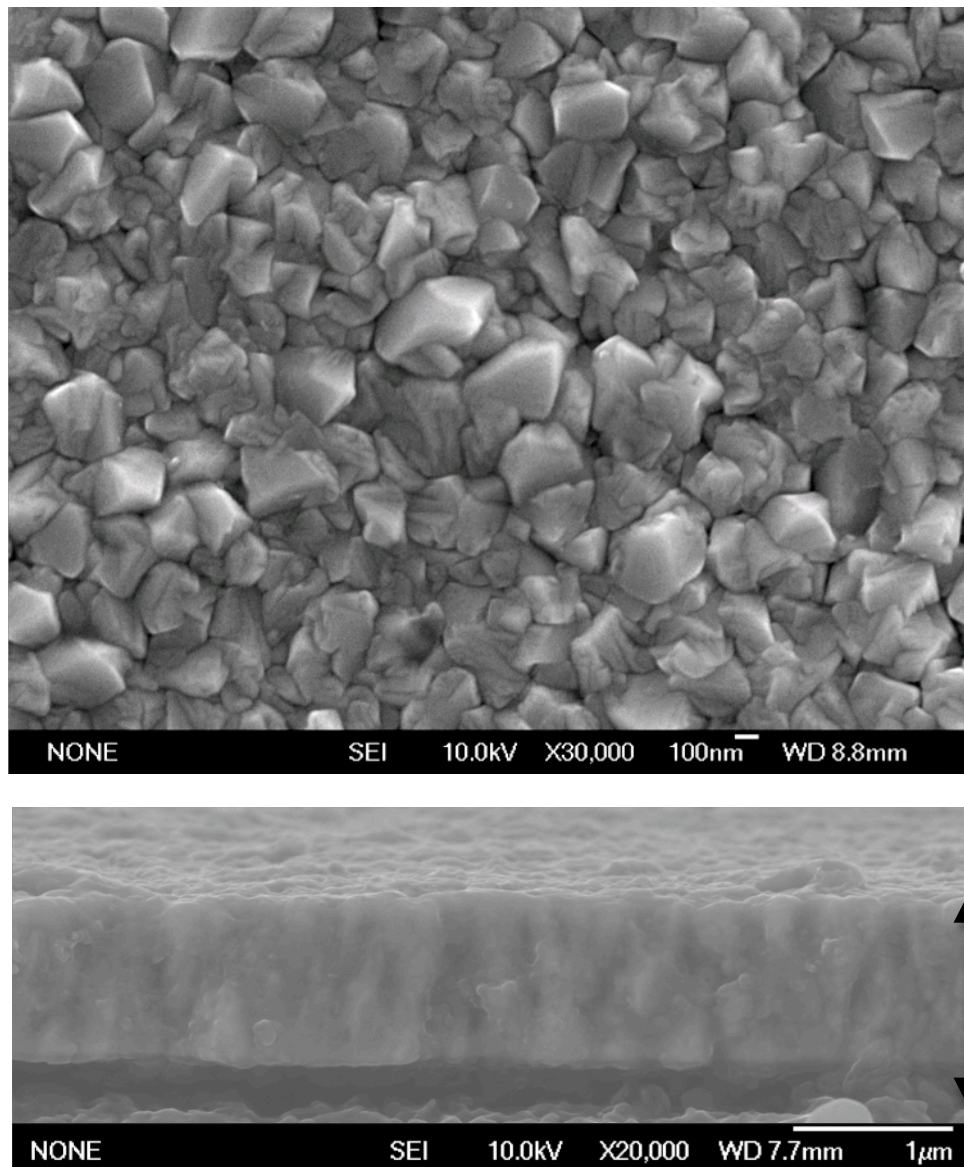


Figure 6.2.4: Surface and cross-sectional morphologies FE-SEM images of Fe on an Ni50Al samples, which was deposited for 600 s with pulse conditions at $i_{cd} = -10 \text{ mA cm}^{-2}$, $t_{on} = 2 \text{ s}$, $t_{off} = 4 \text{ s}$ and $T = 25 \text{ }^\circ\text{C}$

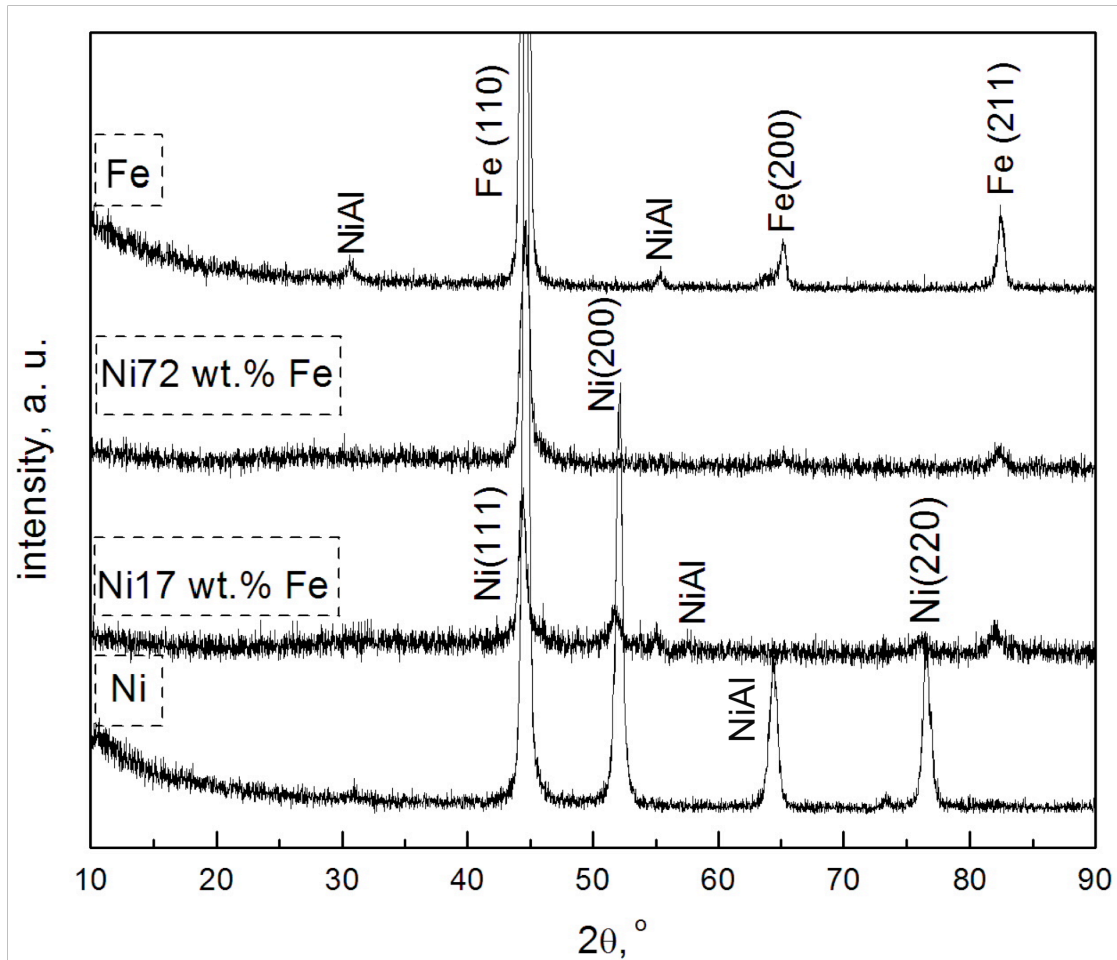


Figure 6.3: XRD patterns of Ni-, Ni17 wt. %Fe-, Ni72 wt. %Fe- and Fe-coated Ni50Al samples, which were deposited for 600 s with pulse conditions at $i_{cd} = -10 \text{ mA cm}^{-2}$, $t_{on} = 2 \text{ s}$, $t_{off} = 4 \text{ s}$ and $T = 25 \text{ }^\circ\text{C}$

Fig. 6.3 shows the XRD patterns of the as-deposited samples. Ni-coating showed three strong peaks of Ni fcc structure (111), (200) and (220) and the growth seems to be oriented at (111) plane reflection. In case of low Fe content alloy (Ni17 wt.% Fe), the deposited alloy still exhibits a (111) growth orientation, but the intensities of other peaks were decreased and shifted to a lower $2\theta^\circ$. The intensities of the (200) and (220) peaks further decrease with increasing Fe content and disappear from high Fe content alloy (Ni72 wt.% Fe) and the deposited alloy transformed to exhibit a (110) growth orientation of Fe bcc structure.

6.3.2. High temperature oxidation tests of NiAl alloy coated with PED Ni, Ni-Fe and Fe precoating layers

Bare Ni50Al alloy, Ni50Al alloys coated with Ni, Ni17Fe alloy, Ni72Fe alloy and Fe precoating layers were subjected to high temperature oxidation tests at 1000 °C in air. Oxidation mass gain (Δm) was obtained from weight change after the isothermal oxidation for $t_{\text{ox}} = 0.5, 1, 4, 7, 9, 25, 49$ and 100 h as shown in **Fig. 6.4**. The oxidation kinetics of all samples seems to follow the parabolic law. Two stages of oxidation were observed, initial stage of oxidation with a rapid growth rate ($t_{\text{ox}} = 0.5 \rightarrow 25$) followed by a steady state of oxidation with a very slow growth rate ($t_{\text{ox}} = 25 \rightarrow 100$). Because of the oxidation of these precoating layers, the formation of fast growing NiO on Ni-coated and Ni17Fe-coated samples or Fe_3O_4 and Fe_2O_3 on Ni72Fe-coated and Fe-coated samples reflected in higher oxidation mass gain and faster growth rate than the bare Ni50Al alloy. The oxidation mass gains on the coated samples were in the order of Fe-coated > Ni72Fe-coated > Ni17Fe-coated > Ni-coated Ni50Al alloy.

Fig. 6.5 shows the surface morphologies of the samples oxidized at 1000 °C for 9 h. An oxide scale of blade-like morphology covered the surface of the Ni50Al bare alloy as shown in **Fig. 6.5a**. Such morphology is typically observed for transient phases of alumina such as $\theta\text{-Al}_2\text{O}_3$ [6-7, 27-30]. An oxide scale of faceted morphology covered the Ni-coated sample as shown in **Fig. 6.5b**. Mixture of faceted and tetrahedral morphologies covered the Ni-Fe-coated samples as shown in **Fig. 6.5c** and **6.5d**. A tetrahedral-shaped oxide covered the Fe-coated sample as shown in **Fig. 6.5e**.

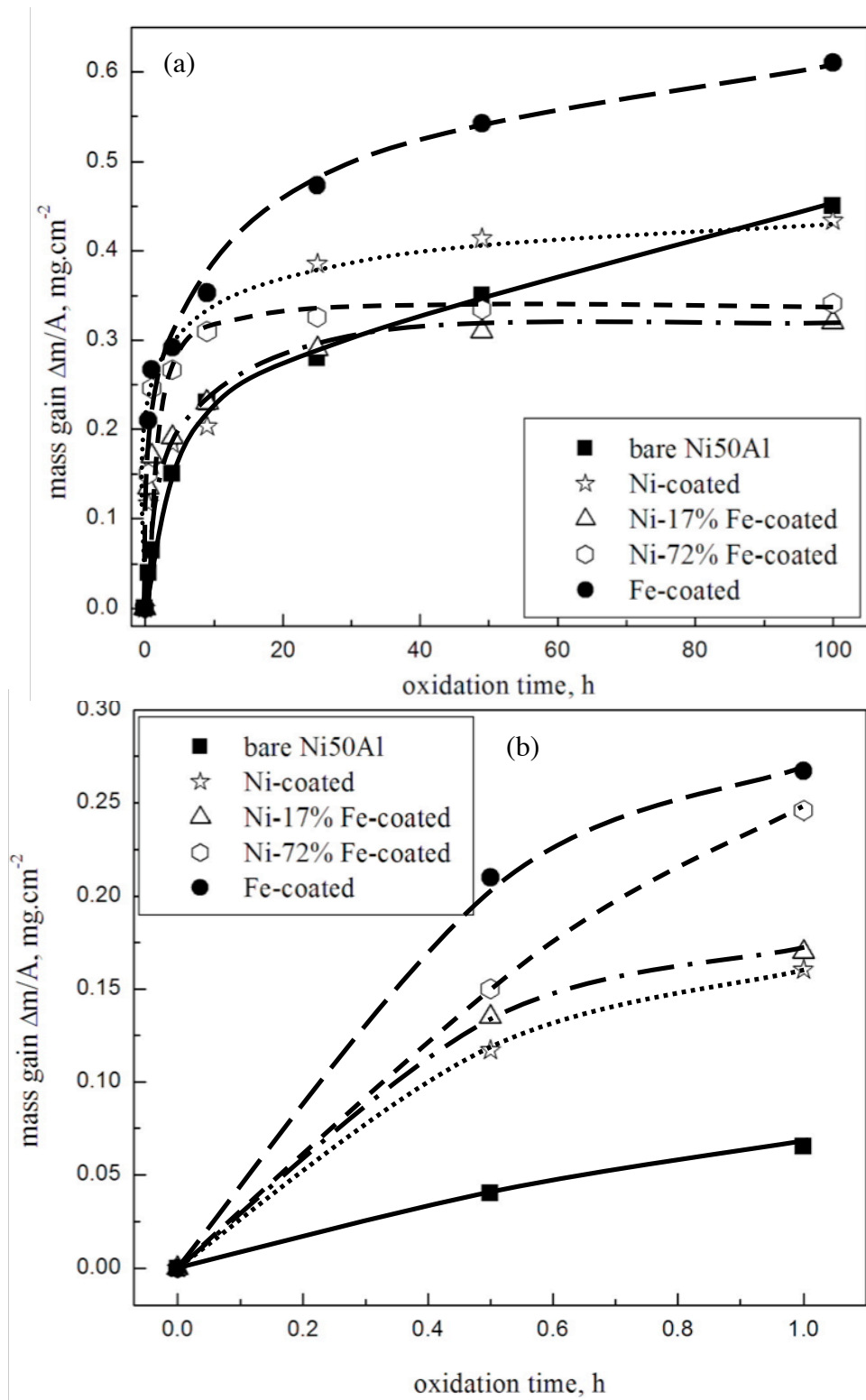
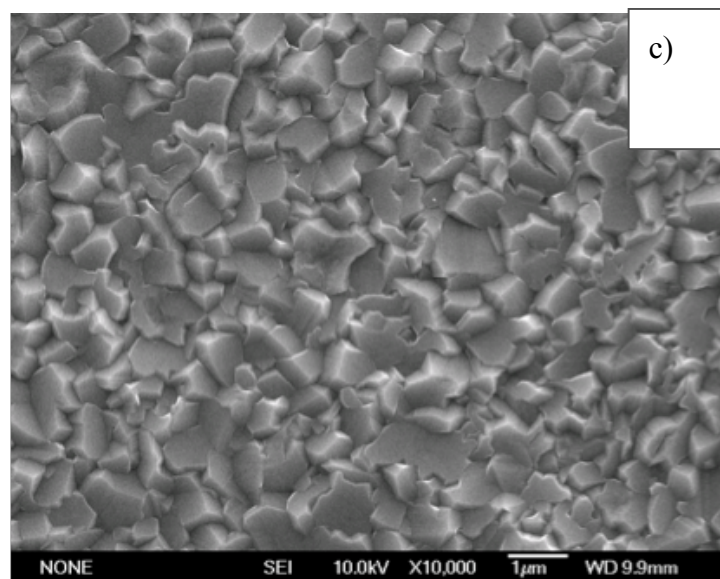
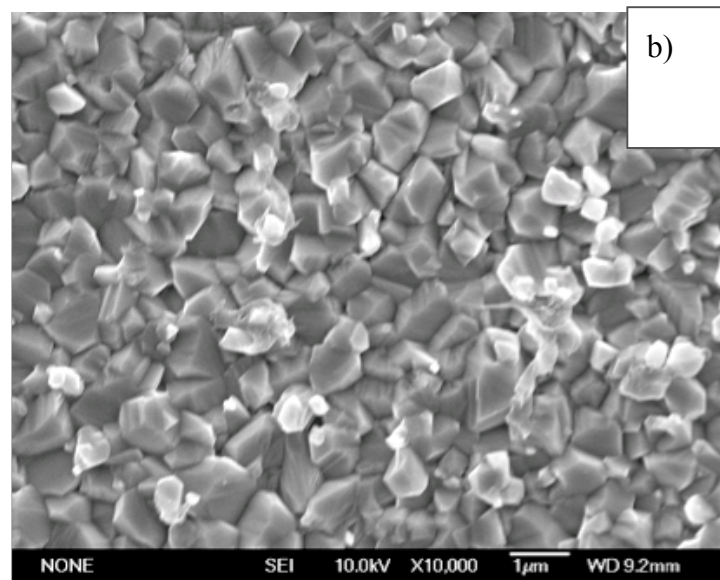
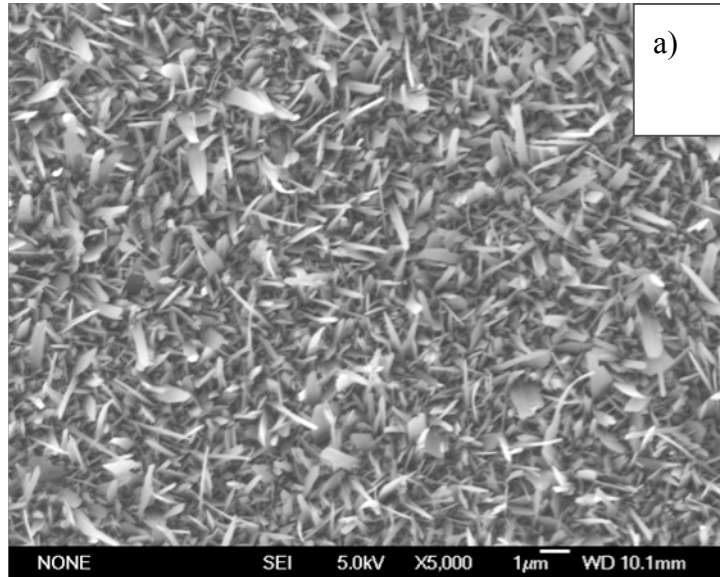


Figure 6.4: Change of oxidation mass gain of bare Ni50Al, Ni-, Ni17 wt. %Fe-, Ni72 wt. %Fe- and Fe- coated Ni50Al samples in the oxidation tests at 1000 °C in air up to 100 h (a) up to 1 h (b).



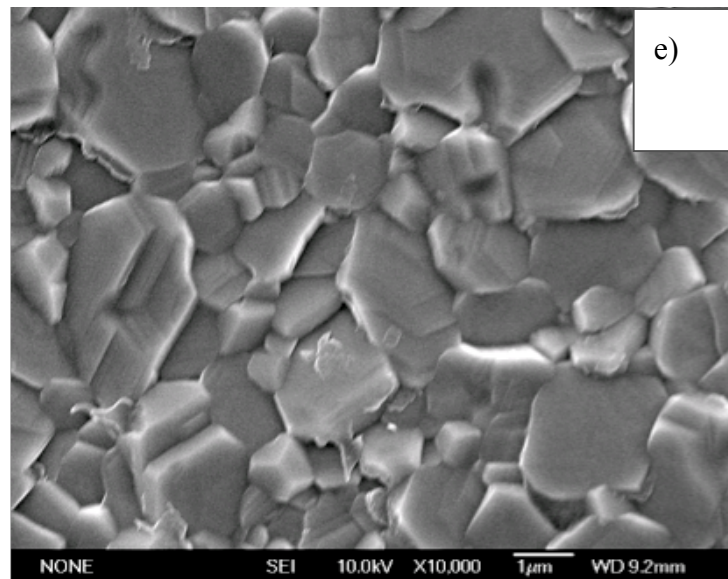
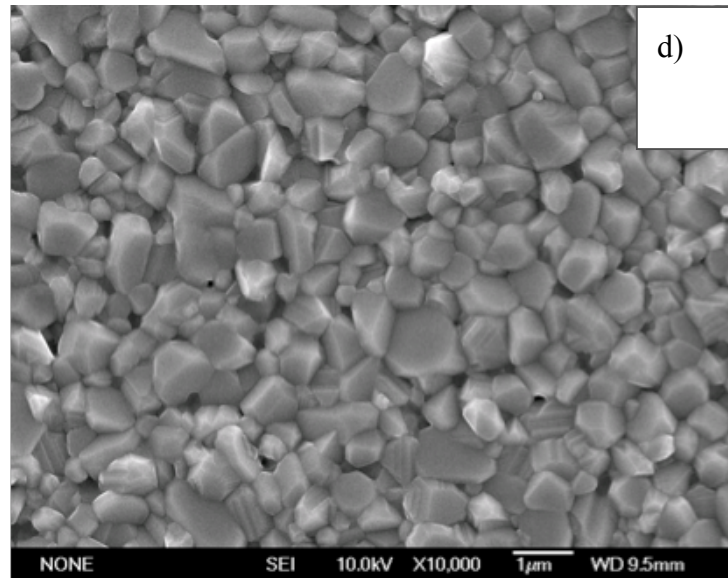


Figure 6.5: Surface morphology FE-SEM images of bare Ni50Al (a), Ni- (b), Ni17 wt. %Fe- (c), Ni72 wt. %Fe- (d) and Fe- (e) coated Ni50Al samples after oxidation for 9 h at 1000 °C in air

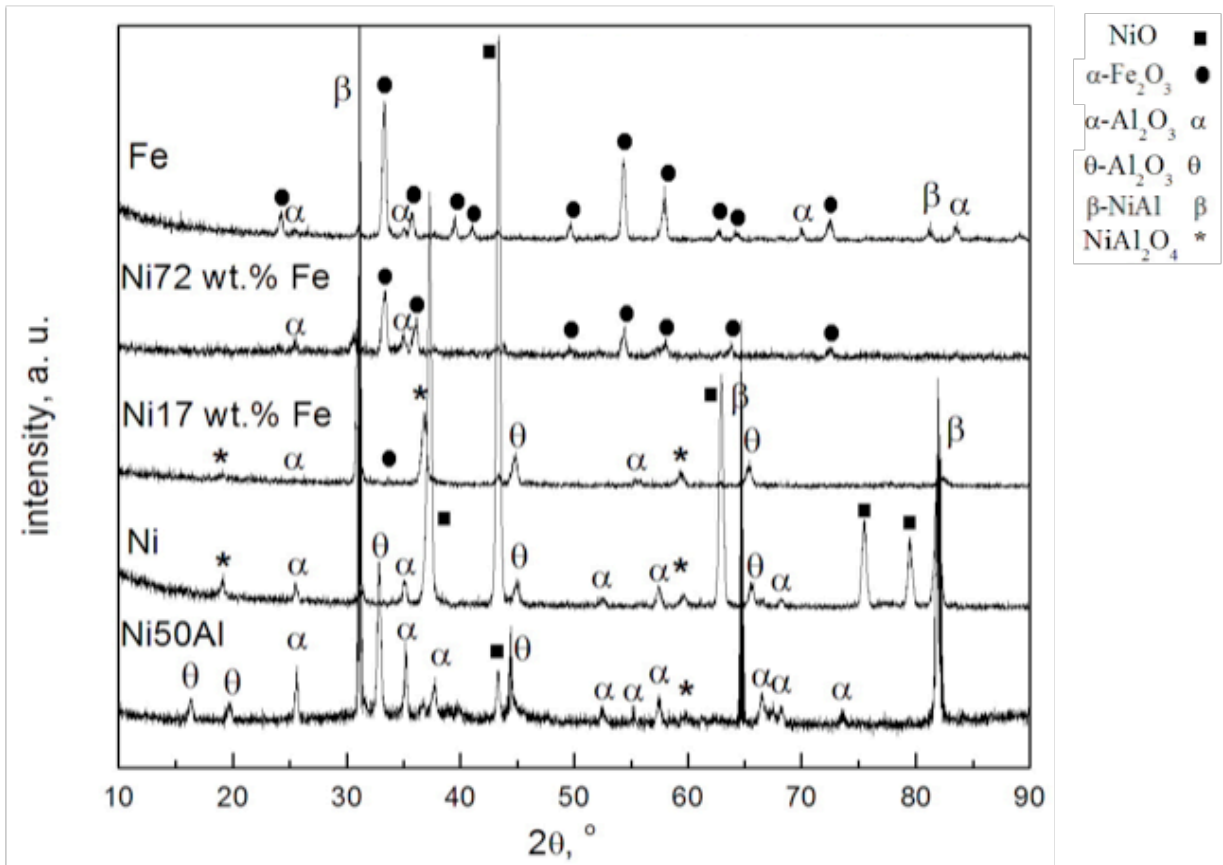


Figure 6.6: XRD patterns of bare Ni50Al, Ni-, Ni17 wt. %Fe-, Ni72 wt. %Fe- and Fe-coated Ni50Al samples after oxidation for 9 h at 1000 °C in air

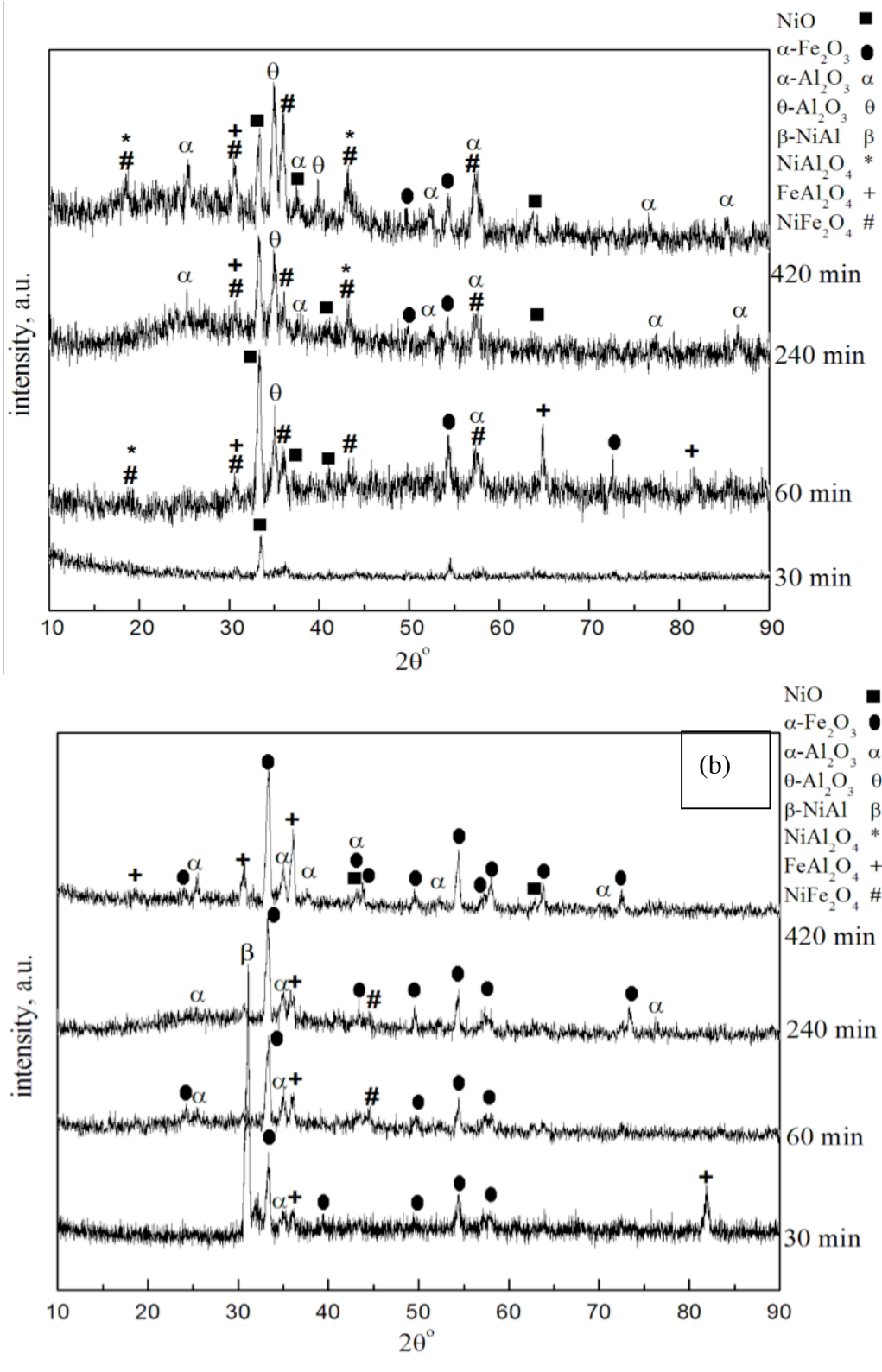


Figure 6.7: XRD patterns of (a) Ni17 wt. %Fe for 0.5-7 h (b) Ni72 wt. %Fe for 30 to 420 min. at 1000 °C in air

XRD patterns of oxidized samples and their phase's identifications are summarized in **Fig. 6.6** and **Fig. 6.7** and **Table 6.1**. Al, Ni and/or Fe are oxidized simultaneously to form Al_2O_3 , NiO and/or Fe_2O_3 phases. Peaks of meta-stable $\theta\text{-Al}_2\text{O}_3$ and $\alpha\text{-Al}_2\text{O}_3$ phases were observed for a bare Ni50Al sample. Peaks of NiO, spinel NiAl_2O_4 , $\theta\text{-Al}_2\text{O}_3$ and $\alpha\text{-Al}_2\text{O}_3$ phases were observed for Ni and Ni17Fe-coated. Peaks of $\alpha\text{-Fe}_2\text{O}_3$ and $\alpha\text{-Al}_2\text{O}_3$ phases were observed for Fe and Ni72Fe-coated samples. At $t_{ox} = 9$ h, $\theta\text{-Al}_2\text{O}_3$ phase were detected for bare, Ni-coated and Ni-17Fe-coated NiAl alloy samples but were not detected for Ni72Fe-coated and Fe-coated NiAl alloy samples. It seems that Fe_3O_4 was not detected in XRD because of either the transformation to Fe_2O_3 or it was reacted with Al_2O_3 / NiO and appeared in spinel FeAl_2O_4 form and inverse spinel NiFe_2O_4 . The oxidized Ni17Fe-coated and Ni72Fe-coated samples were examined after shorter oxidation time at 30, 60, 240 and 420 min as shown in **Fig. 6.7a** and **b**. At the shortest oxidation time at $t_{ox} = 30$ min, due to oxidation of Ni-Fe alloy precoating layers, NiO and Fe_2O_3 predominated the oxide scale composition on Ni17Fe-coated and Ni72Fe-coated samples, respectively. Fe_2O_3 that formed on Ni72Fe-coated sample after $t_{ox} = 30$ min was relatively pure and by further oxidation ($t_{ox} = 30 \rightarrow 420$ min), mixed oxide phases were detected on expenses of Fe_2O_3 . $\theta\text{-Al}_2\text{O}_3$, NiO, spinel FeAl_2O_4 and fcc inverse spinel NiFe_2O_4 on Ni17Fe-coated sample and $\alpha\text{-Fe}_2\text{O}_3$, $\alpha\text{-Al}_2\text{O}_3$, $(\text{Fe, Al})_2\text{O}_3$ and spinel FeAl_2O_4 on Ni72Fe-coated sample. Meta-stable Al_2O_3 formation was not observed for Ni72Fe-coated sample.

Table 6.1. Details of the detected XRD phases

precoating	t_{ox} (h)	NiO	α -Fe ₂ O ₃	θ -Al ₂ O ₃	α -Al ₂ O ₃	NiAl ₂ O ₄	FeAl ₂ O ₄	NiFe ₂ O ₄
-----	9			θ	α			
Ni	9	■		θ	α	*		
Ni-17Fe	0.5	■	●	θ	α	*	+	#
	1	■	●	θ	α	*	+	#
	4	■	●	θ	α	*	+	#
	7	■	●	θ	α	*	+	#
	9	■	●	θ	α	*	+	#
Ni-72Fe	0.5		●		α		+	
	1		●		α		+	#
	4		●		α		+	#
	7	■	●		α		+	
	9		●		α		+	#
Fe	9		●		α			

Fig. 6.8. shows the cross-sectional microstructures of the oxide scale formed on the oxidized bare Ni50Al, Ni-, Ni17Fe-, Ni72Fe- and Fe-coated samples at 1000 °C for 9 h. A single layer of θ -Al₂O₃ of needle-like morphology was observed and some columnar grains of α -Al₂O₃ phase were observed at θ -Al₂O₃/ alloy interface after $t_{ox} = 9$ h as shown in **Fig. 6.8.1**. **Figs. 6.8** indicated that the scales formed on all coated samples had a multilayered structure and were thicker than that of the bare Ni50Al sample due to the formation of fast growing oxides at the initial stage of oxidation. On the Ni-coated sample NiO grew thicker with time until coated Ni is completely consumed. Below NiO scale Al in the substrate selectively oxidized to form meta-stable or stable Al₂O₃. After

Al₂O₃ scale formation, solid phase reactions of NiO with Al₂O₃ phases may occur to form NiAl₂O₄ spinel on all coated samples as confirmed by XRD **Fig. 6.6**. This NiAl₂O₄ was clearly observed as an intermediate layer between the outer layer of NiO and the inner layer of Al₂O₃ on oxidized Ni-coated sample as shown in **Fig. 6.8.2**. EDX point analysis revealed that the composition in mass % of the outer / intermediate / inner layers is Ni_{53.22}Al_{0.67}O_{46.11} / Ni_{14.05}Al_{37.20}O_{48.75} / Ni_{0.2}Al_{51.63}O_{48.17}, which confirms the three layer structure of NiO / NiAl₂O₄ / Al₂O₃ phases [5-7, 31, 32]. Oxide scale of duplex layer structure was observed on oxidized Ni17Fe-coated sample as shown in **Fig. 6.8.3**. EDX point analysis revealed that the composition in mass % of the outer / inner layers is proposed to be Ni_{1.3}Fe_{10.1}Al_{37.7}O_{50.9} or Ni₇Fe_{1.4}Al_{35.8}O_{53.1} / Ni_{0.6}Fe_{0.5}Al_{55.1}O_{43.8}. Combining the results from **Fig. 6.8.5**, XRD and EDX confirms the formation of an outer layer of mixed (Fe, Al)₂O₃ solid solution and/or α-Al₂O₃ phases, and an intermediate scattered layer of mixed spinel phases FeAl₂O₄, NiFe₂O₄ and NiAl₂O₄ on above an inner layer of mixed Al₂O₃ phases.

Oxide scale of triplex layer structure was observed on oxidized Ni72Fe-coated sample as shown in **Fig. 6.8.4**. EDX point analysis revealed that the composition in mass % of the outer / intermediate / inner layers is Fe_{41.2}Al_{6.1}O_{52.5} / Ni_{1.2}Fe_{23.9}Al_{19.1}O₅₅ / Ni_{0.13}Fe_{0.14}Al_{52.9}O₄₆, which confirms the three layer structure of α-Fe₂O₃ / (Fe, Al)₂O₃ / α-Al₂O₃. It is believed that due to formation of (Fe, Al)₂O₃ solid solution, α-Al₂O₃ could appear in two different forms with different crystalline phases, *i.e.* (Al, Fe)₂O₃ and Al₂O₃ [33], as confirmed from XRD. The formation of a duplex Fe₂O₃ scale, with outer relative pure and inner Al saturated Fe₂O₃ scale layers was found by Hayashi *et al.* [34] and it is confirmed from TEM observation and EDX point analysis. Oxide scale of duplex layer structure was observed on oxidized Fe-coated sample as shown in **Fig. 6.8.3** EDX point

analysis revealed that the composition in mass percent of the outer / inner layers is $\text{Fe}_{45.42}\text{Al}_{1.08}\text{O}_{53.5}$ / $\text{Fe}_{0.14}\text{Al}_{53.62}\text{O}_{46.11}$, which confirms the two layer structure of $\alpha\text{-Fe}_2\text{O}_3$ / $\alpha\text{-Al}_2\text{O}_3$. The solubility limitations of Fe in $\alpha\text{-Al}_2\text{O}_3$ and Al in $\alpha\text{-Fe}_2\text{O}_3$, suggests the formation of $(\text{Fe}, \text{Al})_2\text{O}_3$ phase as a layer between $\alpha\text{-Fe}_2\text{O}_3$ and $\alpha\text{-Al}_2\text{O}_3$ on oxidized Ni72Fe-coated sample while, this layer was not observed in cross section image of oxidized Fe-coated sample.

From the point of view of atomic configuration, the oxide phases could be categorized into two groups based on their oxygen framework in other words based on the different configurations of cations in the oxygen sub-lattice. Group I includes $\theta\text{-Al}_2\text{O}_3$ and NiO (Fe_3O_4) and/or NiAl_2O_4 (FeAl_2O_4) phases are related to the similar oxygen framework of face centred cubic (fcc). In the O^{2-} framework of $\theta\text{-Al}_2\text{O}_3$ phase, $\frac{1}{2}$ of the Al^{3+} ions occupy octahedral interstitial sites and another $\frac{1}{2}$ occupies tetrahedral sites. Meanwhile, the Ni^{2+} ions occupy all the octahedral interstitial sites of oxygen framework. In Fe_3O_4 (magnetite) the oxygen anion O^{2-} form a close-packed fcc sub-lattice with Fe^{2+} and Fe^{3+} cations located in interstitial sites. Two different kinds of cation sites exist in the magnetite crystal: tetrahedrally coordinated *A* sites occupied by Fe^{3+} and octahedrally coordinated *B* sites occupied by $\frac{1}{2} \text{Fe}^{2+}$ and $\frac{1}{2} \text{Fe}^{3+}$.

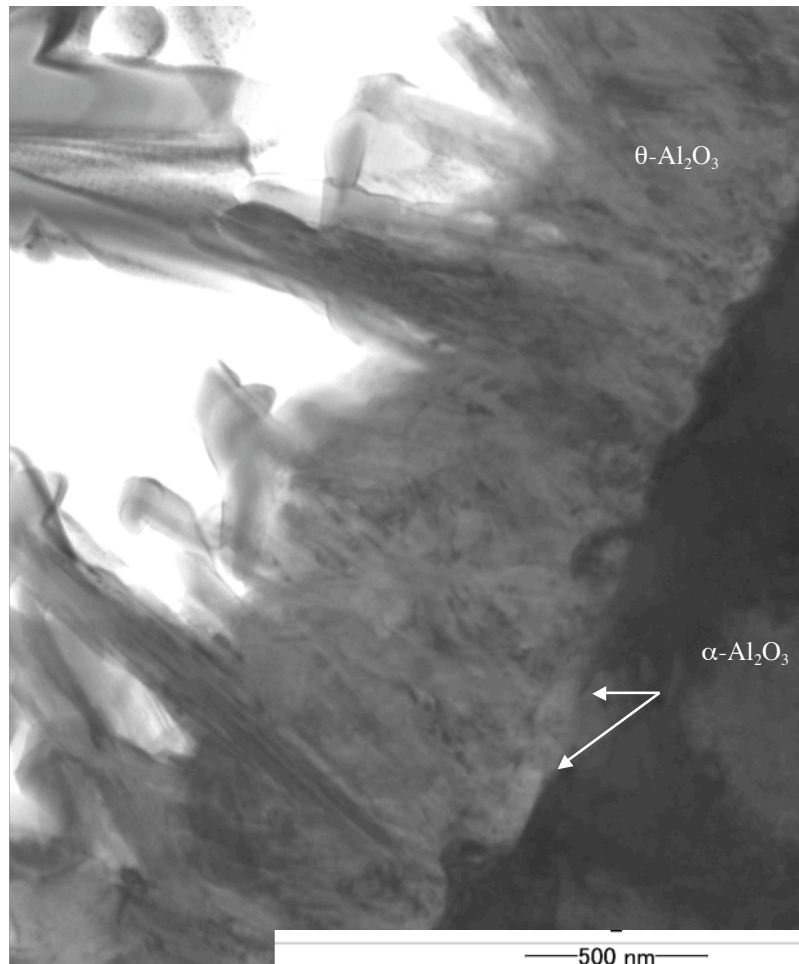


Figure 6.8.1: Cross-sectional TEM images of oxide scales formed on bare Ni50Al sample after oxidation for 9 h at 1000 °C in air

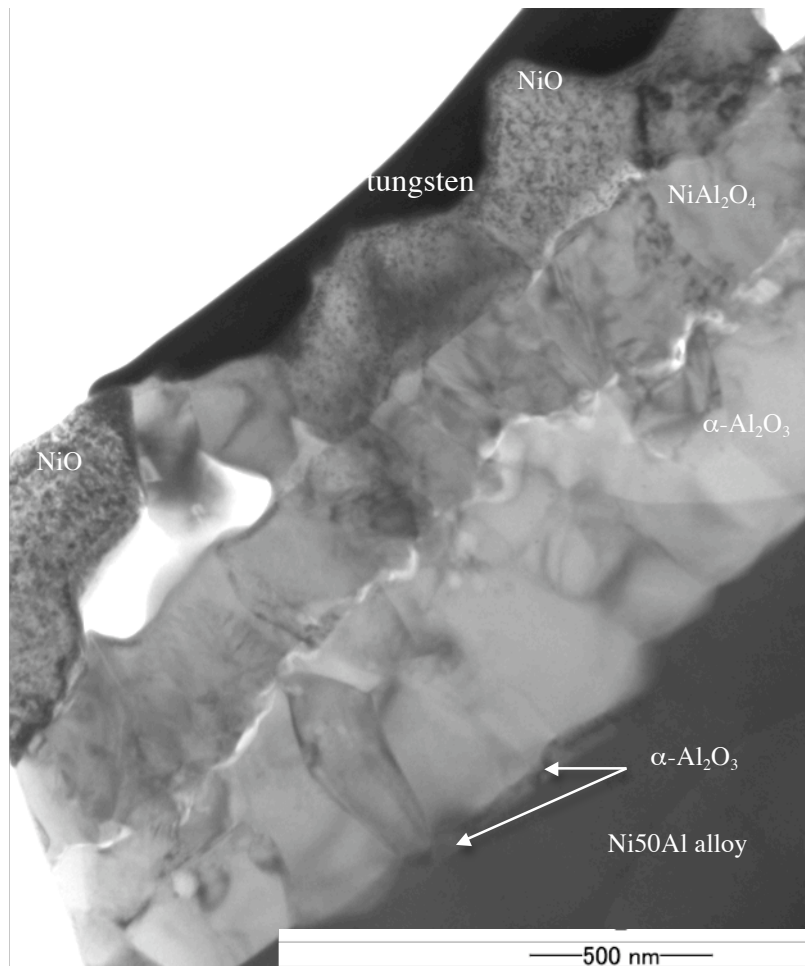


Figure 6.8.2: Cross-sectional TEM images of oxide scales formed on Ni-coated Ni50Al sample after oxidation for 9 h at 1000 °C in air

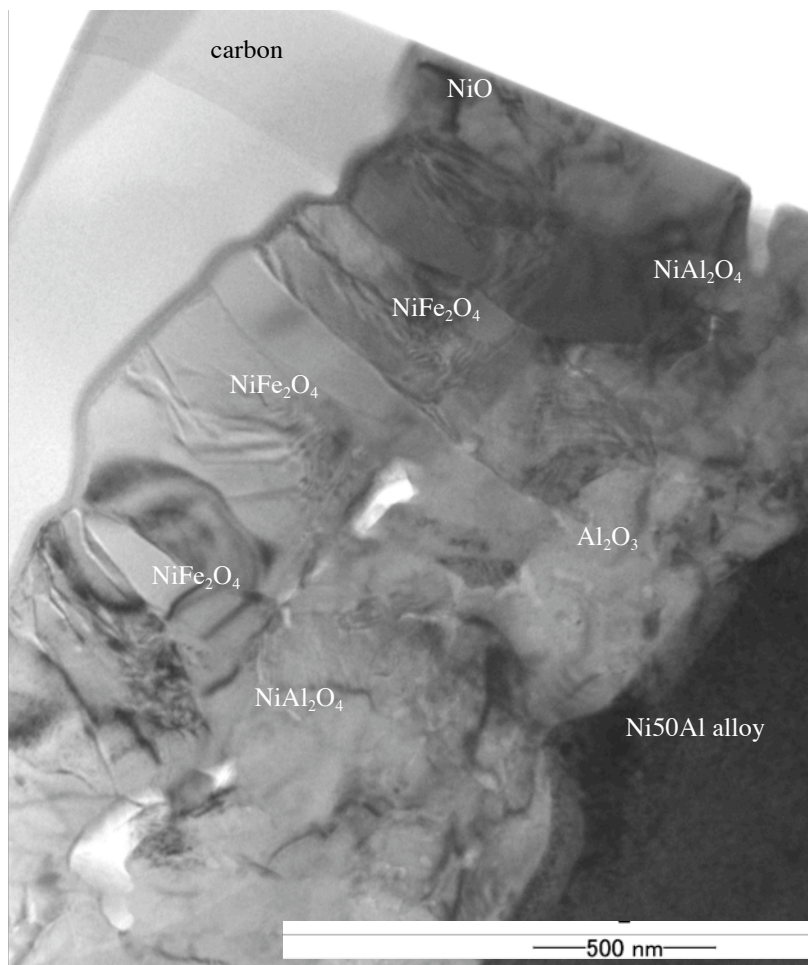


Figure 6.8.3: Cross-sectional TEM images of oxide scales formed on Ni17 wt.

%Fe-coated Ni50Al sample after oxidation for 9 h at 1000 °C in air

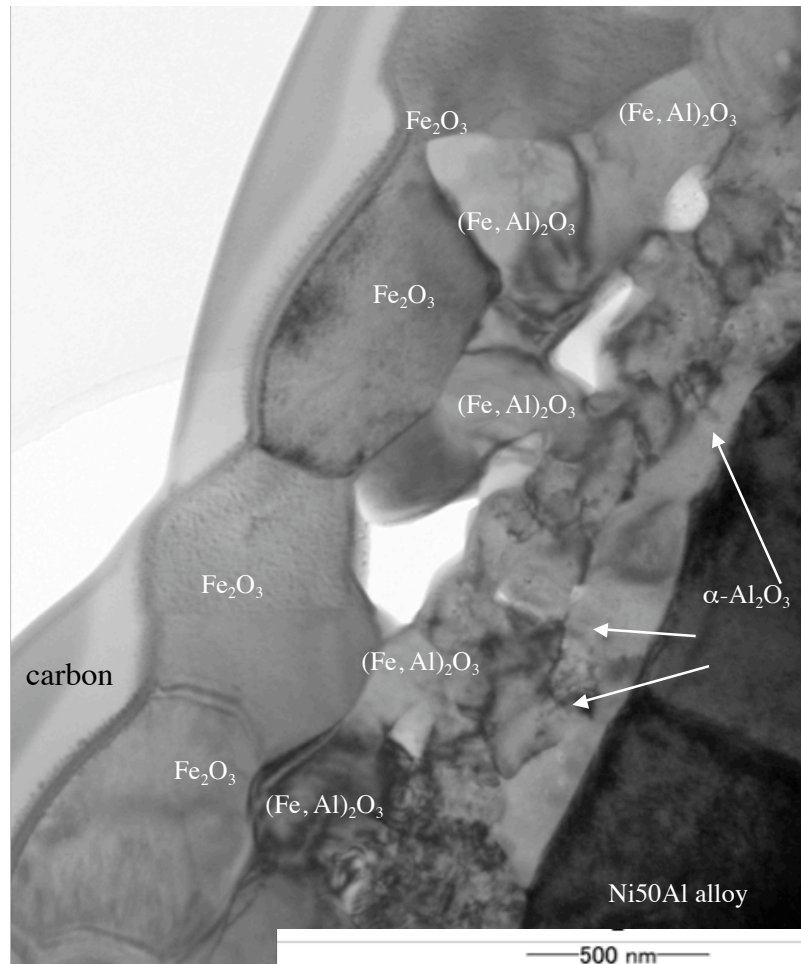


Figure 6.8.4: Cross-sectional TEM images of oxide scales formed on Ni72 wt. %Fe-coated Ni50Al sample after oxidation for 9 h at 1000 °C in air

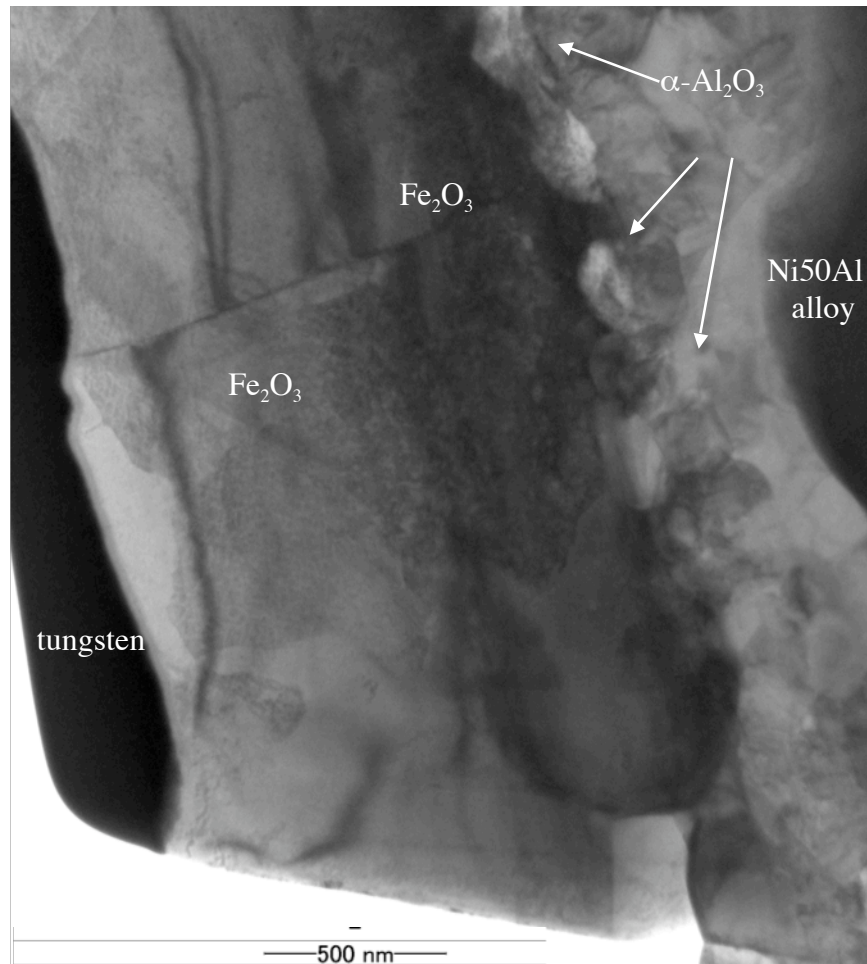
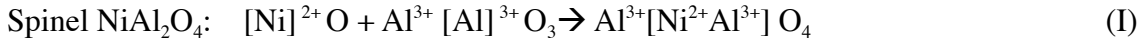
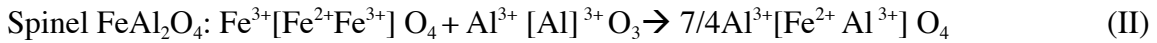


Figure 6.8.5: Cross-sectional TEM images of oxide scales formed on Fe-coated Ni50Al sample after oxidation for 9 h at 1000 °C in air

The reaction between θ -Al₂O₃ and NiO could be represented as,



And the reaction between Fe₃O₄ and θ -Al₂O₃ could be represented as,



Thus, the coexistence of NiO and/or Fe₃O₄ phases probably stabilized θ -Al₂O₃ phase for longer time by the formation of spinel NiAl₂O₄ and/or spinel FeAl₂O₄ resulted in a delay in the $\theta \rightarrow \alpha$ -Al₂O₃ phase transformation. Another reaction is expected to occur between the initially formed Fe₃O₄ and NiO phases, in which Ni may substitute Fe²⁺ in Fe₃O₄ (magnetite) to form NiFe₂O₄ (nickel ferrite) in the cubic inverse spinel structure.

The reaction between Fe₃O₄ and NiO could be represented as,



Group II includes α -Al₂O₃ and α -Fe₂O₃ phases that have a similar oxygen framework of hexagonal close packed (hcp) and both have the same corundum structure. The corundum structure can be described as oxygen sub-lattice, in which the aluminum atoms, or ions, occupy two thirds of the octahedral interstices, i.e., they have six oxygen nearest neighbors. There is thus only one coordination (octahedral) for aluminum and one for oxygen (with four surrounding aluminum ions). Thus the thermodynamic stability of α -Al₂O₃ makes it the most suited phase for use in many high-temperature applications.

From the point of view of thermodynamics and free energy, the possible reactions during the oxidation process and their Gibbs free energy of formation were listed in **Table 6.2** from ref. [35]. At the initial stage of oxidation, NiO and/or Fe₃O₄, Fe₂O₃ and Al₂O₃ grew simultaneously until Ni or Fe pre-coating was consumed. Fe₂O₃ preferentially

formed to NiO because of the higher Gibbs free energy of formation of Fe₂O₃ at 1000 °C as listed in **Table 6.2**. As a result, the oxidation mass gain on the oxidized Fe-coated had the highest oxidation mass gain among the coated samples as shown in **Fig. 6.4**. The oxidation mass gains on the coated samples were in the order of Fe-coated > Ni72Fe-coated > Ni17Fe-coated > Ni-coated Ni50Al alloy.

Table 6.2. Summary of the possible reactions during oxidation at 1000 °C in air [35]

Reaction	$\Delta G_{1000\text{ °C}}, \text{kJ}\cdot\text{mol}^{-1}$
Parent oxides	
$\text{Al(s)} + 1.5 \text{O}_2(\text{g}) \rightarrow \text{Al}_2\text{O}_3(\text{s})$	-1262
$\text{Fe(s)} + 1.5 \text{O}_2(\text{g}) \rightarrow \text{Fe}_2\text{O}_3(\text{s})$	-246.8
$3\text{Fe(s)} + 2 \text{O}_2(\text{g}) \rightarrow \text{Fe}_3\text{O}_4(\text{s})$	-236.5
$\text{Fe(s)} + \frac{1}{2} \text{O}_2(\text{g}) \rightarrow \text{FeO (s)}$	-187.6
$\text{Ni(s)} + \frac{1}{2} \text{O}_2(\text{g}) \rightarrow \text{NiO(s)}$	-130.6
$4\text{Fe}_3\text{O}_4(\text{s}) + \text{O}_2(\text{g}) \rightarrow 6\text{Fe}_2\text{O}_3(\text{s})$	-120.2
spinal phase oxides	
$\text{Fe(s)} + \frac{1}{2}\text{O}_2(\text{g}) + \text{Al}_2\text{O}_3(\text{s}) \rightarrow \text{FeAl}_2\text{O}_4(\text{s})$	-196.7
$\text{Ni(s)} + \text{O}_2(\text{g}) + \alpha\text{-Al}_2\text{O}_3(\text{s}) \rightarrow \text{NiAl}_2\text{O}_4(\text{s})$	-142.7
$\text{FeO(s)} + \text{Al}_2\text{O}_3(\text{s}) \rightarrow \text{FeAl}_2\text{O}_4(\text{s})$	-43.3
$\text{NiO(s)} + \frac{1}{6} \text{O}_2(\text{g}) + \frac{2}{3}\text{Fe}_3\text{O}_4(\text{s}) \rightarrow \text{NiFe}_2\text{O}_4(\text{s})$	-43.2
$\text{NiO(s)} + \text{Fe}_2\text{O}_3(\text{s}) \rightarrow \text{NiFe}_2\text{O}_4(\text{s})$	-28.6
$\text{NiO(s)} + \text{Al}_2\text{O}_3(\text{s}) \rightarrow \text{NiAl}_2\text{O}_4(\text{s})$	-18.7

By further oxidation, solid phase reactions between parent oxides NiO, Fe₃O₄, Fe₂O₃ and Al₂O₃ phases may occur on Ni-, Ni-17Fe and Ni72Fe-coated samples, leading to the formation of spinel phases such as; spinel NiAl₂O₄, spinel FeAl₂O₄, inverse spinel NiFe₂O₄ or the formation of (Fe, Al)₂O₃ phase as listed in **Table 6.2**. Al₂O₃ may dissolve in Fe₃O₄ as a result, beside the NiAl₂O₄ spinel formation, inverse spinel NiFe₂O₄ was formed above the inner layer of Al₂O₃ on oxidized Ni17Fe-coated sample as shown in **Fig. 6.8.3**. While, the solubility limitations of Fe in α -Al₂O₃ and Al in α -Fe₂O₃, suggests the formation of (Fe, Al)₂O₃ phase as a layer between the relatively pure α -Fe₂O₃ and the Al-saturated α -Fe₂O₃ precipitated α -Al₂O₃ on oxidized Ni72Fe-coated sample as shown in **Fig. 6.8.4**. Neither spinel FeAl₂O₄ nor solid solution (Fe, Al)₂O₃ layer was observed in cross section image of oxidized Fe-coated sample as shown in **Fig. 6.8.5**.

The growth rate of spinel (inverse spinel) intermediate layers is similar to that of meta-stable alumina and lower than that of the initially formed (parent) oxide Fe₃O₄, Fe₂O₃ NiO, resulting in reduction in the oxidation growth rate in the oxidation time from $t_{\text{ox}} = 25 \rightarrow 100$ h. Since the oxidation mass gain is an oxygen uptake during the oxidation, formation of these spinel oxides on the coated samples is found to reduce the oxidation growth rate due to the low diffusivity of oxygen in these layers during inward oxide growth. Also, the counterdiffusion of Ni²⁺ or Al³⁺ cations from the parent oxides through these spinel oxides is much slower than that through the initially formed oxides itself.

From XRD (**Fig. 6.6** and **Fig. 6.7**) and TEM cross sectional morphology (**Fig. 6.8**), θ -Al₂O₃ formation could not be observed on oxidized Ni72Fe-coated and oxidized Fe-coated samples. It seems that θ -Al₂O₃ phase was completely suppressed and α -Al₂O₃ was formed exclusively. Due to the isomorphism of α -Al₂O₃ and α -Fe₂O₃ phases, the direct formation of α -Al₂O₃ on these samples could be occurred as a result of at least one

of two reasons;

- (i) $\alpha\text{-Fe}_2\text{O}_3$ can provide heterogeneous nucleation sites for $\alpha\text{-Al}_2\text{O}_3$ phase formation preferentially than $\theta\text{-Al}_2\text{O}_3$.
- (ii) $\alpha\text{-Al}_2\text{O}_3$ was precipitated from Al saturated Fe_2O_3 , without meta-stable Al_2O_3 formation [34].

It seems that the grain size of $\alpha\text{-Al}_2\text{O}_3$ is influenced by the existence of excess Fe, which was oxidized to form $\alpha\text{-Fe}_2\text{O}_3$. Directly formed $\alpha\text{-Al}_2\text{O}_3$ layers on Ni72Fe- and Fe-coated samples were thinner and have smaller grains size than those on Ni- and Ni17Fe-coated samples, due to higher density of heterogeneous nucleation sites for $\alpha\text{-Al}_2\text{O}_3$ formation that represented in $\alpha\text{-Fe}_2\text{O}_3$ on these samples.

$\theta\text{-Al}_2\text{O}_3$ still grow on oxidized Ni-coated and Ni17Fe-coated samples until 9 h of oxidation and may be more. It seems that $\theta\text{-Al}_2\text{O}_3$ phase was stabilized by the coexistence of the intermediate spinel oxides. The formation of these spinel phases seems to have a strong effect on the grain size of $\alpha\text{-Al}_2\text{O}_3$ that reflected on the slowing of the oxide scale growth rate even though $\theta\text{-Al}_2\text{O}_3$ phase still growing.

6.4. Conclusion

The effects of Ni and Fe metallic precoating layers and Ni-Fe alloys on the oxidation products and the growth kinetics of Al_2O_3 scale formation on Ni50Al at 1000°C in air were investigated. The results are summarized as follows.

1. Ni, Ni17Fe, Ni72Fe and Fe precoating layers could be obtained by using PED technique.
2. The coexistence of the initially formed NiO and/or Fe_3O_4 phases probably stabilized $\theta\text{-Al}_2\text{O}_3$ phase for longer time by the formation of spinel NiAl_2O_4 and/or spinel

FeAl₂O₄ resulted in a delay in the $\theta \rightarrow \alpha$ -Al₂O₃ phase transformation on Ni- and Ni17Fe-coated samples.

3. α -Al₂O₃ is precipitated from Al-saturated α -Fe₂O₃ without θ -Al₂O₃ formation on Ni72Fe- and Fe-coated samples.
4. Suppression of θ -Al₂O₃ formation on these samples was reflected on the grain size of α -Al₂O₃, which was smaller than those on samples on which θ -Al₂O₃ still grow.

6.5 References:

1. H. J. Grabke, *Intermetallics* 7, 1153–1158 (1999)
2. G. C. Rybicki and J. L. Smialek, *Oxid. Met.* 275–304 (1989)
3. H.J. Grabke, M.W. Brumm, B. Wagemann, *Materials and Corrosion*, 47, 675 (1996)
4. I. Rommerskirchen, B. Eltester, H. J. Grabke, *Materials and Corrosion*, 47, 646 (1996)
5. Y. Kitajima, S. Hayashi, T. Nishimoto, T. Narita and S. Ukai, *Oxidation of Metals*, 73, 375–388 (2010)
6. A. Shaaban, S. Hayashi, K. Azumi, *Oxid. Met.*, 82, 85 (2014)
7. A. Shaaban, S. Hayashi, K. Azumi *Surf. Coat. Technol.* 266, 113–121 (2015)
8. H. Dahms, *J. Electroanal. Chem. Interracial Electrochem.*, 8, 5 (1964)
9. H. Dahms and I. M. Croll, *This Journal*, 112, 771 (1965)
10. P. C. Andricacos, C. Arana, J. Tabib, J. Dukovic, and L. T. Romankiw, *ibid.*, 136, 1336 (1989)
11. P. C. Andricacos, J. Tabib, and L. T. Romankiw, *ibid.*, 135, 1172 (1988)
12. K. Ming Yin, B. N. Popov, and R. E. White, *ibid.*, p. 103 (1992)
13. D. L. Grimmer, M. Schwartz, and K. Nobe, *J. Electrochem. Soc.* , 137, 3414 (1990)
14. P. Ganesan, S.P. Kumaraguru, B.N. Popov, *Surf. Coat. Technol.* 201, 3658 (2006)
15. W.H. Lee, S.C. Tang, K.C. Chung, *Surf. Coat. Technol.* 120–121, 607 (1999)
16. B. Tury, G.Z. Radnoczi, G. Radnoczi, M.L. Varsanyi, *Surf. Coat. Technol.* 331, 202 (2007)

17. Z.J. Huang, D.S. Xiong, *Surf. Coat. Technol.* 202, 3208 (2008)
18. S.K. Ghosh, A.K. Grover, G.K. Dey, M.K. Totlani, *Surf. Coat. Technol.* 126, 48 (2000)
19. C.R. Tomachuk, *Surf. Coat. Technol.* 122, 6 (1999)
20. Y.H. Song, G. Wei, R.C. Xiong, *Trans. Nonferrous Met. Soc. China* 17, 363 (2007)
21. S.O. Pagotto Jr., *Surf. Coat. Technol.* 122, 10 (1999)
22. P. Gyftou, E.A. Pavlatou, N. Spyrellis, *Appl. Surf. Sci.* 254, 5910 (2008)
23. S. Hessami and C. W. Tobias: *J. Electrochem. Soc.* 136 (1989) 3611– 3616
24. N. Zech, E. J. Podlaha and D. Landolt, *J. Electrochem. Soc.* 146 (8) 2892-2900 (1999)
25. H. Nakano, M. Matsuno, S. Oue, M. Yano, S. Kobayashi and H. Fukushima, *Materials Transactions*, Vol. 45, No. 11 (2004) pp. 3130 to 3135
26. M. Ramasubramanian, S. N. Popova, B. N. Popov, and R. E. White, K.-M. Yin, *J. Electrochem. Soc.*, Vol. 143, No. 7, (1996)
27. S.R. Allahkaram, M. Honarvar Nazari, S. Mamaghani, A. Zarebidaki, *Mater. Des.* 32, 750 (2011)
28. L. Chen, L.P. Wang, Z.X. Zeng, J.Y. Zhang, *Mater. Sci. Eng., A* 434, 319 (2006)
29. J. Doychak, J.L. Smialek, T.E. Mitchell, *Metall. Trans. A* 20, 499 (1989)
30. P. van Manen, E.W.A. Young, D. Schalkoord, C.J. van der Wekken, J.H.W. de Wit, *Surf. Interface Anal.* 12, 391 (1988)
31. Y. Kitajima, S. Hayashi, T. Nishimoto, T. Narita and S. Ukai, *Oxid. Met.* 75, 41 (2011)
32. S. C. Choi, H. J. Cho, Y. J. Kim, and D. B. Lee, *Oxid. Met.* 46, 51 – 72 (1996)
33. S. Hayashi, I. Saeki, Y. Nishiyama, T. Doi, S. Kyo, M. Segawa, *Mater. Sci. Forum*, 696, 63 (2011)
34. S. Hayashi, Y. Takada, I. Saeki, A. Yamauchi, Y. Nishiyama, T. Doi, S. Kyo and M. Sato, *Materials and Corrosion*, 63, No. 10 (2012)
35. Odd-Arne Lorentsen, Behavior of nickel, iron and copper by application of inert anodes in aluminum production, PhD. Thesis, 2000

Chapter 7

OXIDATION MECHANISMS

The promotion of oxidation resistance of highly Al-content alumina-forming alloys by the stable Al_2O_3 scale arises from the slow diffusion kinetics of both anions (oxygen) and cations (Al, Ni, etc...). Two main diffusion pathways are encountered to contribute the oxide scale growth kinetics; 1) lattice diffusion. 2) grain-boundary diffusion. It is well known that the diffusion through the grain boundaries is 100 times faster than that through the diffusion through lattice defects. When the alloy is oxidized at high temperature (1000 °C or more) the scale formation kinetics is dominated by grain boundary diffusion. Hence there is a strong correlation between the oxide scale grain size and its oxidation growth rate. Although the formation of only $\alpha\text{-Al}_2\text{O}_3$ is desirable to protect the alloy surface, $\theta\text{-Al}_2\text{O}_3$ and $\alpha\text{-Al}_2\text{O}_3$ phases are formed simultaneously at such high temperature (1000 °C) on NiAl alloy as shown in **Fig. 7.1**.

As long as $\alpha\text{-Al}_2\text{O}_3$ homogeneous nucleation sites cover some area, these $\alpha\text{-Al}_2\text{O}_3$ grows laterally to cover the surface alloy (**Fig. 7.1a**) with some residual $\theta\text{-Al}_2\text{O}_3$ as shown in **Fig. 7.1b**. Therefore, the lateral growth of $\alpha\text{-Al}_2\text{O}_3$ can block cations and anions diffusion to some extent, which can reduce the growth rate by as much as two orders of magnitude at late stage of oxidation.

As a result, the grain size of the $\alpha\text{-Al}_2\text{O}_3$ has a strong effect on the weight gain even if residual $\theta\text{-Al}_2\text{O}_3$ exists above the $\alpha\text{-Al}_2\text{O}_3$. So that the eq. 12 in **chapter 4** could be stated to correlate the grain size of the $\alpha\text{-Al}_2\text{O}_3$ and the oxidation growth rate constant.

$$k_p = -2 \left(\frac{\Delta\mu_i}{RT} \right) \delta_{GB} D_{GB} \frac{1}{r_G}.$$

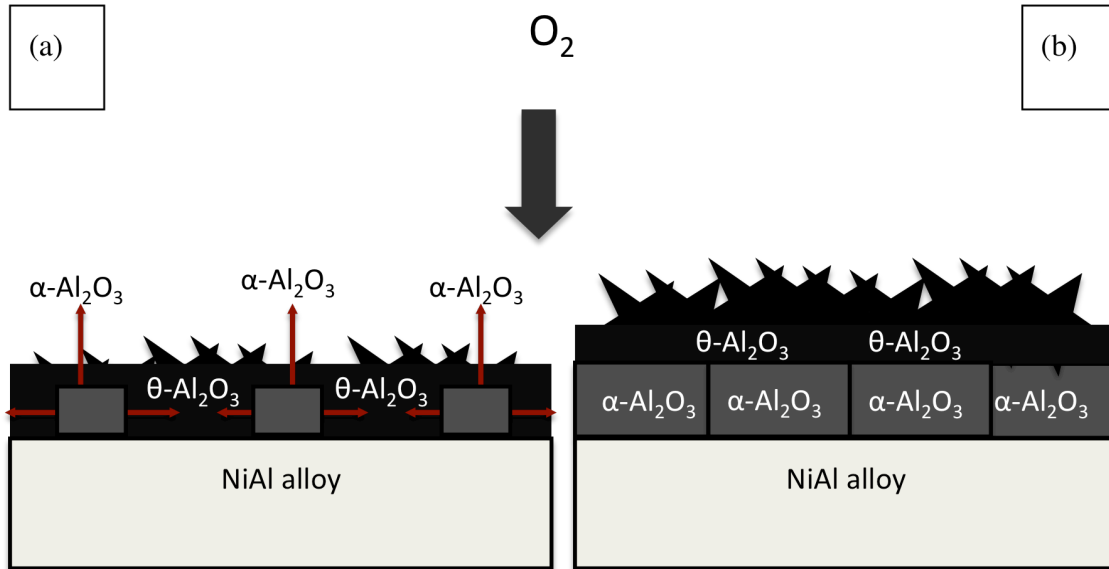


Figure 7.1: Oxidation of bare NiAl early stage (a) and late stage (b) at 1000 °C in air

Different metal precoatings affected the oxide scale morphology. The grain size of $\alpha\text{-Al}_2\text{O}_3$ on Ni-coated NiAl alloy was the largest among the coated samples. This could be owned to the delay in a complete transformation of $\theta\text{-Al}_2\text{O}_3$ to $\alpha\text{-Al}_2\text{O}_3$, which might be caused by

- The lack of the nucleation sites for $\alpha\text{-Al}_2\text{O}_3$
- Similar isomorphism of $\theta\text{-Al}_2\text{O}_3$ and NiO and/or NiAl_2O_4 phases of FCC oxygen framework and the coexistence of NiO and/or NiAl_2O_4 phases probably stabilized $\theta\text{-Al}_2\text{O}_3$ phase for longer time and delayed the $\theta \rightarrow \alpha\text{-Al}_2\text{O}_3$ phase transformation that resulted in relatively larger grain size of $\alpha\text{-Al}_2\text{O}_3$.

The oxidation mass gain on Ni-coated NiAl alloy was the lowest among the coated samples. This caused by,

- The formation of NiO and/or NiAl₂O₄ layer(s) above the θ -Al₂O₃, at the early stage of oxidation, decreased the oxygen potential gradient across the θ -Al₂O₃ scale because of the reduced oxygen potential at the NiO and/or NiAl₂O₄/ θ -Al₂O₃ interface and decreased the growth rate.
- The lack of short circuit pathways for cations and anions diffusion that contribute the oxide scale growth.

Fig. 7.2 shows a schematic illustration of the oxidation mechanism in the presence of Ni or Fe precoating. Smaller grain size of α -Al₂O₃ on alloys with Cr or Fe precoating, on which direct α -Al₂O₃ formation occurred and resulted in very fast growth rate. As mentioned previously from results of XRD analysis after pre-oxidation at 900 °C and as shown previously by Kitajima *et al.*, the Cr or Fe precoating suppresses formation of θ -Al₂O₃. The rapid formation of α -Al₂O₃ is attributed to the formation of coated metal oxides, Cr₂O₃ and Fe₂O₃, which have an isomorphous corundum structure with α -Al₂O₃. These metal oxides may provide a higher density of sites for α -Al₂O₃ nucleation, resulting in smaller grain size as shown in **Fig. 7.2**.

Although the introducing of Ni precoating that resulted in largest grain size of α -Al₂O₃ could slow the growth rate of the oxide scale, there is still a need for rapid $\theta \rightarrow \alpha$ -Al₂O₃ phase transformation, which was accomplished by Cr or Fe precoating. In order to solve this problem, in **chapter 5** a hybrid structure of Ni precoating and Fe₂O₃ nano powder as heterogeneous nucleation sites for α -Al₂O₃ formation was prepared in a form of a composite precoating layer for developing a slow growing protective α -Al₂O₃.

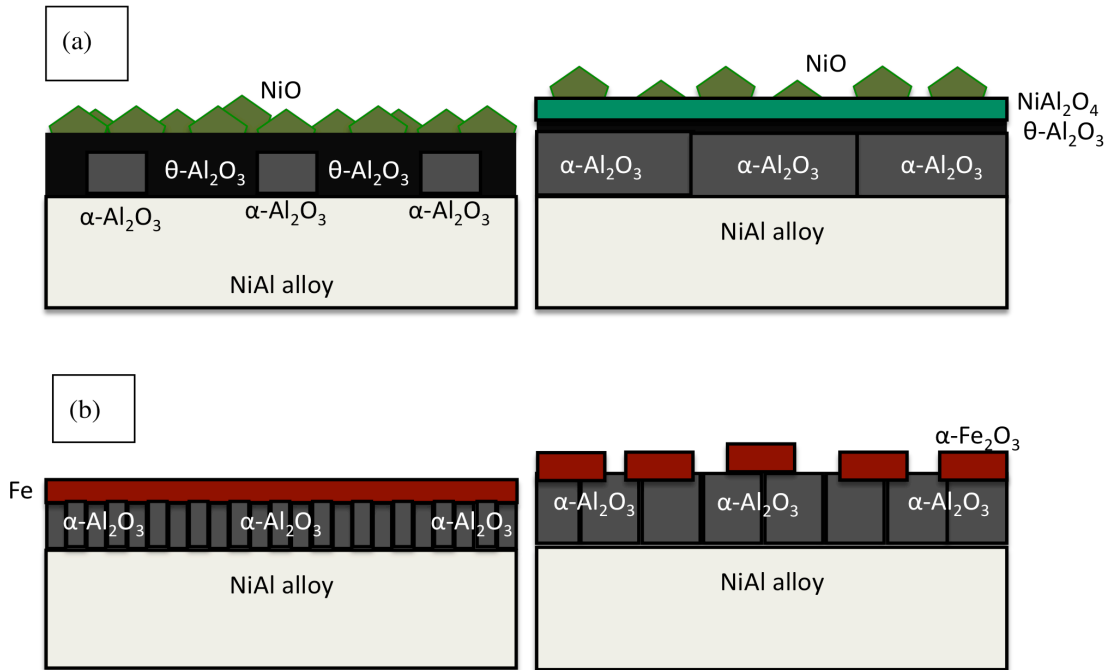


Figure 7.2: Oxidation of Ni-coated NiAl (a) Fe-coated NiAl (b) early and late stages at 1000 °C in air

It was found that the introducing of Ni precoating that resulted in largest grain size of $\alpha\text{-Al}_2\text{O}_3$ could slow the growth rate of the oxide scale and the Fe_2O_3 nano powder will act as heterogeneous nucleation sites for $\alpha\text{-Al}_2\text{O}_3$ formation. From the results obtained in chapter 5, the following reactions may be postulated to occur during the oxidation of coated samples:

(process I) formation and growth of NiO,

(process II) formation of NiAl_2O_4 spinel by a solid phase reaction of NiO and Al_2O_3 ,

(process III) a meta-stable \rightarrow stable- Al_2O_3 phase transformation, and

(process IV) the direct formation of $\alpha\text{-Al}_2\text{O}_3$ without formation of meta-stable Al_2O_3 .

Fig. 7.3 shows a schematic illustration of the oxidation mechanism in the presence of hybrid Ni-Fe₂O₃ precoating. At the initial stage of oxidation of the samples coated with Ni-coating layers in air, Ni is oxidized to form NiO. The NiO continues to grow until the surface layer of Ni is completely consumed by **process I**. Beneath the NiO scale, the Al in the substrate alloy is selectively oxidized to form stable or meta-stable Al₂O₃. After the Al₂O₃ scale formation, solid phase reactions of NiO with Al₂O₃ of any phases present may occur to form NiAl₂O₄ spinel on all the coated samples (**process II**).

Incorporation of 3.1% Fe₂O₃ nano-powder into the Ni precoating layer resulted in an accelerating effect of **process III** at $t_{\text{ox}} = 1$ h. Further addition of Fe₂O₃ nano-powder, above 5%, to a Ni precoating layer was found to promote **process IV**. According to these results, the incorporation of Fe₂O₃ nano-powder into a Ni precoating layer is a promising technique to improve the controllability of high-temperature oxidation of Al₂O₃ forming alloys.

Although the addition of Fe₂O₃ (5.2% and 7.4%) can completely suppress the formation of θ -Al₂O₃ phase or promote direct formation of α -Al₂O₃ there is a limitation of introducing more Fe₂O₃ nano powder in Ni-coating layer as a composite. To study effects of different Fe/Ni ratios on direct α -Al₂O₃ formation PED Ni-Fe co-deposits were proposed.

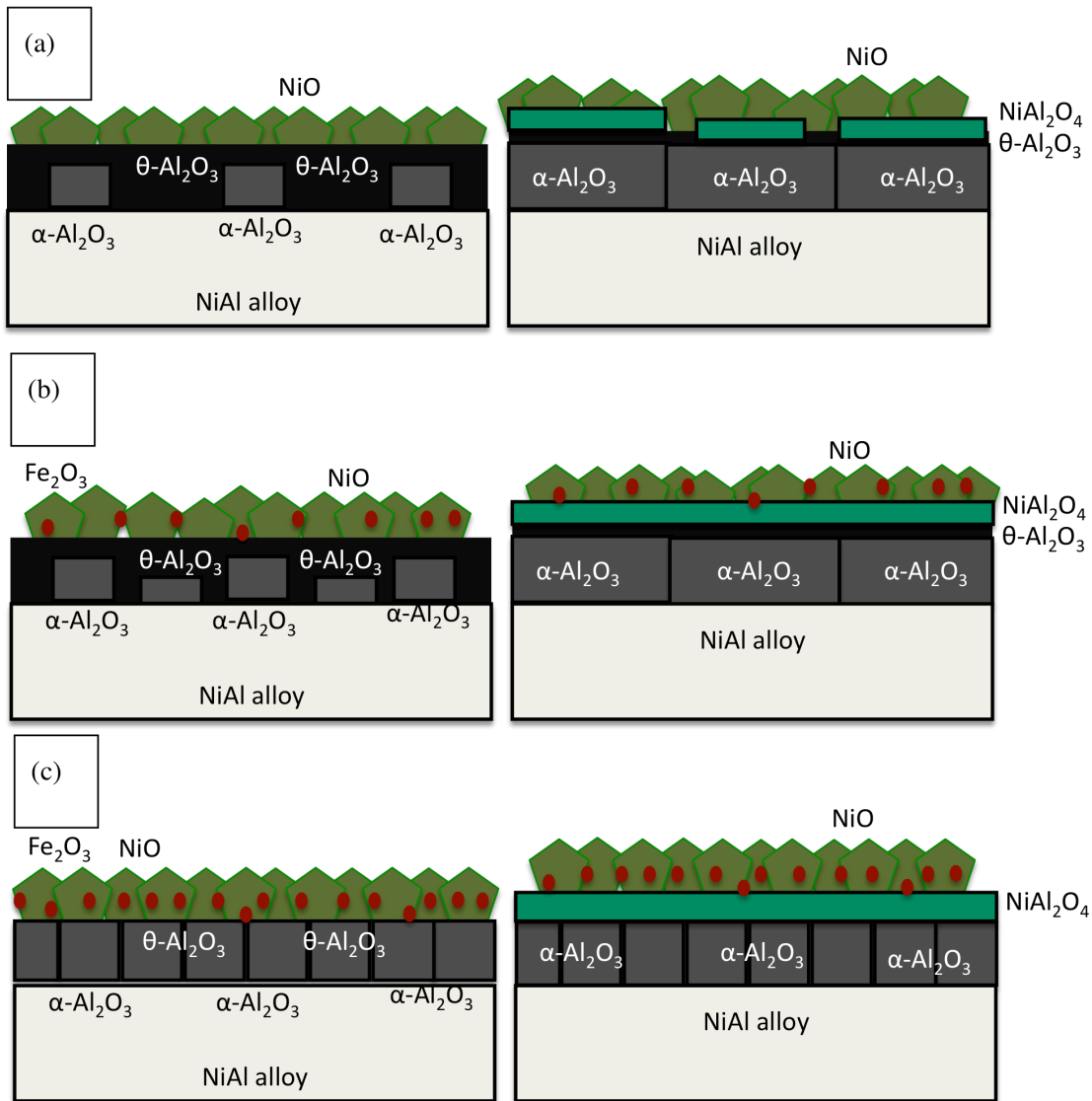


Figure 7.3: Oxidation of Ni coated NiAl (a) 3.1%Ni-Fe₂O₃ coated NiAl (b) Ni-5.2% or 7.4%Fe₂O₃ coated NiAl (c) at 1000 °C in air

It was assumed that from the point of view of atomic configuration, the oxide phases could be categorized into two groups based on their oxygen framework in other words based on the different configurations of cations in the oxygen sub-lattice as listed in **Table 7.1**. Group I includes $\theta\text{-Al}_2\text{O}_3$ and NiO (Fe_3O_4) and/or NiAl_2O_4 (FeAl_2O_4) phases are related to the similar oxygen framework of face centered cubic (fcc). Group II

includes α -Al₂O₃ and α -Fe₂O₃ phases that have a similar oxygen framework of hexagonal close packed (hcp) and both have the same corundum structure. Thus, the coexistence of NiO and/or Fe₃O₄ phases probably stabilized θ -Al₂O₃ phase for longer time by the formation of spinel NiAl₂O₄ and/or spinel FeAl₂O₄ resulted in a delay in the $\theta \rightarrow \alpha$ -Al₂O₃ phase transformation.

Table 7.1. Summary of the possible oxide properties that formed by oxidation of Ni50Al with different precoating layers

Oxide phase	Crystal structure	Oxygen framework (sub-lattice)	Unit cell parameters, Å		
			A	b	c
γ -Al ₂ O ₃	Cubic	fcc	7.924		
θ -Al ₂ O ₃	Monoclinic	fcc	11.813	2.906	5.625
NiO	Rhombohedral	fcc	2.9552		7.2275
Fe ₃ O ₄	Cubic	fcc	8.5336		
NiAl ₂ O ₄	Cubic	fcc	8.048		
NiFe ₂ O ₄	Cubic	fcc	8.3393		
FeAl ₂ O ₄	Cubic	fcc	8.1534		
α -Al ₂ O ₃	Rhombohedral	hcp	4.7592		12.992
Fe ₂ O ₃	Rhombohedral	hcp	5.0356		13.749
Cr ₂ O ₃	Rhombohedral	hcp	4.9999		13.680

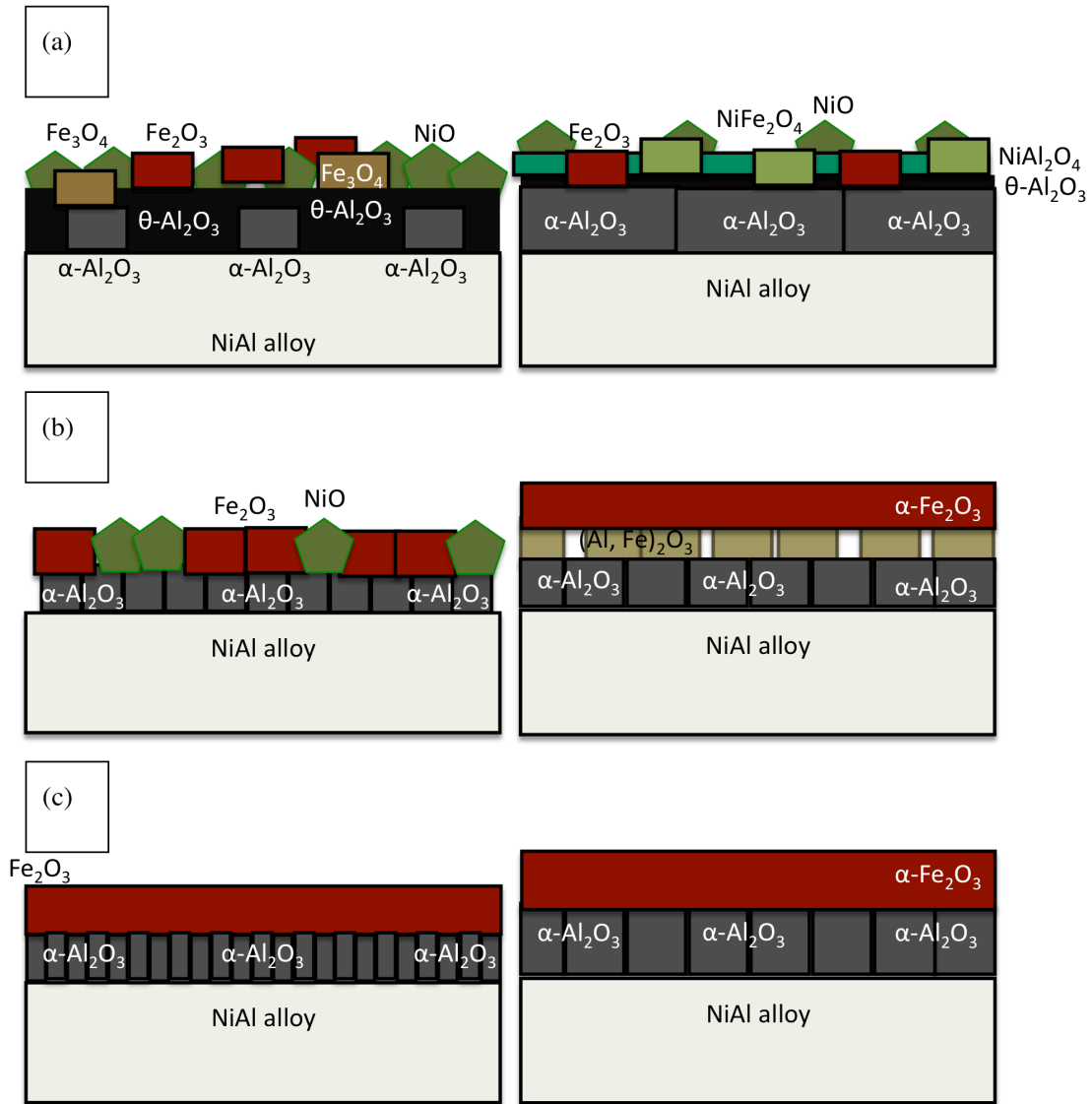


Figure 7.4: Oxidation of Ni17%Fe coated (a), Ni72%Fe coated (b) and Fe-coated (c) NiAl at 1000 °C in air

At the initial stage of oxidation, NiO and/or Fe_3O_4 , Fe_2O_3 and Al_2O_3 grew simultaneously until Ni or Fe pre-coating was consumed. As a result, Fe_2O_3 of the higher Gibbs free energy of formation preferentially formed to NiO at 1000 °C. This reflected on the oxidation mass gains on the coated samples that were in the order of Fe-coated > Ni72Fe-coated > Ni17Fe-coated > Ni-coated Ni50Al alloy.

θ - Al_2O_3 formation could not be observed on oxidized Ni72Fe-coated and oxidized Fe-coated samples by XRD or TEM. It seems that θ - Al_2O_3 phase was completely suppressed and α - Al_2O_3 was formed exclusively. Due to the isomorphism of α - Al_2O_3 and α - Fe_2O_3 phases, the direct formation of α - Al_2O_3 on these samples could be occurred as a result of at least one of two reasons;

- α - Fe_2O_3 can provide heterogeneous nucleation sites for α - Al_2O_3 phase formation preferentially than θ - Al_2O_3 .
- α - Al_2O_3 was precipitated from Al saturated Fe_2O_3 , without meta-stable Al_2O_3 formation.

The grain size of α - Al_2O_3 is influenced by the existence of excess Fe, which was oxidized to form α - Fe_2O_3 . Directly formed α - Al_2O_3 layers on Ni72Fe- and Fe-coated samples were thinner and have smaller grains size than those on Ni- and Ni17Fe-coated samples, due to higher density of heterogeneous nucleation sites for α - Al_2O_3 formation that represented in α - Fe_2O_3 on these samples.

θ - Al_2O_3 still grow on oxidized Ni-coated and Ni17Fe-coated samples until 9 h of oxidation or may be longer. It seems that θ - Al_2O_3 phase was stabilized by the coexistence of the intermediate spinel oxides. The formation of these spinel phases seems to have a strong effect on the grain size of α - Al_2O_3 that reflected on the slowing of the oxide scale growth rate even though θ - Al_2O_3 phase still growing.

Shortly, among the Fe-oxide phases α - Fe_2O_3 is strongly needed in order to form α - Al_2O_3 without meta-stable Al_2O_3 phases. Other Fe-oxide phases were found to stabilize meta-stable Al_2O_3 phases for longer oxidation time and resulted in the formation of spinel phases.

Table 7.2. Summary of alumina properties that formed at steady state of oxidation of Ni50Al with different precoating layers

Precoating System	Steady state Kp value $\times 10^{-6} (mg^2.cm^{-4}.s^{-1})$	Resultant Alumina phase(s)	Parabolic shape type
-----	1.1	$\theta-Al_2O_3 + \alpha-Al_2O_3$	I
PVD - Ni	0.2	$\theta-Al_2O_3 + \alpha-Al_2O_3$	II
PVD - Cr	1.4	$\alpha-Al_2O_3$	III
PVD - Fe	1.4	$\alpha-Al_2O_3$	III
PED – Ni-3.1%Fe ₂ O ₃	0.7	$\alpha-Al_2O_3$	II
PED – Ni-5.8%Fe ₂ O ₃	0.5	$\alpha-Al_2O_3$	IV
PED – Ni-7.4%Fe ₂ O ₃	0.4	$\alpha-Al_2O_3$	IV
PED - Ni	0.4	$\theta-Al_2O_3 + \alpha-Al_2O_3$	II
PED – Ni17Fe	0.2	$\alpha-Al_2O_3$	II
PED – Ni72Fe	0.3	$\alpha-Al_2O_3$	IV
PED –Fe	0.3	$\alpha-Al_2O_3$	IV

Figure 7.5 and **table 7.2** summarize the different parabolic behavior shapes of Al₂O₃ scale and their oxide scale growth kinetic constant kp that formed on different coated samples. It may be categorized as; **Type I** typical as bare NiAl alloy $\theta \rightarrow \alpha-Al_2O_3$ phase transformation after certain time of oxidation (100h), **Type II** similar to Ni-coated NiAl alloy $\theta \rightarrow \alpha-Al_2O_3$ phase transformation was delayed with a slow growth rate, **Type III** similar to PVD Cr or Fe-coated NiAl alloy direct $\alpha-Al_2O_3$ phase formation with a fast

growth rate, **Type IV** similar to PED Ni- ~5%Fe₂O₃ composite, Ni72Fe alloy, Fe metal coated NiAl alloy direct α -Al₂O₃ phase formation with an initial fast growth rate of Ni or Fe oxides followed by a slow growth rate.

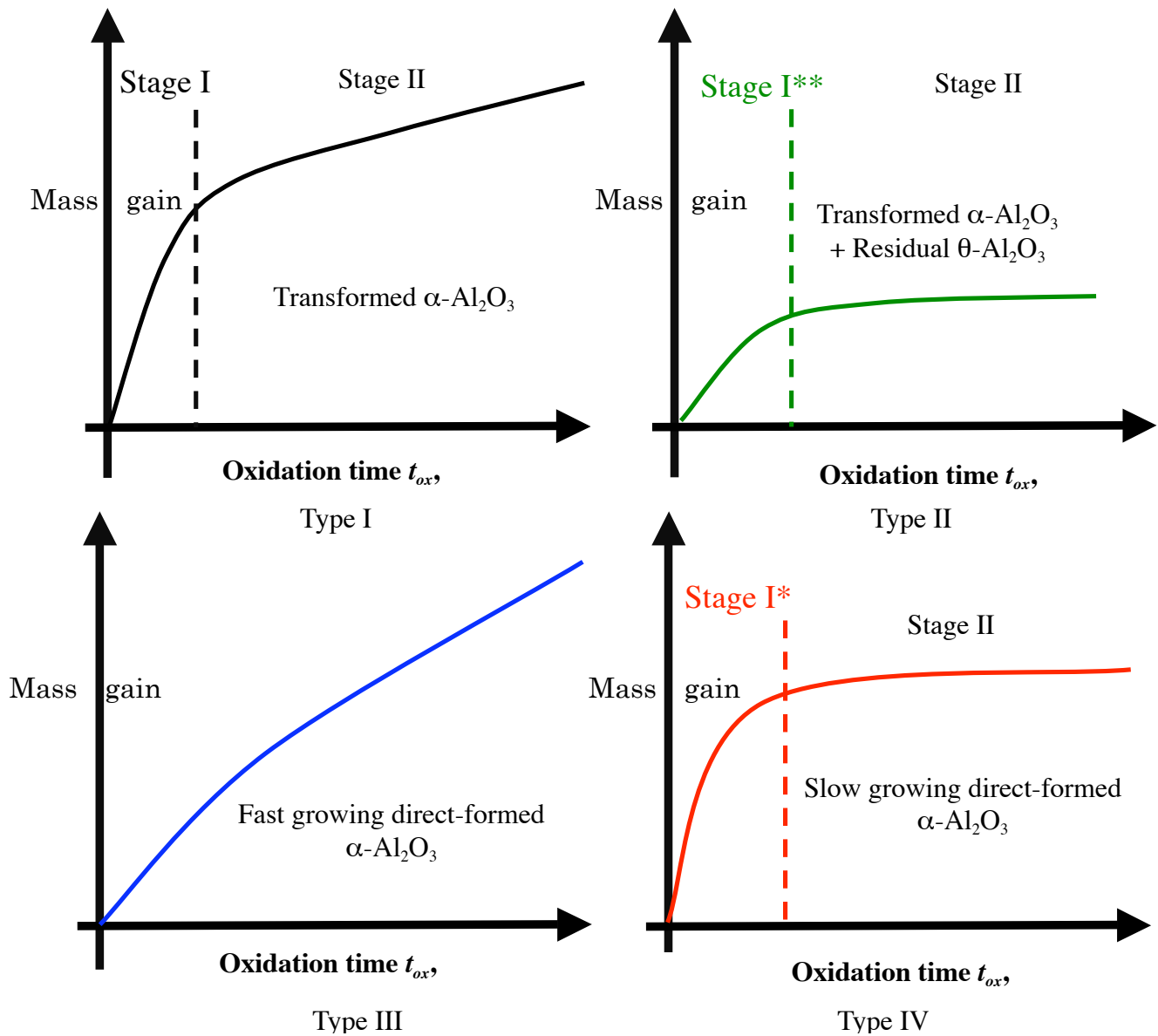


Figure 7.5: Parabolic shapes of Oxidation Kinetics of NiAl with/ without precoating at 1000 °C in air

CONCLUSIONS

The effects of different precoating systems (PVD metal precoating, PED composite precoating, PED metal NiFe alloy precoating) on the growth kinetics of α -Al₂O₃ formed on β -Ni-50Al at 1000 °C in air were investigated. The results are summarized as follows.

1. Different metal precoatings affect the long-term oxidation kinetics of alumina scale growth at 1000 °C in air because they affect the size of grains of the α -Al₂O₃ scale and the $\theta \rightarrow \alpha$ -Al₂O₃ phase transformation.
2. α -Al₂O₃ growth rate was strongly affected by the sizes of α -Al₂O₃ grains. The parabolic rate constant of the α -Al₂O₃ scale formed on coated samples with different metal precoatings increased in the order of Ni-coated < bare alloy < Fe-coated < Cr-coated samples.
3. The size of α -Al₂O₃ grains formed on samples with different precoatings increased in the order of Cr-coated < Fe-coated < bare alloy < Ni-coated samples. This order was related to the time for θ -Al₂O₃ to α -Al₂O₃ phase transformation. The α -Al₂O₃ scale that transformed earlier always consisted of smaller grains, whereas the size of grains increased with delay in θ -Al₂O₃ to α -Al₂O₃ transformation.
4. An Ni-coating layer could not suppress the formation of θ -Al₂O₃ phase, while an Ni_{3.1}Fe₂O₃-coating layer accelerated the transformation of θ -Al₂O₃ to α -Al₂O₃ phases. Further addition of Fe₂O₃ (5.2% and 7.4%) may completely suppress the formation of θ -Al₂O₃ phase or promote direct formation of α -Al₂O₃.
5. Two factors are considerably affect the structure, composition and thickness of the

oxide scales: (i) formation of NiAl_2O_4 and (ii) effect of Fe_2O_3 to accelerate the transformation of meta-stable Al_2O_3 to stable $\alpha\text{-Al}_2\text{O}_3$ or to suppress the formation of meta-stable Al_2O_3 .

6. Fe_2O_3 nano particles in Ni coating as a composite act as heterogeneous sites for $\alpha\text{-Al}_2\text{O}_3$.
7. The coexistence of the initially formed NiO and/or Fe_3O_4 phases probably stabilized $\theta\text{-Al}_2\text{O}_3$ phase for longer time by the formation of spinel NiAl_2O_4 and/or spinel FeAl_2O_4 resulted in a delay in the $\theta \rightarrow \alpha\text{-Al}_2\text{O}_3$ phase transformation on Ni- and Ni17Fe-coated samples.
8. $\alpha\text{-Al}_2\text{O}_3$ is precipitated from Al-saturated $\alpha\text{-Fe}_2\text{O}_3$ without $\theta\text{-Al}_2\text{O}_3$ formation on Ni72Fe- and Fe-coated samples i.e. Fe-coating provides precipitation sites for $\alpha\text{-Al}_2\text{O}_3$ phase formation.